VIETNAM NATIONAL UNIVERSITY

UNIVERSITY OF SCIENCE

Pham Hoang Ha

ENHANCEMENTS OF CRITICAL CURRENT DENSITY OF MgB_2 BULK AND FILM SAMPLES USING ION IRRADIATION TECHNIQUE

DISSERTATION FOR DOCTOR OF PHILOSOPHY IN PHYSICS

Hanoi - 2025

VIETNAM NATIONAL UNIVERSITY

UNIVERSITY OF SCIENCE

Pham Hoang Ha

ENHANCEMENTS OF CRITICAL CURRENT DENSITY OF MgB_2 BULK AND FILM SAMPLES USING ION IRRADIATION TECHNIQUE

Major: Thermophysics

PhD Student code: 21008024

DISSERTATION FOR DOCTOR OF PHILOSOPHY IN PHYSICS

SUPERVISORS:

1. Dr. Tran Hai Duc

   Associate Professor of Physics

2. Dr. Nguyen Khac Man

Hanoi - 2025

Declaration

I hereby declare that this is my own research work. The results written in collaboration with other authors have been approved by the co-authors prior to being included in the dissertation. The results presented in the dissertation are truthful and have not been published in any other works.

Author

Pham Hoang Ha

Acknowledgments

"Education is not preparation for life; education is life itself." - John Dewey. The beginning of our lengthy academic career is our time as PhD students. A difficult but incredibly gratifying time that required a lot of work and persistence has given me the mentality, abilities, and character I need to carry out independent study and advance science. As I reflect on the countless hours spent in libraries poring over literature, the late nights spent analyzing data, and the exhilarating moments of discovery during lab experiments, I am acutely aware that these experiences are not just stepping stones toward a degree; they are integral components of a lifelong learning process. Each challenge surmounted and each success celebrated has contributed to my growth, both as a scholar and as an individual. The lessons learned extend far beyond the classroom walls, shaping my worldview and my approach to problem-solving. My supervisors, lab partners, coworkers, friends, and family have all contributed to and supported my accomplishments to this point. I want to sincerely thank everyone who has supported me along the way, even if words can never adequately convey how grateful and loved I am.

In the first place, I want to sincerely thank my supervisors, Asso. Prof. Tran Hai Duc and Dr. Nguyen Khac Man, for their essential input, supervision, and advice during the voyage. Their enlightening remarks and helpful critiques were crucial in forming and improving my research. For all of the time and work they have put into helping me reach my academic objectives, I sincerely appreciate it.

Secondly, I would want to take this opportunity to convey my appreciation to the members of my dissertation committee for the constructive feedback they provided. The effectiveness of my job has been greatly improved as a result of their constructive criticism and advice.

Moreover, for their excitement and invaluable assistance during the project, I would like to thank my lab partners, coworkers, and friends. For their administrative and technical assistance, I would like to express my gratitude to the faculty and staff of

the Department of Low-Temperature Physics, Faculty of Physics, and other departments at the University of Science, Vietnam National University. Their help has been invaluable in helping me finish my doctoral program.

At last, I would want to take this opportunity to express my heartfelt gratitude to my family and my girlfriend for their unflinching support, tremendous inspiration, and unwavering spiritual fortitude throughout this challenging period. I have been very motivated to achieve all of my objectives as a result of their affection of me. I sincerely value the sacrifices they have made and the unwavering faith they have placed in me.

Ha Noi, December 2025

Pham Hoang Ha

Contents

List of notations and abbreviations

Notations	Explain
k_B	Boltzmann's constant
ξ	coherence length
ξ_c	c-axis coherence length
λ	penetration depth
$\lambda_{Cu\text{-}K\alpha}$	Cu-Kα radiation wavelength
J_c	critical current density
j	normalized critical current density ($j = J_c/J_c(0)$)
J_{sv}	critical current density in single vortex regime
T	temperature
T_c	critical temperature
t	normalized temperature ($t = T/T_c$)
τ	crystallite size
d	effective inter-layering spacing
I	electric current
e	electron charge
EPC	electron-phonon coupling
$FWHM$	full width at half maximum
v	hole concentration
J	interlayer coupling strength
M	magnetization
ΔM	magnetization hysteresis width
B_{irr}	irreversibility field
b	normalized field ($b = B/B_{irr}$)
b_{sb}	normalized small bundle field
B_{sb}	small bundle field
B_{lb}	large bundle field
B_{c1}	lower critical field

B_{c2}	upper critical field
F_L	Lorentz force density
F_p	pinning force density
$F_{p,max}$	maximum value of pinning force density
f_p	normalized pinning force density ($f_p = F_p/F_{p,max}$)
b_{peak}	reduced field at maximum of flux pinning force density
$\hbar$	Planck constant
Φ_0	quantum flux
R_p	mean projected ranges
R	resistance
ρ	resistivity
ρ_{300K}	resistivity at 300 K
ρ_{40K}	resistivity at 40 K
ρ_{41K}	resistivity at 41 K
κ	Ginzburg–Landau parameter
μ^*	Coulomb pseudopotential
e-ph	electron - phonon
ph-ph	phonon-phonon
DC	direct current
RRR	residual resistivity ratio
HTS	high temperature superconductor
BSCCO	bismuth strontium calcium copper oxides
HPCVD	hybrid physical-chemical vapor deposition
PCs	pining centers
CDs	columnar defects
PPMS	physical property measurement system
PDOS	phonon density of states

List of tables

List of figures

ABSTRACT

When compared to other superconductors, the conventional magnesium diboride (MgB_2) superconductor, which was found in 2001, possesses a number of benefits. These include a relatively high critical temperature (T_c) of 40 K, a high critical current density (J_c), a simple crystal structure, a low cost, and a number of additional advantages. In addition, MgB_2 is made up of two light elements: Mg and B, which are very affordable in comparison to the components that are utilized to produce iron-based and high-temperature superconductors (HTS). Other properties like as weak-link free behaviour across grain boundaries, greater coherence length, and reduced electronic anisotropy are the additional benefits of MgB_2. Nevertheless, its practical uses are limited due to its quick decline of J_c in magnetic field. On this material, a great deal of study has been done on both fundamental physical characteristics and practical applications.

In this study, the main objective is to focus on enhancements of J_c of MgB_2 bulk and film samples. Due to their ability to produce a stronger magnetic field than traditional ferromagnets, bulk superconductors can be utilized in their place. However, there exist weak link behaviour of grain boundaries in high temperature superconducting materials, which leads to the requirements of complex techniques.

First of all, the fabrication of MgB_2 bulk samples showing the strongest performance of superconductivity was carried out. The *ex-situ* MgB_2 powders were further mixed with Mg and B at different amounts and sintered at different times and temperatures. Pure *ex-situ* MgB_2 + 0.5 Mg sintered at 1000 °C for 1 hour is considered to be the optimal condition within the allowable research range for fabricating MgB_2 bulk samples with the highest possible value of J_c.

Secondly, the enhancements of J_c of the MgB_2 bulk sample were investigated by adding small amounts of the proper impurities. The co-additions of B_4C and Dy_2O_3 was expected to improve the connectivity between superconducting grains, which led

to the enhancements of upper critical field *(B_{c2})* and J_c. The greatest J_c enhancement was obtained for the sample with the co-additions of 5 wt.% B_4C + 2.0 wt.% Dy_2O_3.

Lastly, the deposition of high-quality MgB_2 thin films was studied. The hybrid physical-chemical vapor deposition (HPCVD) was known as a particularly successful approach for the deposition of MgB_2 thin films. By optimizing the growth environment, this dissertation has synthesized extremely *c*-axis-oriented 412-nm-thick MgB_2 was grown on Al_2O_3 substrates. By using the irradiation of non-magnetic ions into MgB_2 films, a dose of 5×10^{13} ion/cm^2 was shown to be optimal for providing the highest J_c enhancement. Possible reasons for the obtained J_c enhancements were attributed to the improvements of pinning ability when the pinning centers (PCs) were properly introduced. Moreover, geometry of PCs in MgB_2 bulk and film samples were analyzed by using the Dew-Hughes model. The 2-dimensional PCs were found to be dominant in the MgB_2 bulk and pristine thin film, while the formation of 0-dimensional PCs in form of point-like defects was observed in the ion irradiated MgB_2 thin films.

Chapter 1: INTRODUCTION

1.1. Superconductivity

1.1.1. History and crucial milestones

Materials in the superconductivity state lose their resistance below a temperature known as the critical temperature (T_c). Scientist Heike Kamerlingh Onnes of the Netherlands made the first observation of superconductivity in Mercury (Hg) in 1911. The resistance vanished abruptly when he cooled it to 4 Kelvin, the temperature of liquid helium, and this has since opened up a whole new field of study in low-temperature physics [33]. After that, he discovered that large transport acurrents or a magnetic field can recover the resistive condition [34]. Superconductors are entirely different in terms of mechanism and order from regular electrical conductors; they are not only superior to them. Scientists have found it to be a fascinating occurrence and an interesting subject. Superconductivity was found in numerous elemental metals by the 1930s, including Ga, Sn, Pb, Nb, Ta, and others [49,103]. Significant turning points in this area could be summed up as follows:

- Meissner effect: The elimination of a magnetic field from a superconductor when it goes from a normal to a superconducting state (1933) [56].

- The London equations: Descriptions of the electrodynamics in superconductors, able to explain Meissner effect (1935) [32].

- Ginzburg-Landau theory: An explanation of the Meissner effect through the electrodynamics of superconductors (1935) [29].

- Bardeen–Cooper–Schrieffer (BCS) theory: The microscopic mechanism of superconductivity (1957) [6].

- Josephson effect: Superconducting Copper pair tunneling across interfaces (1962) [37].

- Discovery of intermetallic and alloys: such as NbTi, Nb_3Sn, NbAl (1962) [84].

• Discovery of High T_c superconductors (1986) [10].

• Discovery of superconductivity in MgB_2 (2001) [62].

• Discovery of Iron based superconductors (2006) [40].

1.1.2. Classification

Superconductors can be categorized based on a number of factors, including their material composition, our level of interest in their physical characteristics, and our understanding of them. The predominant method involves categorizing superconductors into two groups, type-I and type-II, according to how they behave in an external magnetic field.

• Type-I superconductors:

Except for the entire magnetic field, type-I superconductors exhibit the full Meissner effect as far as a critical magnetic field (B_c) at which point a quick shift to a normal state takes place. Their tendency to permit field penetration even at low fields has earned them the moniker "soft superconductors." About thirty pure metals are type I superconductors, and the BCS theory provides a good description of their superconducting mechanism [6]. Figure 1.1(a) illustrates how magnetization abruptly and reversibly declines to zero at H_c.

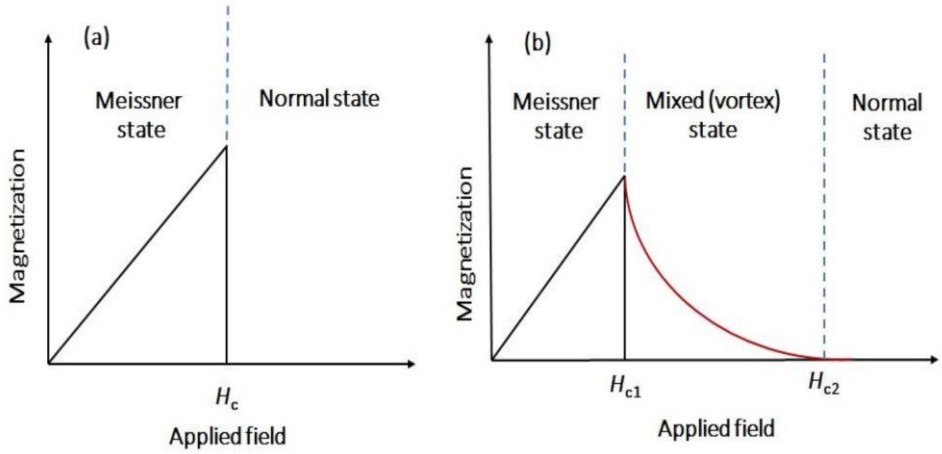

Figure 1.1. The magnetic fields dependent magnetization of (a) type-I superconductors and (b) type-II superconductors [27].

• Type-II superconductors:

Figure 1.1 illustrates how Type-II superconductors, also known as hard superconductors, react to an applied magnetic field in a distinct way.(b) Two critical fields, B_{c1} and B_{c2}, are produced by a rising field starting at zero. The superconductor displays the Meissner effect below B_{c1}. The applied field starts to partially enter the superconductor's interior at B_{c1}. Nonetheless, superconductivity persists up to the achievement of B_{c2}, a significantly higher critical field. A magnetic field of $B_{c1} < B < B_{c2}$ can enter superconductors as quantized magnetic flux, or vortex, with flux quanta of magnitude $\Phi_0 = h/2e$, where e is the electron charge and h is Plank's constant. The coherence length (ξ) determines the radius of the normal center of each vortex. Over a length determined by penetration depth (λ), electrical supercurrent flows around the vortex core and decays exponentially in magnitude [1]. The magnetic field intensity and electron number density surrounding the normal cores of a type-II superconductor are depicted in Figure 1.2. The Ginzburg-Landau parameter, or $\kappa = \lambda/\xi$, is a significant ratio that can be used to categorize superconductors. $0 < \kappa < 1/\sqrt{2}$ for type-I superconductors and $\kappa > 1/\sqrt{2}$ for type-II superconductors, respectively, represent positive and negative surface energies, respectively [29]. Since superconducting wires can be used to create high field electromagnets due to their high upper critical field (B_{c2}), type-II superconductors are the most advantageous technologically.

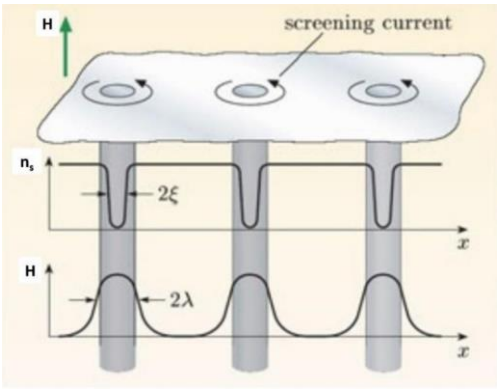

Figure 1.2. The number density of electron ns and magnetic field strength around normal cores in a type-II superconductor [22].

1.2. Vortex dynamics in superconductors

1.2.1. Flux pinning

A flux vortex is subject to a Lorentz force per unit length $f_L = \Phi_0 J \times n$ in the occurrence of a macroscopic transport current *J* (shown in Figure 1.3), where J is the current density, n is a unit vector along the flux line, and Φ_0 is the flux quantum [78]. The Lorentz force density is obtained by averaging the number of vortices, $F_L = J \times B$. An electric field normal with regard to the movement as well as the field direction is produced by this force, which tends to move flux lines perpendicular to the direction of the flow current. The primary causes of power dissipation in type-II superconductors are this vortex movement and the impact of vortex-vortex interactions. A force opposing the Lorentz force is required to "pin" the vortices in place so that dissipation by flux flow does not start as soon as they enter a type II material. Defects in the superconductor provide as energetically suitable locations for a flux line to reside, hence providing vortex pinning sites. Pinning centers can be plane defects like grain boundaries, line defects like dislocations, or point defects like vacancies and impurities [26]. The flux line lattice, f_p, experiences a pinning force that resists the Lorentz force due to the existence of those suitable spots for pinning. The pinning force density, represented by F_p, is the total pinning force that all of the elementary pinning centers in a unit volume are able to apply to the flux lines. As a

result, the greatest current density that superconducting materials can carry without dissipating power is known as the finite critical current density, or J_c. This is one of the most crucial facts for superconductor engineering applications. The Lorentz force applying on the flux lines in a unit volume is equal to the pinning force density at the critical current density J_c. Thus, the relationship is as follows [78]:

$$F_p = -J_c \times B, \tag{1.1}$$

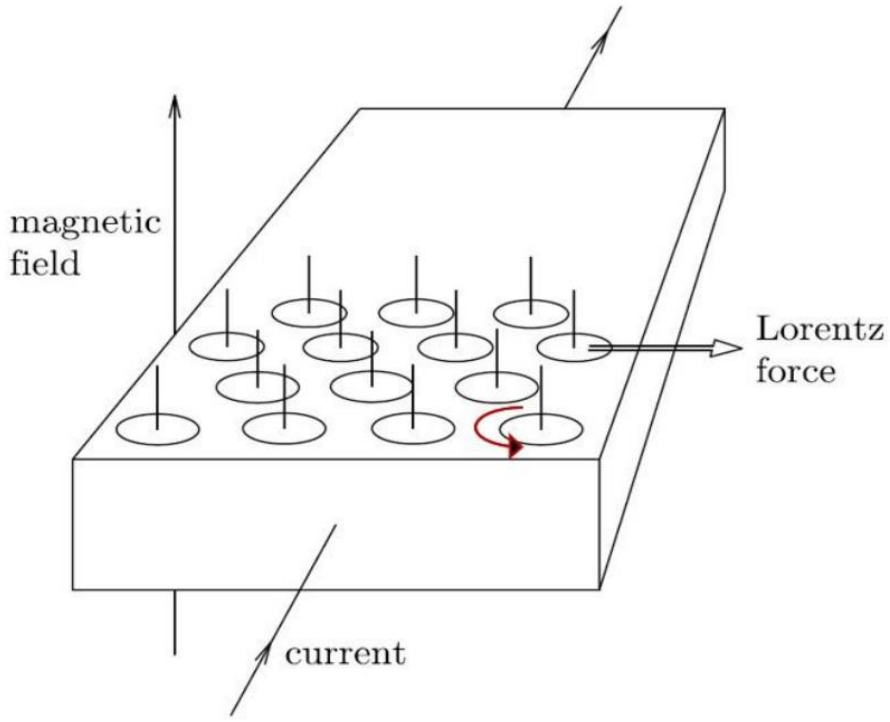

Figure 1.3. Mixed-state of type-II superconductors in presence of a transport current J [78].

Therefore, increasing the pinning sources by increasing the density of defects in superconductors is an intriguing way to improve J_c. The following will discuss several key hypotheses pertaining to flux pinning in superconductors.

1.2.2. Bean's critical state model

Bean's critical state model can be used to compute the J_c of superconductors from magnetization hysteresis (M-H) loops [9]. Assuming that each sponge filament

carried either its critical current or no current at all, Bean examined the results of his magnetization measurements. The inner filaments are protected from the field by currents that are induced in the outer filaments when the external field is increased. Once the outer filament current reaches its critical value can the field become permeable. The critical current is gradually carried by filaments until the flux reaches the sample's core. All of the filaments' current continues to flow when the field is reduced to zero, and flux becomes trapped inside the sample. The critical current in the filaments gradually reverses when a field is applied in the other direction. Bean postulated an independent critical current in the filaments. By using Ampere's law, curl H was obtained: $\boldsymbol{\nabla \times H = \mu_0 J_c}$ and $M = B/\mu_0 - H$ was the magnetization calculation [30]. From the definition, the magnetic flux density was given as $B = \frac{1}{V}\int Hdv$. Ultimately, $J_c = \frac{a\Delta M}{d}$ represents the relationship between magnetization and J_c, where d is the characteristic length, an is a numerical component that relies on the sample's form, and $\Delta M (= M_+ - M_-)$ is the height of the hysteresis loop [30].

1.2.3. Dew-Hughes model

Based on the geometry of the pinning centers and the nature of the interaction between individual flux lines and pinning centers, Dew-Hughes has constructed a model for describing flux-pinning in type-II superconductors [22]. This approach gives $F_p = \eta L f_p = -\eta L \Delta W/x$ as the pinning force per unit volume. Where ΔW, the work performed in moving a unit length of flux-line from a pinning center to the closest place whereby it is unpinned, divided by x, the effective range of the pinning interaction, equals f_p, pinning the pinning force per unit length of pinned flux-line. The efficiency factor η is derived from the degree to which a flux-line's neighbors in the flux-lattice permit it to relax towards a position of maximal pinning. L is the total length of the flux-line per unit volume which is directly pinned. There are four elements that affect these quantities:

(i) The magnitude of the local interaction is determined by the difference between the superconducting properties of the pinning centers and the matrix. This indicates the superconducting characteristics of the centers.

(ii) The local equilibrium value of μ_0H can only be determined if the size and spacing (or wavelength) of the pinning microstructure is greater than the superconducting penetration depth λ.

(iii) The entire length of the interacting flux-line and the geometrical character of the interaction are determined by comparing the diameter of the pinning centers with the flux-lattice spacing.

(iv) The stiffness of the flux lattice, since this determines whether the pinning forces are strong enough to fully disrupt the lattice and permit each flux-line to act independently, or whether displacements of flux-lines beneath local pinning pressures are merely elastic and resisted by surrounding flux lines.

Inserting the necessary values of L, ΔW, and x will allow you to identify pinning by magnetic or core, normal or $\Delta\kappa$, point, surface, or volume. Dew-Hughes has suggested the pinning functions for several scenarios following the computation. The pinning process is defined by a curve that plots the normalized volume pinning force ($F_p/F_{p,max}$) against the reduced magnetic field ($h = H/H_{c2}$). The majority of scaling laws take the following forms [22]:

$$F_p(h,T) = A{H_{c2}}^m(\mathrm{T})h^p(1-h)^q, \qquad (1.2)$$

Where the parameter m, p, and q depend on the pinning mechanism. Examples of surface pinning (grain boundary) mechanism (p=0.5, q=2) and normal point pinning mechanism (p=1, q=2) are shown in Figure 1.4.

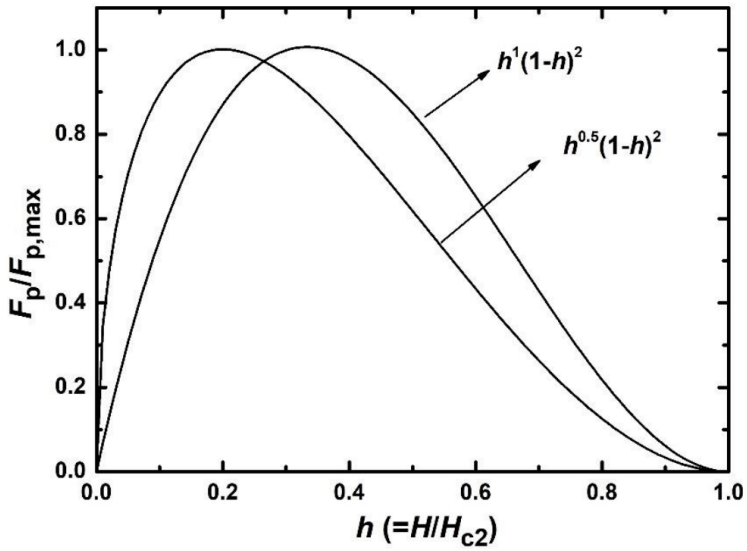

Figure 1.4. The scaling law of normal point pinning and surface pinning mechanism proposed in Dew-Hughes model [22].

1.3. Collective pinning theory

One of the most effective methods for examining the interaction between pierced vortices in type-II superconductors is collective pinning theory. According to the principles of quantum mechanics, the vortices are made up of interacting particles, and the collective interaction between these particles and their environment governs how they interact. The field dependence of J_c and the flux pinning mechanism in HTS samples would be methodically examined utilizing the collective pinning hypothesis.

In the 1980s, researchers attempting to comprehend the vortex correlations in superconducting materials while randomized defects or impurities were added initially proposed the basis of the collective pinning theory. It was evident that the type-II semiconductors' penetrating vortices tended to get stuck in the samples' tiny areas, which make up the vortex lattice. The combined interaction of the vortices and the material flaws may have been the source of the observations [1,11].

Then, based on the idea that vortices can interact with one another and the surrounding material via a number of mechanisms, including temperature fluctuations and elastic/plastic deformations, collective pinning theory is established. According to the theory, vortex interactions are governed by the underlying physics

of the superconductor, and collective systems of vortices are assumed to have formed. The existence of a pinning landscape is one of the major elements that contribute significantly to collective pinning theory. The pinning landscape model provides a comprehensive description of the distribution of impurities or defects inside superconductors and how they interact. The vortex interactions may be influenced by the kind of pinning landscape. The vortices would either travel freely or be trapped in small areas of the material. The notion of critical current density is another key element in collective pinning theory. The most current a superconductor may transport before turning into a conventional conducting material is known as the critical current density. The density of vortices and how they interact with the pinning environment define the critical current density in type-II superconductors. Researchers can attempt to increase the critical current density of superconducting materials by comprehending the collective behavior of vortices and how they interact with the pinning environment. Figure 1.5 shows the schematic of collective pinning regimes as the field increases.

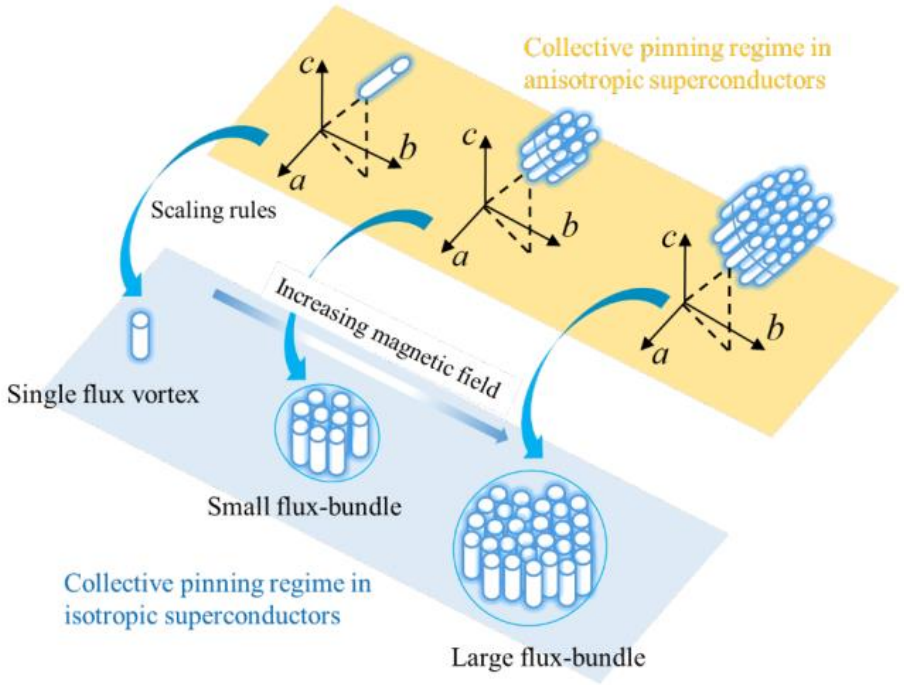

Figure 1.5. Schematic of collective pinning regimes with increasing magnetic field [53].

1.3.1. Collective pinning theory for bulk superconductors

When the magnetic field induction (B) is less than the crossover field B_{sb} of the single vortex pinning regime, J_c is field independent, in accordance with Blatter *et al. [11]*:

$$B_{sb} = \beta_{sb} \frac{J_{sv}}{J_0} B_{c2}, \tag{1.3}$$

Where β_{sb} is the coefficient with value of ≈ 5, $J_0 = 4B_c/3\sqrt{6}\mu_0\lambda$ is depairing current, $B_c = \Phi_0/2\sqrt{2}\pi\lambda\xi$ is the thermodynamic critical field, $B_{c2} = \mu_0\Phi_0/2\pi\xi^2$ is the upper critical field, and J_{sv} is the value of J_c in the single vortex regime, λ and ξ are coherence length and penetration depth and coherence length of a superconductor, respectively, μ_0 is permeability of vacuum ($\mu_0 = 4\pi\times10^{-7}$ H/m), Φ_0 is the flux quanta ($\Phi_0 \sim 2.067 \times 10^{-15}$ Wb) [9,71]. When a single vortex is pinned to a single pinning site, this is known as the single vortex pinning regime. The vortex displacement from the pinning site determines the pinning force in this regime. The small bundle pinning regime, where a few vortices are pinned together in a limited area to form bundles, happens when B > B_{sb}. The distance between the vortex bundle and the pinning location determines the pinning force in this regime. In this regime, the law of J_c is exponential [11]:

$$J_c = J_c(0).\exp\left[-\left(\frac{B}{B_0}\right)^{\frac{3}{2}}\right], \tag{1.4}$$

Where $J_c(0)$ and B_0 were fitting parameters. Numerous phenomena in type-II superconductors have been studied using collective pinning theory, such as the behavior of vortices in materials with complex pinning landscapes, the dynamics of vortices in applied magnetic fields, and the impact of thermal fluctuations on vortex motion [9,71].

1.3.2. Collective pinning theory for thin film superconductors

Larkin and Ovchinnikov introduced the idea of collective pinning for the first time in 1979 [48]. Singlevortex pinning regime refers to the low fields (close to B_{c1}) in which

a defect can firmly pin one sole vortex. The vortices can be pinned in this domain without power dissipation because the Lorentz forces are weak and the inter-vortex spacing, $a_0 \approx 1.07(\phi_0/B)^{0.5}$, is big enough to ignore the interactions between vortices. As a result, J_c is not affected by the magnetic field, and $J_c(B)$ exhibits a plateau zone. While a single defect cannot pin a vortex line, the combined impact of multiple defects can significantly alter the vortex dynamics. As the magnetic field increases, the pinning forces become weaker than Lorentz forces and interaction forces. The concept of the collective pinning is therefore introduced. The contributions of different flaws will only add up arbitrarily when the individual pinning forces functioning on the vortex line are added up; only variations in the density as well as force of the defects may pin the flux line at a specific location. When a density n_i of defects acts on the vortex line with a single force pin f_{pin}, the total force for a vortex segment of length L is equal to $F_{pin} \approx f_{pin}\sqrt{n_i \xi L}$. Collective pinning in fields can result from a high concentration of weak pinning sites. J_c is dependent on fields in the collective pinning regime according to the relation [53]:

$$J_c(H) \propto B^{-\beta}, \tag{1.5}$$

where $\beta < 1$. The pinning strength of the samples could then be assessed using the exponent β.

1.4. MgB_2 Superconductor and Subject to be discuss

1.4.1. Basic parameters

In 2001, Akimitsu"s research group announced the discovery of superconductivity in magnesium diboride (MgB_2) with T_c of 39 K [62], bring a breakthrough in the history of superconductivity. Soon after, due to advantages of this new intermetallic superconductor, it got wide attention among the scientific community. MgB_2 has hexagonal AlB_2 type crystal structure with a p6/mmm space group like other common diborides. The structure contains alternative boron and magnesium layers. The boron atoms form graphite like honeycomb network as shown in Figure 1.5. The unit cell

lattice parameter of MgB_2 are α = 3.084 Å and c = 3.521 Å. List of basic parameters for MgB_2 is shown in Table 1.1 [14].

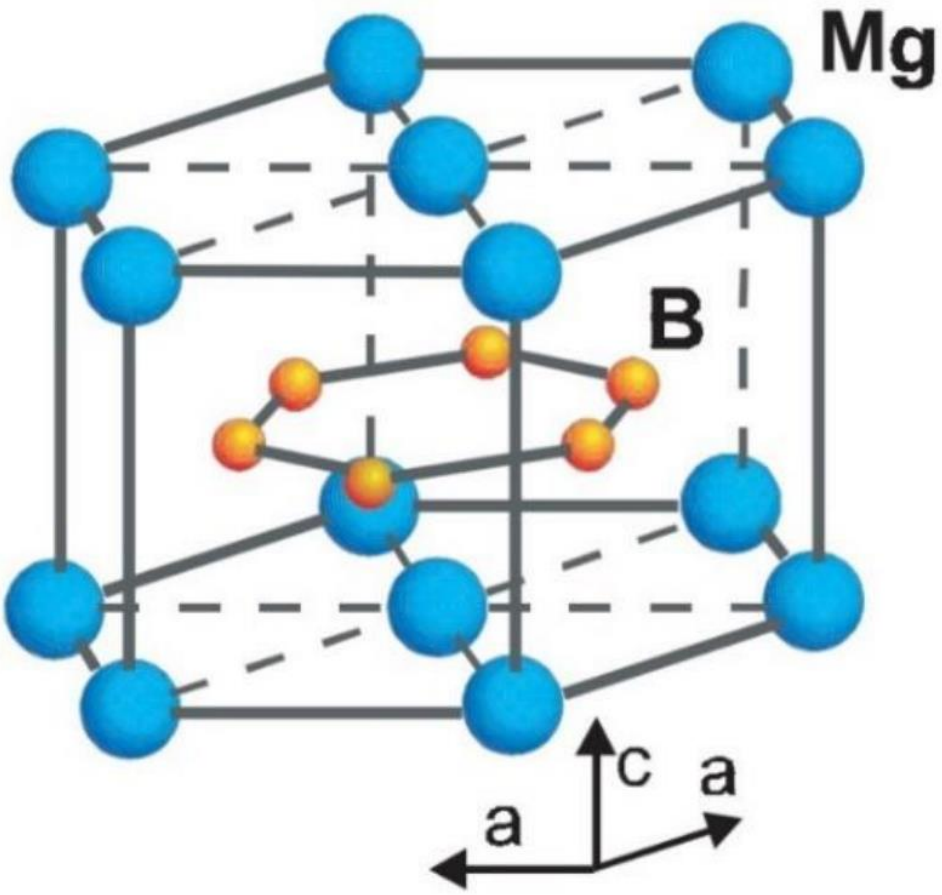

Figure 1.6. Crystal structure of MgB_2 [14]

Table 1.1. List of parameters of MgB_2 [14]

Parameter	**Values**
Critical temperature	$T_c = 39 - 40$ K
Hexagonal lattice Parameters	$a = 0.3084, c = 0.3521$ nm
Theoretical density	$\rho = 2.55\ \mathrm{gcm}^{-3}$
Pressure coefficient	$dT_c/d_P = -1.1 - 2\ \mathrm{K\ (GPa)}^{-1}$
Carrier density	$n_s = 1.7 - 2.8 \times 10^{23}\ holes\ cm^{-3}$
Isotope effect	$\alpha_T = \alpha_B + \alpha_{Mg} = 0.3 + 0.02$
Resistivity near T_c	$\rho(40\ K) = 0.4 - 16\ \mu\Omega\ cm$
Residual Resistivity ratio	$RRR\ =\ \rho(300\ K)/\rho(40\ K) = 1 - 27$
Upper critical field	$H_{c2} \parallel ab\ (0\ K) = 14 - 39\ T$
	$H_{c2} \parallel c\ (0\ K) = 2 - 24\ T$
Lower critical field	$H_{c1}\ (0\ K) = 27 - 48\ mT$
Irreversibility field	$H_{irr}\ (0\ K) = 6 - 35\ mT$
Coherence lengths	$\xi_{ab}(0\ K) = 3.7 - 12\ nm$
	$\xi_c(0\ K) = 1.6 - 3.6\ nm$
Penetration depths	$\lambda(0\ K) = 85 - 180\ nm$
Energy gap	$\Delta(0\ K) = 1.8 - 7.5\ meV$
Debye temperature	$\Theta_D = 750 - 880\ K$
Critical current density	$J_c(4.2\ K, 0\ T) > 10^7 A\ cm^{-2}$
	$J_c(4.2\ K, 4\ T) = 10^6 A\ cm^{-2}$
	$J_c(4.2\ K, 10\ T) > 10^5 A\ cm^{-2}$
	$J_c(25\ K, 0\ T) > 5 \times 10^6 A\ cm^{-2}$
	$J_c(25\ K, 2\ T) > 10^5 A\ cm^{-2}$

1.4.2. Superconducting mechanism in MgB_2

The majority of theoretical and experimental studies demonstrate that this compound fits the BCS framework, even if the transition temperature of MgB_2 is slightly greater

than that anticipated by BCS theory [6]. Based on the majority of investigations, MgB_2 can be viewed as a phonon-mediated BCS type superconductor, wherein the causes for superconductivity are the selective coupling between particular electronic states and particular phonons [14]. With two superconducting energy gaps of $\Delta\varsigma$ (~ 7meV) and $\Delta\pi$ (~ 2 meV) emanating from the px, y, and pz orbitals of the boron layer, respectively, MgB_2 possesses a layered structure. The two gaps vanish at the same T_c, as Figure 1.6 illustrates [19].

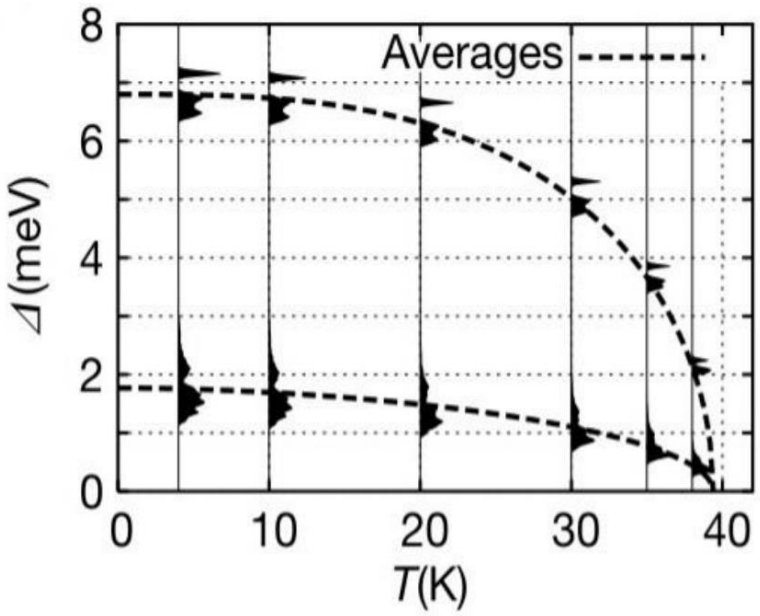

Figure 1.7. Temperature dependent superconducting gaps in MgB_2 [19]

The electronic state of MgB_2 at the Fermi level is depicted in Figure 1.7 [19]. The boron atoms in the planes are bonded together by robust two-dimensional (2D) covalent connections. There are metallic linkages that are three dimensional (3D) between the layers. Two superconducting energy gaps in MgB_2 are caused by electron coupling in the 2D bands and weak coupling in the 3D. Point contact spectroscopy and particular heat measurements provide strong evidence for the presence of two energy gaps in MgB_2 [19]. The two gaps that the theoretical computations predicted are strongly associated with these bands [3]. Based on the aforementioned data, it may be inferred that MgB_2 is a superconductor that more closely resembles normal

superconductors than high-T_c superconductors. As such, it can be incorporated into the Bardeen–Cooper–Schrieffer (BCS) framework.

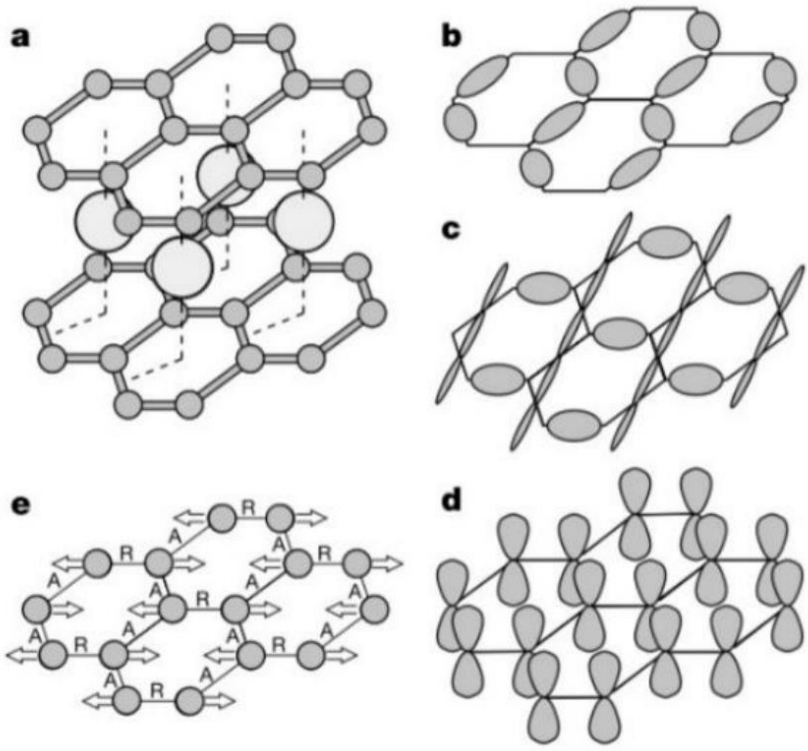

Figure 1.8. (a) Crystal structure of MgB_2, (b) (c) σ-bonding states at the Fermi level derived from boron px,y orbitals, (d) π-bonding state at the Fermi level derived from boron pz orbitals, (e) a vibrational mode of boron atoms that couples strongly to σ-bonding electronic states at the Fermi level [19].

1.4.3. Properties of MgB_2 Superconducting Materials

The industrial sector is now reaching the point of practical applications thanks to recent advancements in the creation of novel superconducting materials. High-temperature superconductors (HTS) based on bismuth strontium calcium copper oxides (BSCCO) and rare-earth barium copper oxides (MgB_2) are the most promising for broad use in a number of industries [22,44]. This category may soon include a category of iron-based superconducting compounds, namely FeSC [44], for which manufacturing procedures are being thoroughly researched. MgB_2-based superconductors are the least expensive and easiest to make for magnetic applications

out of all the materials listed. In a polycrystalline structure, MgB_2 exhibits high levels of superconducting capabilities due to the absence of the weak-link issue at grain boundaries. These qualities are essential for applications such as upper critical as well trapped magnetic fields and critical current density. The latter is HTS's main drawback. This is different from HTS, which requires texturization or epitaxial production to have good superconducting properties. Furthermore, attaining a high degree of superconducting properties is not hampered by a sufficiently large stoichiometry departure from MgB_2. Depending on the isotope makeup, the T_c of MgB_2 is approximately 39 K . Although the T_c can be lower than HTS's, it is still high enough to be used in cryogenic devices that allow for cooling using cryocoolers and liquid hydrogen, which has a boiling temperature of 20 K.

A promising green fuel with no carbon emissions is liquid hydrogen, provided it is made from renewable resources. It is the perfect fuel source for industry and transportation due to its high energy density. There is a lot of interest in the efficient storage and transportation of liquid hydrogen since it is more compact than hydrogen gas.

As a result of the aforementioned research, there has been increased interest in the development of various superconducting devices that operate at liquid hydrogen temperatures, such as transformers, motors, magnetic bearings, generators, energy storage devices, pumps, magnets, fault current limiters, transmission wires, MAGLEV transport, resonators, screens from electromagnetic irradiation, and so on. The development of superconducting MgB_2 appliances may help advance hydrogen energy technology.

Magnesium diboride compounds have slightly different characteristics than other superconductors. The structure of MgB_2 is responsible for some of these variations. The compounds have a space group of P6/mmm and a hexagonal crystal structure, hP3. $a = b = 3.084 \pm 0.001$ Å and $c = 3.522 \pm 0.002$ Å are the lattice parameters . Mg and B layers alternate in their tiered stacking . The melting point is 830 °C, and the

bulk density is 2.57 g/cm^3 and 2.63 g/cm^3 according to . The bulk modulus of the materials is around 172 GPa. Anisotropic compressibility is exhibited by the unit cell of MgB_2 crystals, where the compressibility along the c axis is greater than that along the a and b axes . MgB_2 materials in bulk exhibit isotropic properties, such as critical current density.

The study of the different characteristics of MgB_2 superconductors and their theoretical implications has been the subject of numerous articles . The characteristics of MgB_2 are thought to be closer to those of metal than HTS. This dissertation focuses solely on analyzing the effects of technological circumstances and additions on superconducting characteristics. Only a few theoretical findings are included here.

By taking into account two energy gaps, the theoretical comprehension of the properties of MgB_2 superconductors has almost been attained. The π- and σ-band gaps of the electrons of MgB_2 are often measured to be about 2 meV and 6.5 meV, respectively. These gaps can range between 1 and 4 meV and between 5.5 and 10 meV, according to.

Since the coherence lengths of MgB_2 materials are rather high (ξ_{ab} (0 K) = 3.7–12 nm and ξ_c (0 K) = 1.6–3.6 nm) , tunneling superconducting currents do not encounter obstructions from the grain boundaries. Grain boundaries may serve as effective foci for pinning. The Ginzburg–Landau parameter $\kappa(0\ K) = 26$ and the London penetration depth $\lambda(0\ K) = 125–140$ nm are estimated for MgB_2, a type II superconductor. The low-temperature penetration depth of a MgB_2 film was calculated by the authors of to be $\lambda_c = 40$ and $\lambda_{ab} = 140$ nm.

The isosurfaces of electron localization functions were recently examined in. Although the structure of a MgB_2 unit cell is straightforward and the compound is said to consist of only two elements - Mg and B - the existence of an blend of carbon, oxygen, and even hydrogen, as well as an uneven distribution of boron, can complicate the structure of materials based on MgB_2. Even in materials made under "clean" processes in protected atmospheres, an oxygen impurity is typically present

in a significant amount (in comparison to carbon). This is because magnesium has a strong affinity for oxygen. MgB_2 products may contain carbon and hydrogen admixtures that were present in the initial form of boron powder or that were absorbed from the environment.

These materials can be used in practical applications because of the following processes for preparing MgB_2 bulk materials, which enable the development of a relatively high degree of superconducting characteristics: Infiltration method (Inf.) , sintering in Ar under atmospheric pressure (PL), spark plasma sintering (SPS), shock consolidation method, high quasi-hydrostatic pressing (HP), hot isostatic pressing (HIP), field-assisted sintering technique (FAST), and hot pressing (HotP) or ultra-high-pressure-assisted sintering.

From the perspective of increasing J_c, carbon (C), carbon-containing compounds, silicon carbide (SiC), titanium (Ti), tantalum (Ta), zirconium (Zr), and compounds containing these metals are the most effective additions to MgB_2 out of the dozens of additions that have been tested. Recent research in the literature has reported on the beneficial effects of Si_3N_4 hexagonal, cubic BN (boron nitride), NbB_2, NbTi, Ni-Co-B, Rb_2CO_3, and Cs_2CO_3 additions on the superconducting properties of MgB_2-based materials. However, contradictory findings have been reported regarding the effects of the following oxygen-containing additions: Dy_2O_3, SnO_2, Sn-O, and Ti-O.

The fabrication of MgB_2 bulk superconductors and an examination of how their characteristics vary depending on technological procedures and additives are the subjects of the current overview. Temperature, pressure, holding time, contaminants, and additives are some of the production technology characteristics that are examined in relation to the structure along with superconducting properties of materials.

1.4.4. Raman spectroscopy in MgB_2 superconductors

Being a phonon-mediated superconductor, MgB_2's superconductivity is mostly dependent on electron-phonon interactions during the pairing process. For MgB_2, the E_{2g} phonon mode is a single initial-order active mode among the optical modes A_{2u},

B_{1g}, E_{1u}, and E_{2g} [91]. There are three major peaks in the frequency range of 200–1000 cm^{-1}: the shorter phonon ridge, which is mostly focused at 455–490 cm^{-1}; the intermediate phonon ridge, which is concentrated at 580–610 cm^{-1} (E_{2g}); and the bigger phonon ridge, which is primarily concentrated at 740–800 cm^{-1}. Because of the higher phonon density of MgB_2 samples, we also observe an extension of the E_{2g} ridge in the Raman spectra of MgB_2 [52]. Although most of the superconducting properties of MgB_2 are attributed to the boron plane, the E_{2g} mode notably Raman operational and closely associated with the electrical transport of bands. Therefore, Raman scattering is a suitable method for studying this phonon mode and could yield important data on crystal symmetry, particle size, and contaminants. Similarly, Raman scattering is greatly affected by residual stress and disorder [15], both of which can change phonon frequencies and lifetimes. The E_{2g} mode frequencies are expected to be approximately 515 cm^{-1} (64 meV) [45] and 665 cm^{-1} (82 meV) , while measurements have shown a broad Raman mode at about 600 cm^{-1} and 630 cm^{-1} [71]. The E_{2g} phonon's Raman shift peak fluctuated between 590 and 610 cm^{-1}.

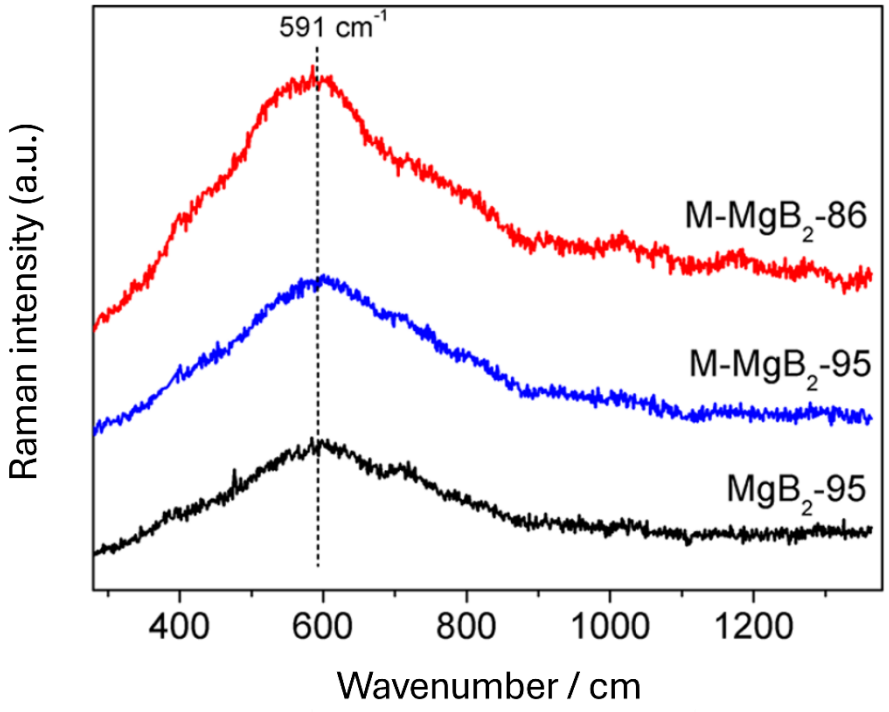

Figure 1.9. Raman spectroscopy measurements for MgB_2 [7]

Figure 1.6 shows Raman spectroscopy measurements for MgB_2 samples, where MgB_2-95 is a sample prepared from B powder with the purity grades of 95-97%-wt., M-MgB_2-95 is a sample prepared from B powder with the purity grades of 94.8%-wt. and M-MgB_2-86 is a sample prepared from B powder with the purity grades of 85.9%-wt., comprising 10-12%-wt Mg. The results showed that E_{2g} appeared at about 591 cm^{-1} for all samples.

1.4.5. Potential application of MgB_2 superconductors

Since high temperature superconductor (HTS) and MgB_2 superconductors were discovered, they have been in competition with long wires and tapes for potential and actual uses, including shields, DC magnetic field generation, and small and medium power motors [65]. For instance, bulk superconductors may trap magnetic fields that are an order of magnitude stronger than those trapped by permanent magnets (for instance, a trapped magnetic field in bulk MgB_2 can reach 5.4 T at 12 K and 5.6 T at 11 K). The production of thin films and wires/tapes also necessitates a sophisticated multi-step processing method. The procedure for fabricating bulk MgB_2 is substantially simpler. In contrast to traditional magnets, a bulk superconductor magnet can be demagnetized easily and safely by merely raising its temperature above the critical point. Numerous devices' HTS-bulk prototypes have been created and detailed in [95]. The required superconducting properties, working temperature, etc., define the kind of superconductor; nonetheless, the fundamentals of how superconducting devices work are not affected by the type. Of the practical superconductors, the lightest materials are MgB_2 superconductors, which have a bulk density of roughly 2.63 g/cm^3. Because of this, MgB_2 is appealing for portable applications [95], particularly in space and aviation technology.

Using a range of methods (high pressing, hot pressing, and spark plasma sintering), we create the MgB_2 bulk samples into discs, parallelepipeds, cylinders, and cylinders with a bottom (cap) (Figure 1.10). Rings as well hollow cylinders were electro-eroded out of these samples in oil [65] or deionized water for use in creating magnetic shields, fault current limiter models, and other devices.

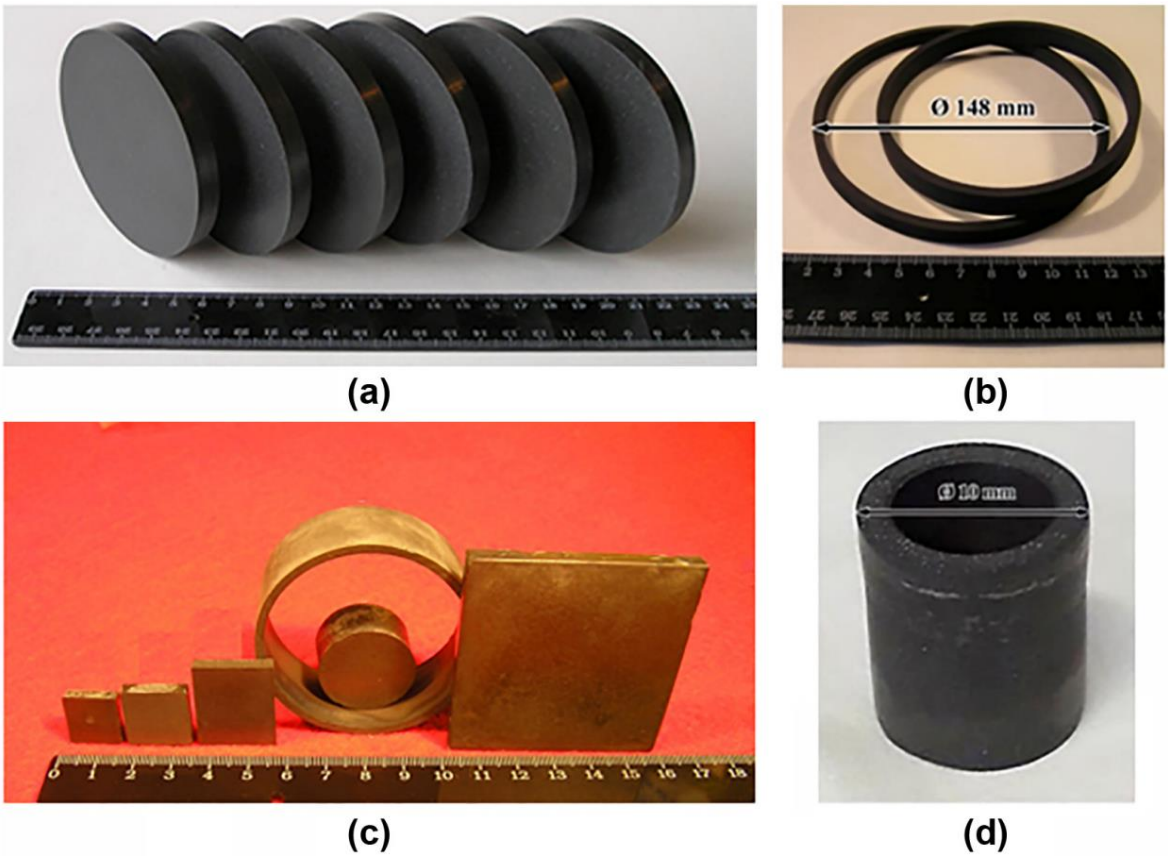

Figure 1.10. Examples of MgB_2 bulk superconductors: (a) obtained using HotP, (b) , (c) obtained using HP and then the rings were cut mechanically, and (d) obtained by machining a bulk cylinder manufactured using SPS

The standard equipment for producing bulk MgB_2 material using various techniques is depicted in Figures 1.11–1.13. The equipment used for high-pressing (Figure 1.11), hot-pressing (Figure 1.12), and spark plasma sintering (Figure 1.13) enables the production of rather large blocks that are mechanically stable, highly dense, and appropriate for practical applications (up to 100–250 mm in diameter) with high critical currents. MgB_2 may come into touch with graphite stripe or hexagonal boron nitride when magnesium diboride is synthesized or sintered using these techniques.

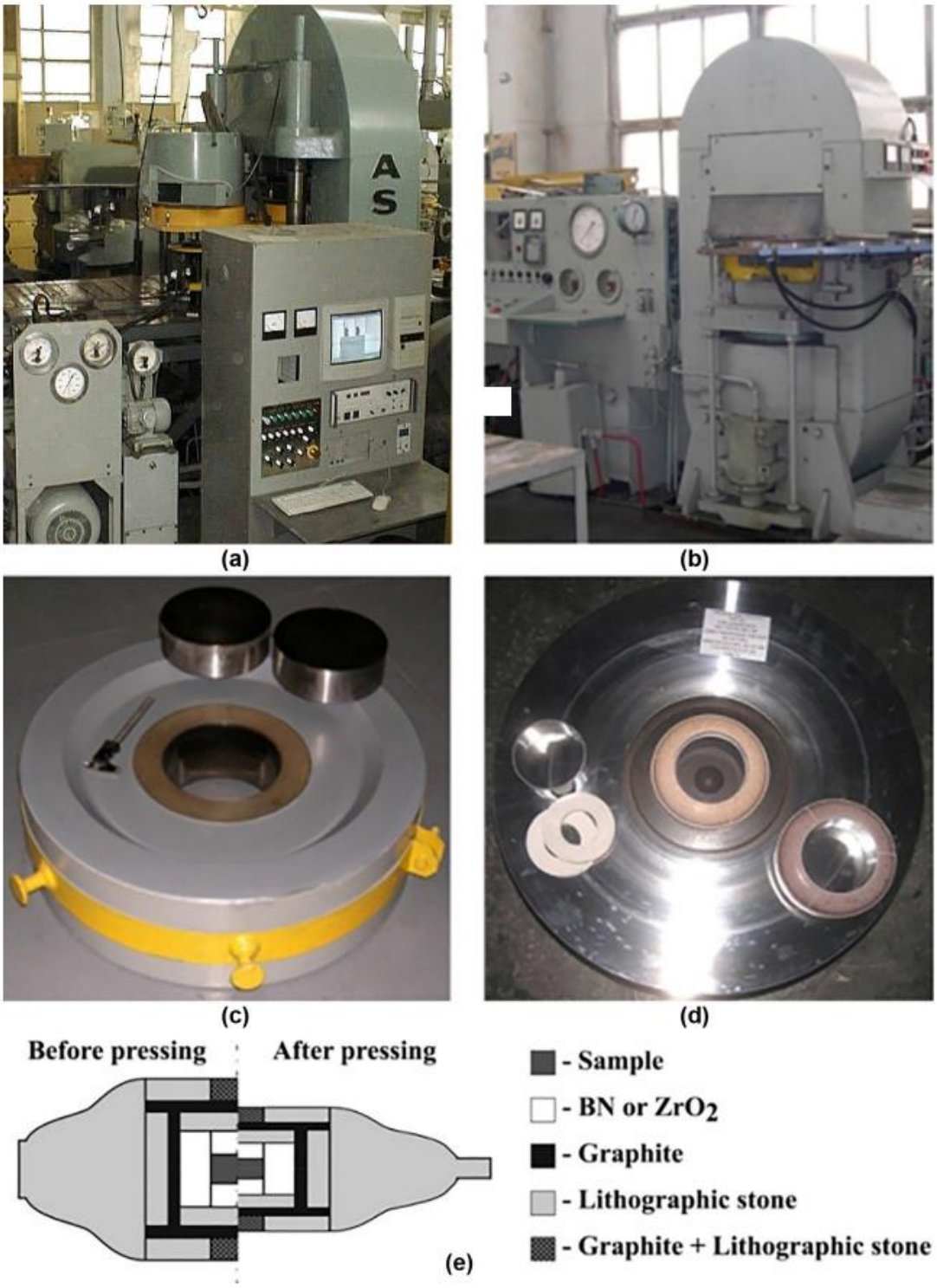

Figure 1.11. High quasi-hydrostatic pressing (HP) in ISM NASU. Hydraulic 140 MN-effort press from the ASEA company (a), hydraulic 25 MN-effort press (b), cylinder piston high–pressure apparatus (HPA) (c), recessed-anvil type (HPA) for 25 MN press (d), and scheme of high–pressure cell of the recessed-anvil HPA (before and after loading) (e) [66]

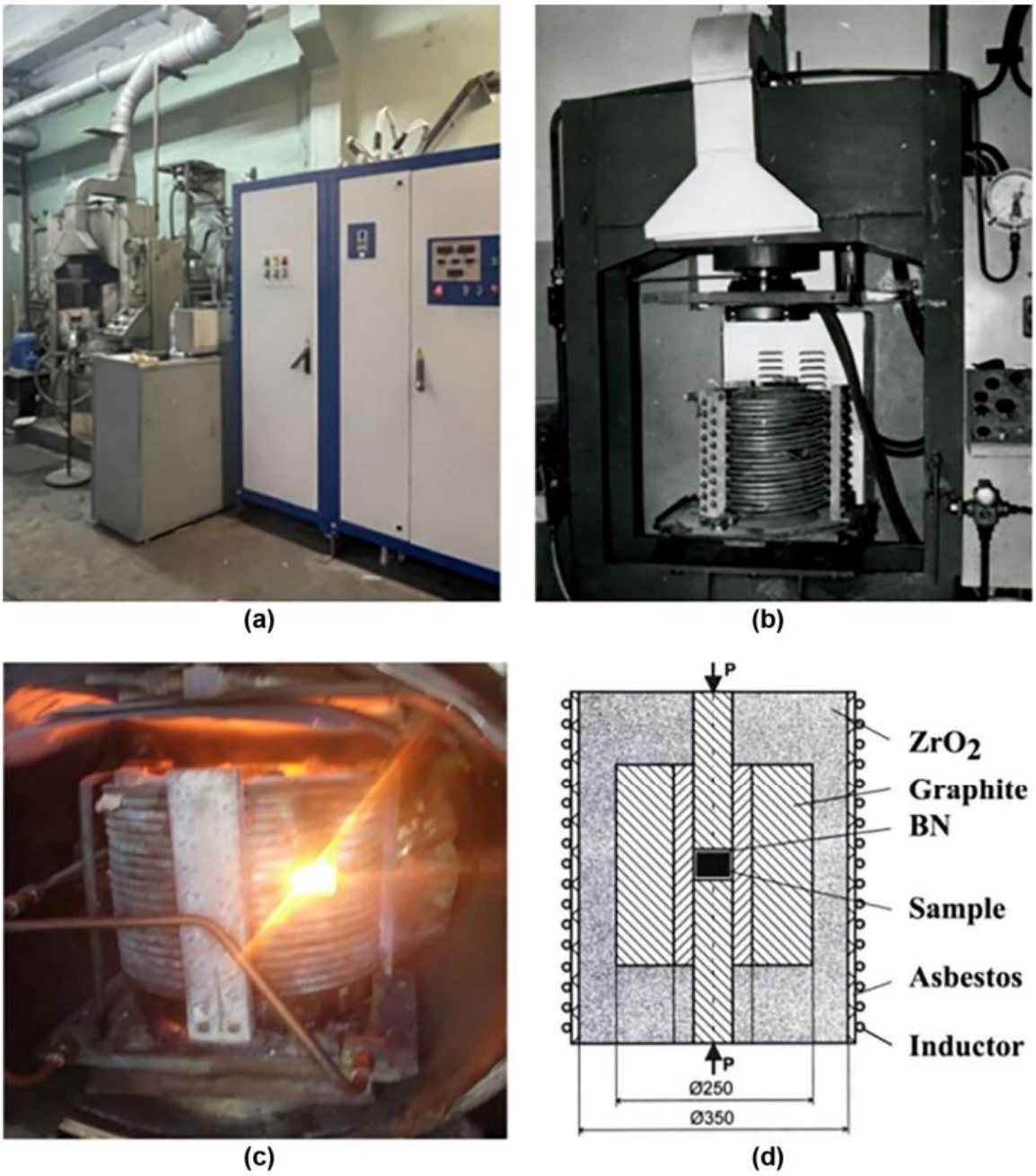

Figure 1.12. Hydraulic press DO 630 for hot pressing with generator and inductor (a,b); general view of inductor of hot press during heating (shining window—opening for temperature estimation by pyrometer) (c), scheme of assembled inductor (d) [66]

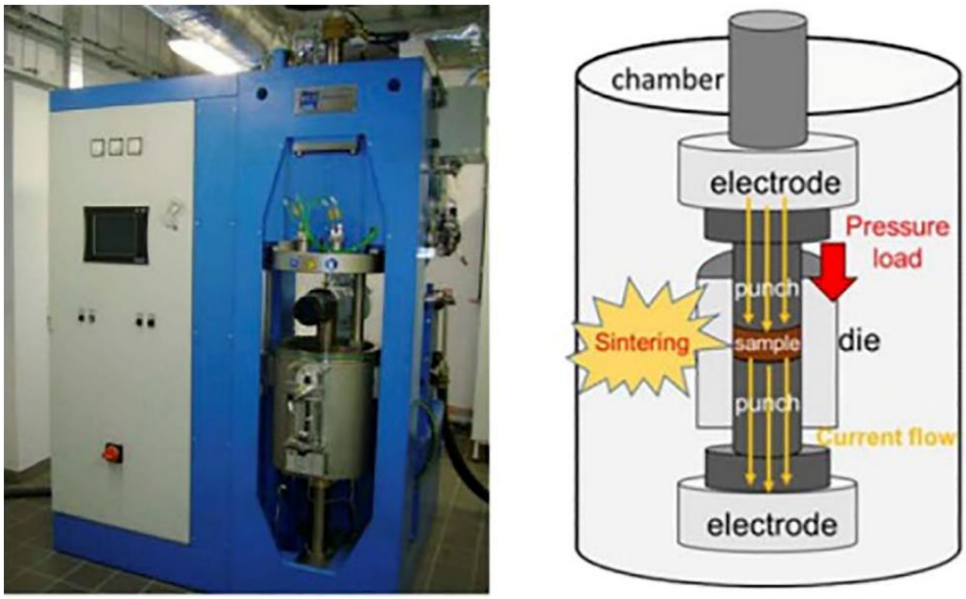

Figure 1.13. Installation for spark plasma sintering (a) and, scheme of SPS heating chamber (b) [20]

Bulk materials that have superconducting properties can also be produced using the high isostatic pressing (HIP) process at high temperatures, however encapsulation is required for densification. The capsule should be inert toward magnesium diboride, hermetized, and soft enough at high temperatures to transfer gas pressure toward the sample's or block's green body. For a large volume, the HIP equipment is fairly complicated and unique.

1.4.5.1. Trapped Magnetic Field (Quasi-Permanent Magnets)

By producing magnetic fields that are several Tesla or larger more than 10, magnetized MgB_2 as well HTS bulks may be employed as quasi-permanent magnets. A magnetic field, which can produce the finest conventional permanent magnets, is substantially (up to an order of magnitude) lower than these values. This makes it possible to use these superconductors in a variety of devices, including flywheel energy storage systems, as permanent magnets.

In the center of two 26 mm diameter samples reinforced using carbon fiber and impregnated with Wood's metal and resin, it has been demonstrated that MT-YBCO

bulks can trap magnetic fields of 17.24 T at about 29 K. Nevertheless, at around 26 K, these reinforced samples shattered. The trapped field of 5.4 T was measured in MgB_2 bulk at 12 K on the surface of a single cylinder (20 mm in diameter) formed by hot pressing ball-milled Mg and B powders. At 17.5 K, 3.14 T can be trapped by a uniaxial stack of two hot-pressed MgB_2 disc-shaped bulk superconductors, each measuring 25 mm in diameter and 5.4 mm in thickness.

The superconductor's mechanical characteristics set a limit on the trapped field of REBCO magnets. It is possible for samples to be destroyed by the Lorentz force. The trapped fields of MgB_2 are lower than those of MT-YBCO at 20 K, however MgB_2 bulks materials have shown trapped fields greater than 3 T. The benefit of MgB_2 superconductors is that they are significantly simpler, less expensive, and need less time to prepare.

In numerous applications, the necessary experimental structure can be formed by stacking multiple rings. For instance, at 20 K, a three-ring stack may block (D30 × h7.5 mm) and trap a field of 2.04 T. A structure made of Mg(I):2B (V) and 10% Ti traps a field of 1.8 T at 20 K at 2 GPa and 900 ◦C for one hour [53].

All the methods noted above open a way to use MgB_2 bulk and thin film superconductors as an element of the setup for physical experiments, electrical machines, medical devices, levitation systems, flywheel energy storage systems, etc.

1.4.5.2. Fault Current Limiters

One potential solution to the fault current issue in power systems is the use of fast-operating nonlinear fault current limiters (FCLs), which enable the limiting of high fault currents because of their ability to quickly increase their impedance. As the temperature, magnetic field, or current increases above their critical values, two characteristics of superconducting materials - an perfect conductivity in the superconducting state with a quick phase transition from this state towards the normal conducting state - form the basis of SFCLs. There are currently no classical counterparts for SFCLs, one of the most alluring uses of superconductors in power

systems [81]. These devices satisfy all power system criteria; testing models, prototypes, and experimental power devices of several SFCL types based on different superconductors has experimentally verified this.

Hollow cylinders and bulk MgB_2 rings can be used as active superconducting components in inductive SFCLs. Figure 1.14 (a) shows the experimental setup and principal inductive SFLC configuration for evaluating the SFCL concept. The SFCL, whose primary coil is coupled in series, has a low impedance under the nominal regime of a protected AC circuit. When the circuit current rises during a fault event, the secondary superconducting coil undergoes a phase transition, which is followed by a rise in the device impedance and, ultimately, a fault current restrictions. High-voltage direct-current (HVDC) systems can also be protected with an inductive SFCL.

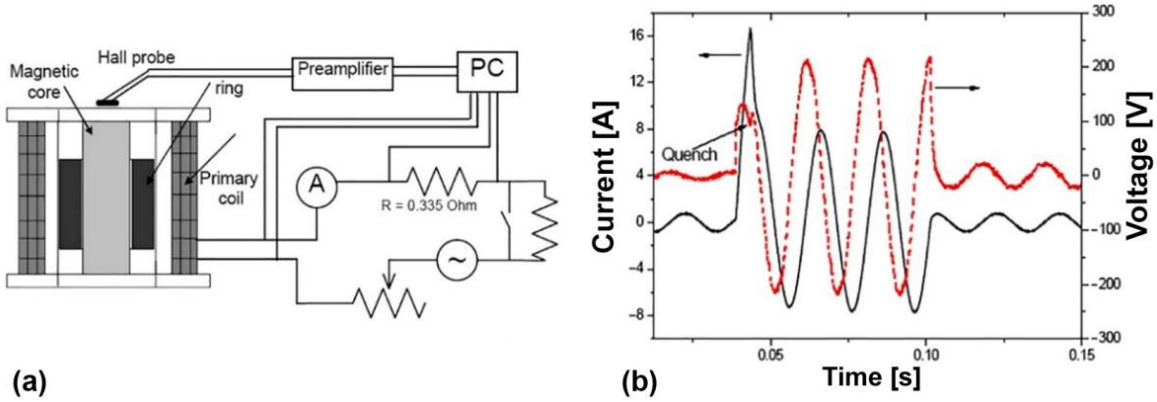

Figure 1.14. (a) The schemes of an SFCL model and a testing circuit for the simulation of a fault event, (b) typical oscilloscope traces of the current in a protected circuit (black, solid curve) and the voltage drop across the primary coil of the SFCL model (red, dashed curve) at 50 Hz and about 4 K [100]

The synthesis settings and ring sizes have no bearing on the oscilloscope traces of the circuit current as well as the voltage drop across the primary coil of the inductive SFCL versions. The superconducting ring does not change into the resistive state when a low, continuous current flows through the protected circuit (nominal regime). The aberrations of the voltage and current curves show up before the initial current maximum at high current (which replicates a fault event) (Figure 1.14 (b)). These

variations are linked to the ring's quenching (critical) current as well as its transition from the superconducting to the resistivity state. Using a variety of methods, starting materials, and enhancements, a collection of FCL models using MgB_2 rings has been constructed and tested with success [100].

The sizes and synthesis parameters of the rings that have been examined as components of an inductive SFCL. It should be noted that a "transport" critical current, AC losses, and voltage–current characteristics can all be measured using the experimental setup for SFCL model testing (Figure 1.14 (a)) [100]. The transition was caused by a quenching current, which was determined to be the "transport" critical current of the different rings. With an outside diameter of 45 mm, a height of 11.6 mm, and a wall thickness of 3.3 mm, Ring 3 had the highest value, 63.200 A/cm^2. The ring was made for two hours at 800 °C and 30 MPa of pressure. The T_c of these rings was calculated to be approximately 38 K based on the magnetization measurements.

1.4.5.3. Electrical Machines

Using superconductors into electrical machines is mostly related to substituting superconducting wires for conventional metal ones in the design. Other kinds of electrical machines with bulk-superconducting rotor elements can now be designed thanks to advancements in the electromagnetic characteristics of bulk superconductors [100]. It has been demonstrated that these devices work well at low as well as medium power levels. Bulk YBCO superconducting elements have been used to create series prototypes of a variety of machine types (trapped field, hysteresis reluctance, etc.) that have been successfully tested throughout a broad temperature range. The world's first motor (1.3 kW) constructed using a bulk high-pressure, high-temperature MgB_2 superconductor was introduced by the authors of . The reluctance motor rotor's superconducting components were manufactured under 2 GPa at 800 ◦C for one hour using MgB_2 - 10 weight percent Ti.

The basic perspective of the zebra-type rotor (superconducting and ferromagnetic layers alternating) of a 1300 W MgB_2-10%Ti motor operating at 210–215 V is shown in Figure 1.14. The motor's efficiency is comparable to that of the MgB_2 motor, according to comparison measurements conducted using MT-YBCO elements at a temperature of 20 K [100]. Systems for the generation, preservation, and transportation of liquid hydrogen would be an essential component of hydrogen energetics. MgB_2 motors and submersible liquid hydrogen (LH) pumps may find their initial use in liquid hydrogen systems.

MgB_2 bulk superconductor-based small- and medium-power electrical motors are less expensive than HTS motors and have shown higher efficiency than conventional motors. Superconducting magnets with trapped fields of 500–600 mT are needed for these pumps. For such purposes, a bulk MgB_2 superconductor operating at liquid hydrogen's temperature is appropriate.

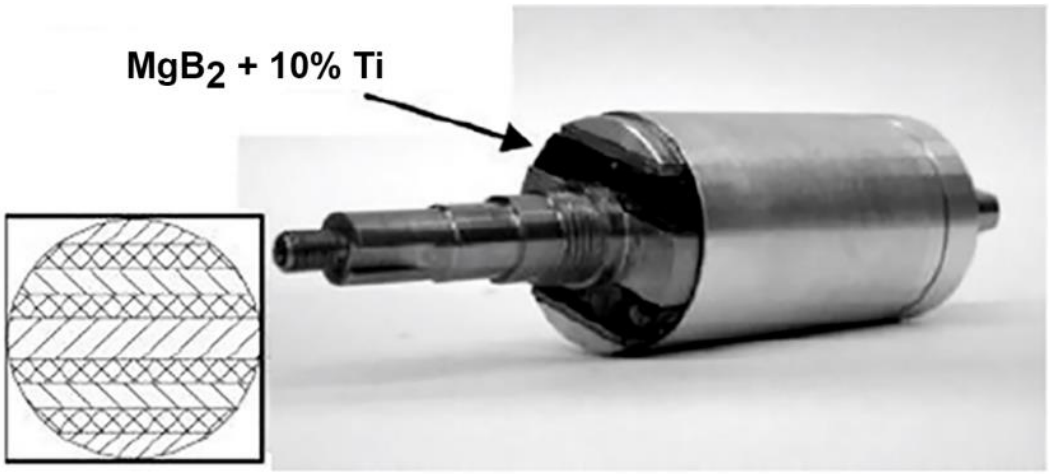

Figure 1.15. General view of azebra-type rotor of a 1300W/215V superconducting motor with MgB_2 bulk superconductor [85]

1.4.5.4. Magnetic Field Shields

Excellent magnetic shielding properties have been demonstrated by bulk MgB_2 superconductors [31], which can be helpful for passively safeguarding a variety of devices (physical setup, medical and measuring equipment, etc.) and even for shielding orbital stations in space from cosmic radiation. Additionally, unlike other

high- or low-temperature superconductors, the basic ingredients are widely accessible and devoid of noble, poisonous, or rare earth elements. The findings from the investigation of several bulk MgB_2 shield designs have been published in the literature [31].

The outcomes of MgB_2 bulk materials' magnetic shield characteristics in the form of a cup are taken into consideration as an example. Up to around 0.8 T, the experimental shielding factors (dots in Figure 1.16 (c)) are essentially unaffected by the applied field. The factor reaches its greatest value, of the order of 105, close to the cup's bottom and is highly dependent on the Hall probe position. The factor at the midpoint, z3, is about 250; in certain situations, this is adequate.

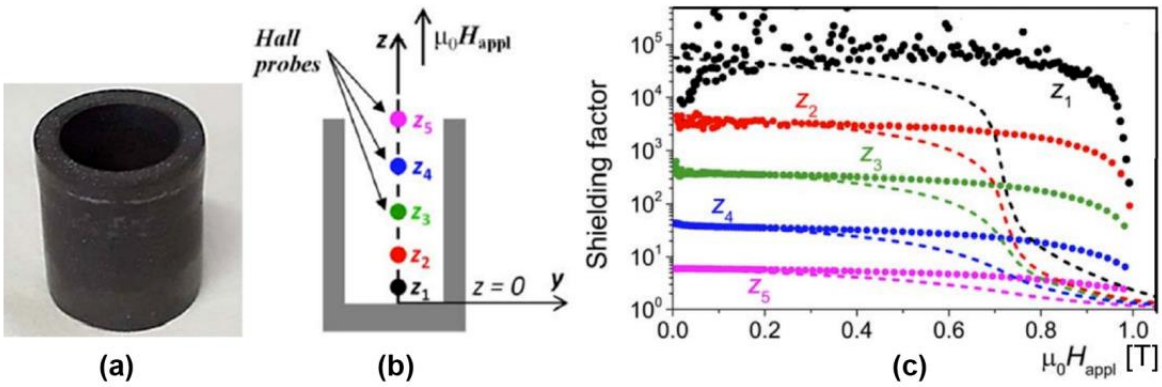

Figure 1.16. (a) Magnetic shield of MgB2 in the shape of a cup, (b) an inner magnetic field measured by a Hall sensor at different z1–z5 positions, (c) The shielding factors at T = 30 K [84]

1.4.6. Enhancements of critical current density of MgB_2 bulk superconductors

Due to benefits of the material, including its high coherence lengths, weak-link-free behavior at grain boundaries, and simple hexagonal crystal structure, this discovery has quickly attracted the attention of researchers worldwide [65,80]. Additionally, MgB_2 is a strong choice for commercial and industrial applications because it is composed of inexpensive and lightweight materials. However, in order to make the material suitable for use in high magnetic field applications, more enhancement of

the J_c is essential. Instead of using natural pinning centers, a variety of approaches and methodologies [23,27] were created to produce factitious pinning centers. *Ex-situ* MgB_2 bulks were sintered at different temperatures and times after varying dopant addition quantities. In addition to coexisting with the superconducting matrix, dopants like Mg and B were expected to function as efficient factitious pinning centers. As a result, this dissertation anticipate that MgB_2 bulk samples will have better intergrain connections and higher J_c. The inclusion of Mg and B may enhance the grain connectivity of *ex-situ* MgB_2 due to its higher bulk density. The genesis of the reinforcing vortex pinning mechanism and the increase in the J_c value [85], or critical current density, were examined using the theory of collective pinning [11]. The size and spacing of the pinning centres exceed the penetration depth due to the manner the magnetic interaction is executed [22]. Other additives have also been added to MgB_2, including graphene [82], carbon nanotubes [90], carbon-based materials [42] and silicon carbide[24]. The idea behind these additions is that they will replace boron with carbon, which is a proven way to increase J_c. Recent studies show that self-feld J_c of MgB_2 bulk samples in the range of $2 – 4 \times 10^4$ A/cm^2. This demonstrates the potential for improved J_c research by optimizing the fabrication and enhancements of J_c of MgB_2 bulk superconductors as presented in Figure 1.17 and Figure 1.18.

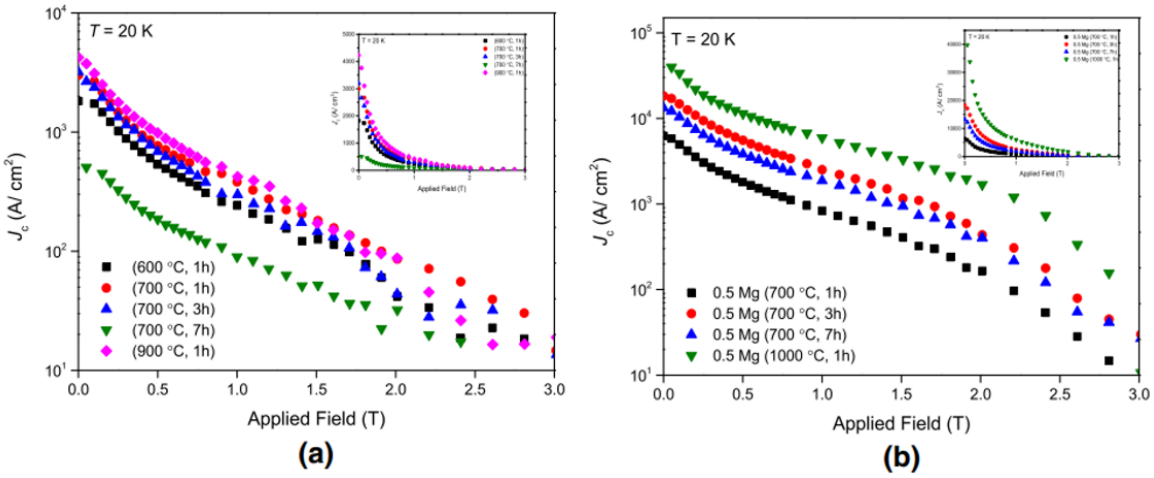

Figure 1.17. Increasing J_c of MgB_2 bulk samples with different fabrication conditions [35]

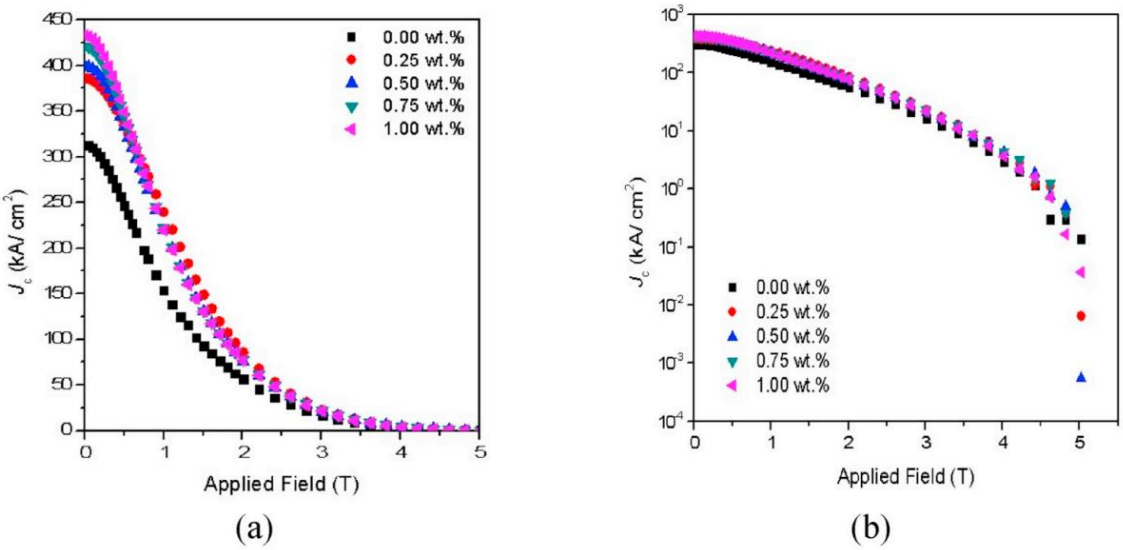

Figure 1.18. Increasing J_c of MgB_2 bulk samples with different doping amounts [59]

1.4.7. Enhancements of critical current density of MgB_2 thin-film superconductors

1.4.7.1. Enhancements of critical current density of MgB_2 thin-film superconductors by using buffer layers

The property of flux pinning of MgB_2 films on buffered hastelloy tapes with different SiC layer thicknesses was investigated in terms of J_c and F_p as delivered in Fig 1.20. The field dependence of J_c of MgB_2 tapes has been shown to improve systematically

as the thickness of the SiC buffer layer increases, whereas J_c values fall. Both the pure MgB_2 and the MgB_2 film with the thinnest SiC buffer layer have two pinning sources, per the investigation of F_p. In contrast, the pinning source seen in the MgB_2 films with thicker SiC buffer layers seems to be distinct from that in the earlier examples. The distinct pinning characteristics of MgB_2 films could indicate the presence of an extra pinning center operating on the thick SiC buffer layers of MgB_2 films. Both Pure MgB_2 and MgB_2 films with a 170 nm-thick SiC buffer layer may be pinned primarily by intra-granular flaws and columnar grain boundaries, according to the microstructural investigations of MgB_2 films. The additional pinning mechanism for MgB_2 films having thicker SiC buffer layers may be the result of carbon diffusion into the MgB_2 film, as determined by Auger electron spectroscopy (AES).

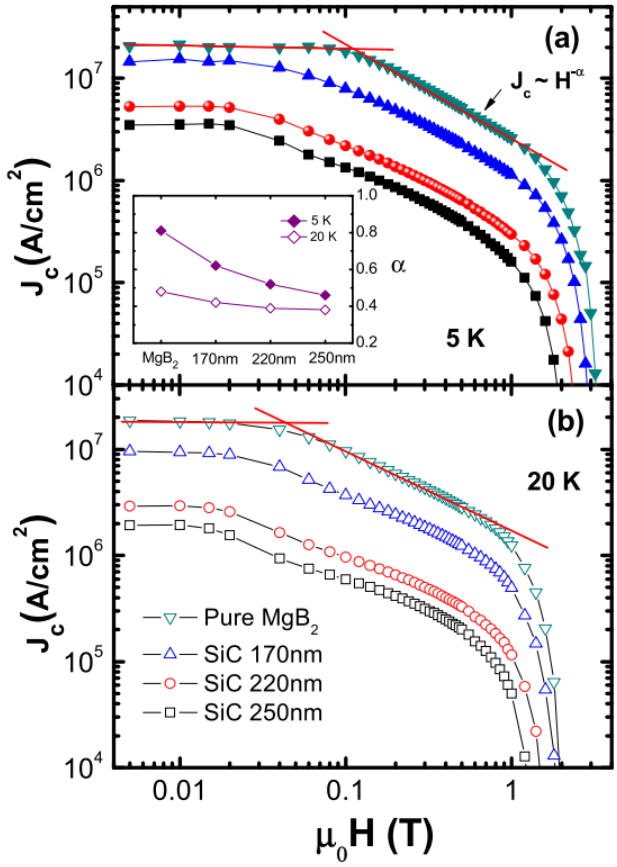

Figure 1.19. Double-logarithmic graph for the field dependence of the critical current density of pure MgB_2 tape and MgB_2 films grown on varied thicknesses of SiC buffered-Hastelloy tapes measured at (a) 5 K and (b) 20 K [57]

With ZnO buffer layers of different thicknesses as given in Figure 1.21, the flux pinning characteristics of MgB_2 films were examined in terms of J_c and F_p. Higher buffer layer thicknesses result in noticeably increased J_c values in the high-field region while having no effect on J_c values in the low- and intermediate-field regions. Depending on the thickness of the ZnO buffer layer, the F_p analysis shows a secondary point-pinning mechanism in addition to primary grain boundary pinning. Furthermore, a strong correlation between the secondary pinning fitting parameter and the Mg and B bond ordering is found, suggesting that flux-pinning enhancement in the high-field region may be facilitated by the local structural distortion of MgB_2 caused by ZnO buffer layers of varying thickness. Finding further benefits of ZnO as

a buffer layer beyond its ability to resist delamination would aid in the creation of a high-J_c MgB_2 superconducting wire for power applications.

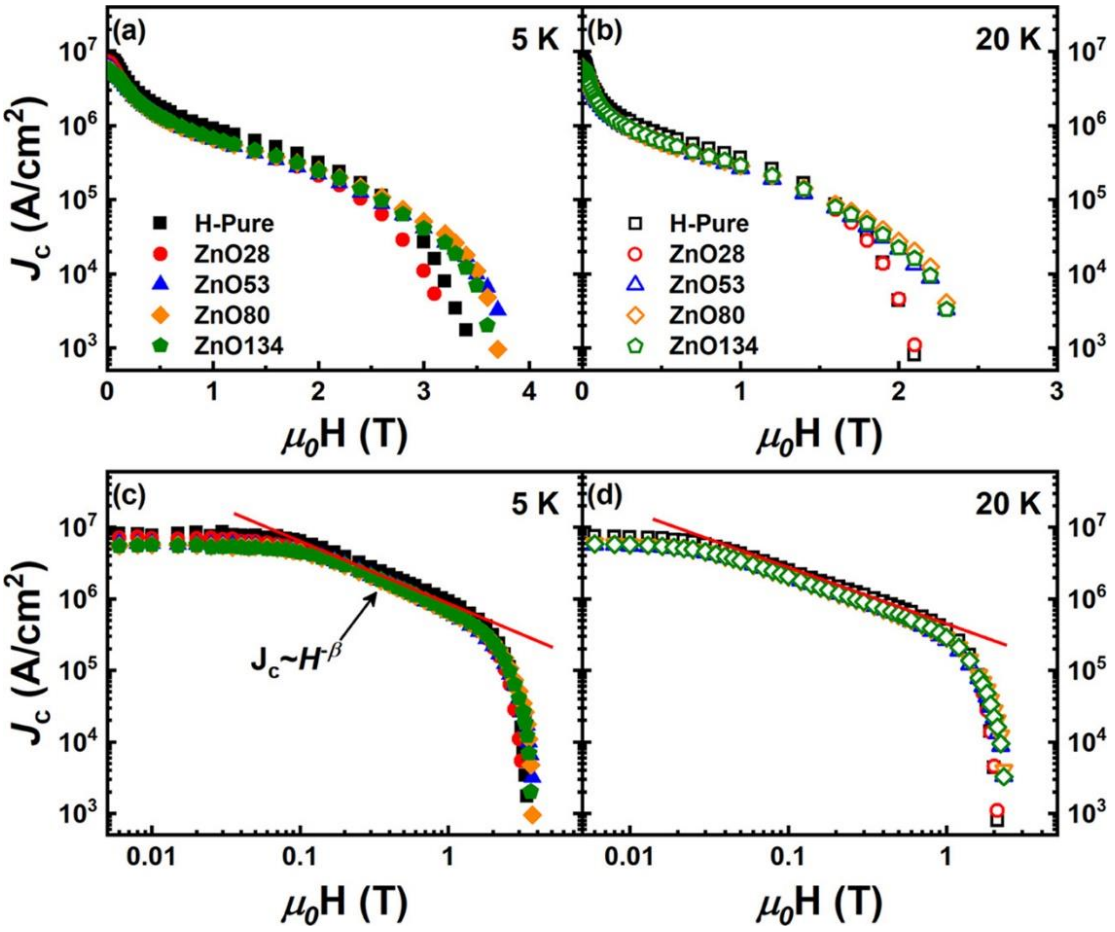

Figure 1.20. Magnetic field dependences of the critical current density (J_c) as a log−linear scale at (a) 5 K and (b) 20 K and as a double-log scale at (c) 5K and (d) 20 K [87]

With polarized Raman spectroscopy, we examined the phonon behavior of ZnO-buffered MgB_2 tapes at normal temperature and cryogenic temperature, with different ZnO buffer layer thicknesses. The boron plane geometry was significantly distorted by lattice mismatch between the MgB_2 film, ZnO buffer layer, and Hastelloy substrate, according to polar plots from integrated angle-resolved polarized Raman spectroscopy (ARPRS) at ambient temperature. This distortion has a major impact on the electron–phonon coupling (EPC) constant, λ, which we computed in relation to the sample's superconducting transition temperature (T_c) using Allen-Dynes'

modified McMillan equation. Our analysis of the E_{2g} mode at cryogenic temperatures revealed a significant phonon hardening effect of up to ~4.1%, which was associated with the thickness of the ZnO buffer layer. Additionally, damping behavior was discovered through line width analysis of the anharmonic E_{2g} phonon mechanism (full width at half maximum), suggesting the existence of another temperature-dependent coupling mechanism within the sample. Traditional EPC estimates underestimate the high T_c mechanism of MgB_2, which may be clarified by this unusual Raman scattering behavior. Furthermore, it is anticipated that thickening the ZnO layer will reduce the distortion in the geometry of the boron plane, which will encourage MgB_2 to become more electron-phonon superconducting by reducing the need for extra coupling mechanisms. Optimizing MgB_2's superconducting characteristics and expanding its useful uses in high-performance superconducting devices would require an understanding of how the ZnO buffer layer affects the phonon dynamics and EPC in the material.

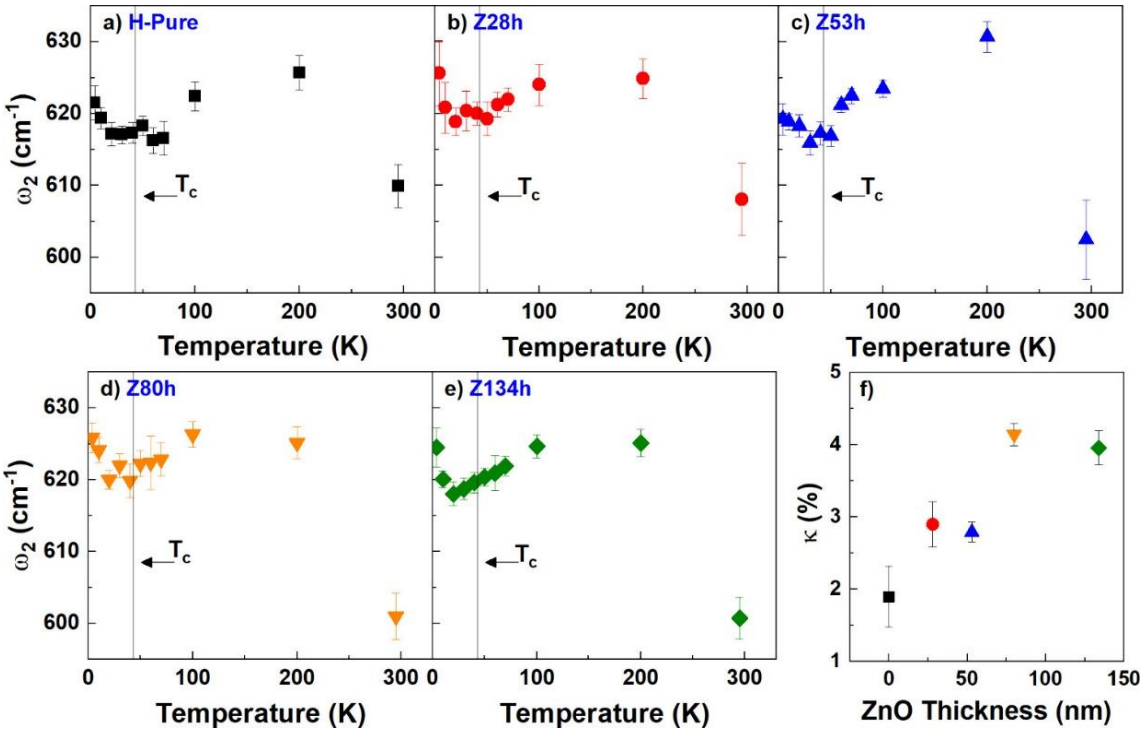

Figure 1.21. The E_{2g} mode (ω_2) of ZnO-buffered MgB_2 tapes with varying ZnO buffer layer thicknesses [86]

1.4.7.2. Enhancements of critical current density of MgB_2 thin-film superconductors by using ion irrradiation

Advantageous features of MgB_2 films include a high T_c of 39 K, a large coherence length, a simple crystal structure, no weak links, low cost, and a high J_c (0) exceeding 10^7 A/cm^2 [39,59,87]. However, their practical uses are hindered by the quick fall in J_c (B) under an applied magnetic field, which is caused by inadequate flux pinning. Ion irradiation has been extensively studied recently for the purpose of producing artificial pinning sites in super conducting materials. Because the lattice disorder induced by low-energy ion irradiation functions as effective point-like pinning sites, it has been reported that light-ion irradiation (e.g., by carbon and oxygen) at low energies (a few hundred keV) significantly improves in-field J_c and B_{c2} in MgB_2 [38,50]. In the meantime, it has been demonstrated that rapid heavy-ion irradiation enhances the in-field J_c of iron-based superconductors and high-T_c cuprates by producing ion tracks, which function as columnar defects . Other research, however, demonstrated that the J_c of MgB_2 was not considerably altered by the high energy (on the order of GeV) implantation of heavy ions (such as gold and silver) [46,79]. However, nothing is known about how MgB_2 films are affected by intermediate-energy (on the order of MeV) heavy-ion irradiation. The highest value J_c of MgB_2 irradiated samples is set at energy 200 keV. This demonstrates the potential to study enhancements of J_c of MgB_2 thin films by ion irradiation at higher level energy of MeV.

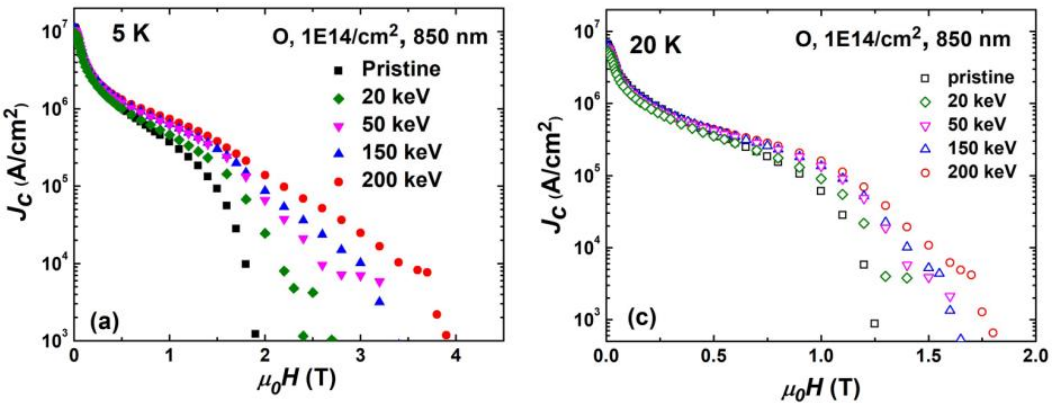

Figure 1.22. Enhancement of J_c of MgB_2 thin films with O ion irradiation [83]

One special method that allows the effects of radiation and other flaws to be investigated in the same sample is irradiation [70]. To verify their use in radiation environments, such as space, fusion processes, and so forth, it is crucial to investigate the effects of radiation on superconductors [70]. Furthermore, although the precise mechanism for defect generation is still up for debate, nuclear stopping of energetic ions is the main way that ion irradiation may cause defects in target materials [43]. Type-II defects are generally beneficial for enhancing superconducting critical qualities, especially in-field J_c, as they can prevent vortex motion. Therefore, understanding how defects impact superconducting fundamental characteristics is critical for superconductor science and technology growth [29].

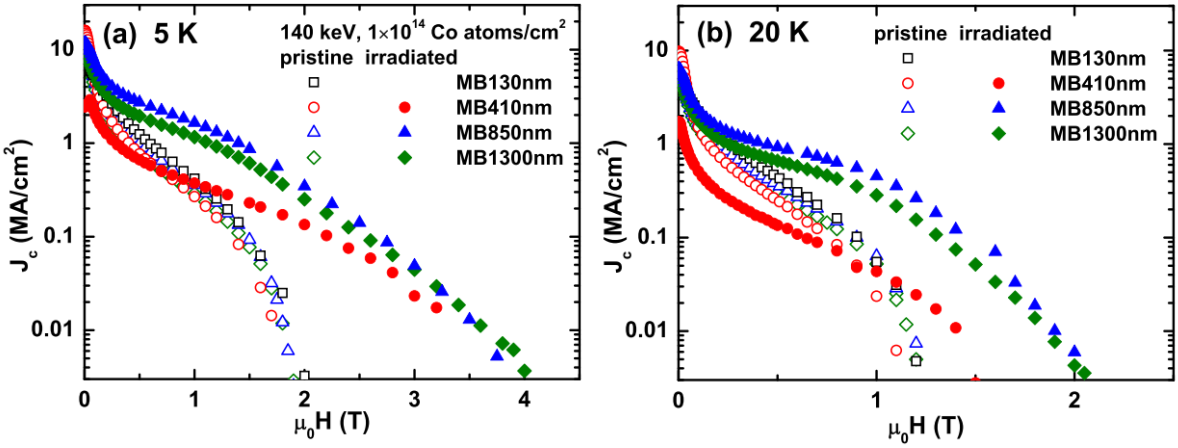

Figure 1.23. Enhancement of J_c of MgB_2 thin films with Co ion irradiation [55]

1.4.8. Subject to be discuss

In comparison to other superconductors, the MgB_2 superconductor has a number of benefits, such as a low cost, two energy gaps, a simple crystal structure, a high self-field J_c. Nevertheless, its practical applications are limited due to its quick decline of J_c in magnetic field.

While high-temperature cuprates and traditional low-temperature superconductors dominated the field for decades, the discovery of superconductivity in MgB_2 in 2001 at $T_c \approx 39$ K opened a unique "middle ground." It offers a significantly higher transition temperature than conventional metallic superconductors (like NbTi) while

maintaining a simpler crystalline structure and lower material costs than cuprates. From a manufacturing perspective, MgB_2 lacks the weak-link grain boundary issues that plague other materials, making it a prime candidate for next-generation MRI magnets, wind turbine generators, and power transmission cables that can operate using liquid neon or closed-cycle refrigerators rather than expensive liquid helium.

The study will involve the synthesis of MgB_2 bulk samples using the *Ex-Situ* reaction methods and MgB_2 thin film samples using HPCVD. The core content will focus on a systematic analysis of how nano-scale defects and dopants influence the vortex dynamics of the material. Experimental work will include X-ray diffraction (XRD) for phase analysis; Physical Property Measurement System (PPMS) testing to determine the superconducting transition and critical current behavior, the Raman spectroscopy provides valuable information about crystal symmetry, particle size, and contaminants; Magnectic force measurement (MFM) to determine the absolute value of the pinning force. The primary objective of this dissertation is to enhance the critical current density (J_c) of MgB_2 samples to make them viable for high-field applications.

The thesis aims to enhance J_c of MgB_2 bulks and thin films. The overall structure of this dissertation is as follows:

- Fabrication conditions for pure MgB_2 bulk superconductors showing high T_c and J_c. Ex-situ MgB_2 bulks were sintered at different temperatures and periods, and this dissertation will investigate the impact of adding different quantities of Mg and B. Sample S5 had the lowest T_c value after adding 0.5 mol Mg then sintering it for an hour at 1000 °C, but its J_c enhancement had the greatest value. After the abnormality was identified, researchers looked into how it related to and affected the superconducting characteristics of MgB_2 samples.
- Enhancing J_c of MgB_2 bulk by co-addition of B_4C and Dy_2O_3. In addition to the previously indicated Mg, trace quantities of B_4C and Dy_2O_3 were added. After limiting Dy_2O_3 to 2 wt%, B_4C was introduced at 5 and 10 weight percent concentrations. Investigating how the coaddition of Mg, Dy_2O_3, and B_4C

affected the crystal structure as well as superconducting characteristics of MgB_2 was the goal of this work. Grain connection was probably enhanced by the coaddition of B_4C and Dy_2O_3, which increases B_{c2} and J_c.

- Enhancing J_c of MgB_2-thin films obtained by ion irradiation. The effects of 2 MeV Sn^{2+} ion irradiation on the T_c, in-field J_c, and B_{c2} of MgB_2 films produced on an Al_2O_3 substrate are discussed in the thesis. The doses range from 2×10^{12} atoms/cm^2 to 7×10^{13} atoms/cm^2. These results imply that the T_c, in-field J_c, and B_{c2} must be modified by the displacement brought about by ion irradiation. The J_c increased with Sn^{2+} ion irradiation at 10 K; the sample with 5×10^{13} atoms/cm^2 had the highest J_c.

Chapter 2: EXPERIMENTAL METHODS

2.1. MgB_2 bulk sample fabrications

2.1.1. Pure MgB_2 bulk sample fabrications

MgB_2 bulk samples are typically prepared using one of two standard methods: *in-situ* [4] or *ex-situ* [88]. During heat treatment, Mg grains melt and diffuse into B grains to generate MgB_2 through a liquid-solid reaction. This is known as the *in-situ* reaction process. This approach produces a sample with a high J_c and a strong intergrain coupling. The introduction of contaminants into MgB_2 during the *in-situ* process greatly increases J_c, much like the cuprate HTS. Mg sites become voids as a result of the liquid-solid transition, resulting in a low bulk density with packing factor of around ~50% . However, *ex-situ* MgB_2, a pre-reacted form of MgB_2 made by the *in-situ* reaction, may achieve a much greater packing factor of around 75%. Despite this, the intergrain coupling of *ex-situ* MgB_2 samples is substantially weaker than that of the *in-situ* ones. Therefore, this dissertation is driven to try to increase the J_c of *ex-situ* MgB_2 by improving its intergrain connection. In order to achieve this, an *ex-situ* MgB_2 bulk was combined with a Mg and B mixture in the ratio of (1.5 Mg + 2 B). Because powder technique eliminates the need for extra chemical dopants, it is cost-effective. Because *ex-situ* MgB_2 has a larger bulk density than *in-situ* MgB_2, the addition of mixed powder (1.5 Mg + 2 B) during the *in-situ* process is anticipated to increase the grain connectivity of *ex-situ* MgB_2 .

To make *ex-situ* MgB_2, commercially available MgB_2 powder (Alfa Aesar, 99.0% purity), boron (B, Tangshan Wei Hao, 97.0% purity), and magnesium (Mg, Tangshan Wei Hao, 99.0% purity) powders was utilized. By applying five tons of pressure using a hydraulic press, the mixture was formed into round pellets about 13 mm in diameter and 1 mm in thickness. The stainless-steel tube was then filled with pellets and sealed at both ends. In order to heat treat the tube, it was finally placed into a tube furnace and heated to 700, 800, and 1000 degrees Celsius, respectively, for one hour while an argon gas flow was constant. The heat treatment serves two purposes: (i) solid-state

self-sintering is projected to improve the cross-section of the grain-to-grain current channel for *ex-situ* MgB_2 [88]; (ii) It maximizes the MgB_2 phase's production *in-situ*, which helps with grain connectivity in (i). Because magnesium is highly volatile at high temperatures, excess magnesium was added to the mixture (1.5Mg + 2B) to make up for the magnesium loss.

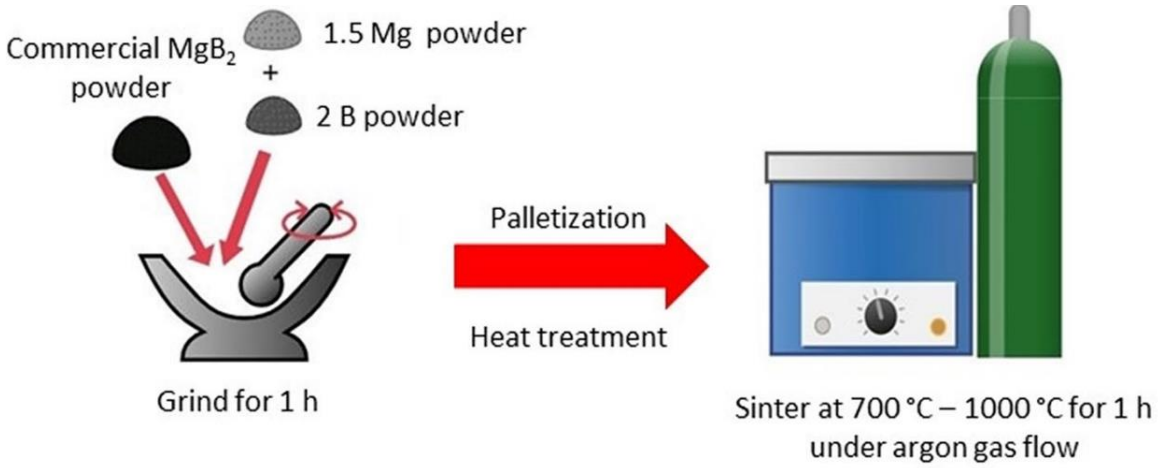

Figure 2.1. MgB_2 bulk sample fabrication diagram

Ex-situ MgB_2 was mixed with 0.5 mol of Mg to form Mg-added samples, based on the stoichiometry of MgB_2 + 0.5 Mg [47,48]. According to the stoichiometry of MgB_2 supplemented with 1.5 Mg + 2 B (30 wt%), 1.5 mol of Mg along with 2 mol of B had been added to bulk MgB_2 samples. For one hour, pure *ex-situ* MgB_2 was sintered at 600 and 700 °C. Regarding the Mg addition-containing *ex-situ* MgB_2 samples, sintering needed 3 hours at 700 °C and 1 hour at 1000 °C. Sintering has been performed for one hour at 700 °C and 800 °C on *ex-situ* MgB_2 samples that had been supplemented with Mg and B (1.5 Mg + 2 B) [48]. We have given the samples names and sample details in the table below for convenience of study.

Table 2.1. MgB_2 bulk samples names and fabrication details

No.	Sample	Sample Name
1	Pure *ex-situ* MgB_2 (600 °C – 1h)	S1
2	Pure *ex-situ* MgB_2 (700 °C – 1h)	S2
3	Pure *ex-situ* MgB_2 + 0.5 mol Mg (700 °C – 1h)	S3
4	Pure *ex-situ* MgB_2 + 0.5 mol Mg (700 °C – 3h)	S4
5	Pure *ex-situ* MgB_2 + 0.5 mol Mg (1000 °C – 1h)	S5
6	Pure *ex-situ* MgB_2 + 30 wt.% (1.5 Mg + 2 B) (700 °C – 1h)	S6
7	Pure *ex-situ* MgB_2 + 30 wt.% (1.5 Mg + 2 B) (800 °C – 1h)	S7

2.1.2. MgB_2 bulk superconductors with co-additions of B_4C and Dy_2O_3

Alfa Aesar provided the 99.0% pure magnesium diboride (MgB_2) powder. In accordance with the stoichiometry of MgB_2 + 0.5 Mg, *ex-situ* MgB_2 was combined with Mg (0.5 mol) as an additional to the pure MgB_2 ceramic that served as the reference sample. MgB_2 samples with 0.5 mol of extra Mg were mixed with varying weight percentages of B_4C. The following are the sample names and details: pure MgB_2 (MgB_2 + 0.5 Mg) as S5-1, (MgB_2 + 0.5 mol Mg + 5 wt% B_4C) as S5-2, (MgB_2 + 0.5 mol Mg + 5 wt% B_4C + 0.5 wt% Dy_2O_3) as S5-3, (MgB_2 + 0.5 mol Mg + 5 wt% B_4C + 1.0 wt% Dy_2O_3) as S5-4, (MgB_2 + 0.5 mol Mg + 5 wt% B_4C + 2.0 wt% Dy_2O_3) as S5-5, and (MgB_2 + 0.5 mol Mg + 10 wt% B_4C + 1.0 wt% Dy_2O_3) as S5-6. After an hour of grinding, the mixture was compacted into spherical pellets that were 13 mm in diameter and about 1 mm thick. To reduce oxidation, the pellets were then put inside stainless steel tubes, covered at both ends, then heated to 1000 °C for an hour while being surrounded by argon gas. All of the powder handling was done in the air. Table 2.2 lists the names and other information of the samples.

Table 2.2. MgB_2 samples co-added B_4C and Dy_2O_3 samples names and fabrication details

No.	Sample	Sample Name
1	Pure MgB_2	Pure MgB_2
2	MgB_2 + 0.5 mol Mg	S5-1
3	MgB_2 + 0.5 mol Mg + 5wt.% B_4C	S5-2
4	MgB_2 + 0.5 mol Mg + 5wt.% B_4C + 0.5wt.% Dy_2O_3	S5-3
5	MgB_2 + 0.5 mol Mg + 5wt.% B_4C + 1.0wt.% Dy_2O_3	S5-4
6	MgB_2 + 0.5 mol Mg + 5wt.% B_4C + 2.0wt.% Dy_2O_3	S5-5
7	MgB_2 + 0.5 mol Mg + 10wt.% B_4C + 1.0wt.% Dy_2O_3	S5-6

2.2. MgB_2 thin film sample fabrications

2.2.1. Hybrid Physical-Chemical Vapor deposition (HPCVD) system

The hybrid physical-chemical vapor deposition approach, which is recognized as an extremely efficient way to create high-quality MgB_2 thin films, was used to fabricate the MgB_2 thin films used in this investigation. Two types of vapor deposition are used in the system: chemical and physical (PVD and CVD). The high Mg vapor pressure required to maintain the thermodynamic stability of the MgB_2 phase at high temperatures is made possible by the HPCVD process [92]. The HPCVD apparatus is schematically shown in Figure 2.2(a).

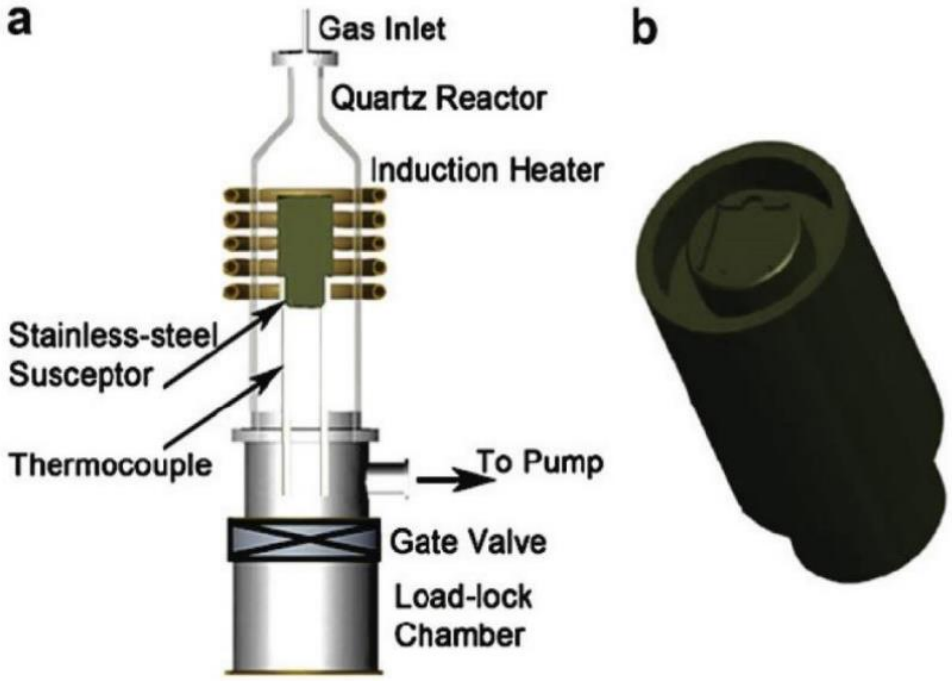

Figure 2.2. (a) Schematic view of the HPCVD system, (b) the susceptor on which substrate is mounted on the top and Mg pieces can be accommodated around the substrate holder [73].

The components of HPCVD include a load-lock chamber, an inductively connected heater, a vertical quartz tube reactor with a bell-shaped inner diameter of 65 mm and a height of 200 mm, a gas inlet and flow control system, pressure maintenance system, temperature control system, and gas exhaust and cleaning system. An induction heater is mounted on the outer edge of the main process chamber, which is coupled to the load-lock chamber at its base. As seen in Figure 2.2(b), a stainless steel susceptor is positioned coaxially inside the reactor. The process chamber and the load-lock chamber are separated by a gate valve. During the production of MgB_2 films, this valve guards against contamination of the process chamber. Diborane (B_2H_6) is used as the boron precursor gas and magnesium pieces as the magnesium sources in the HPCVD process for MgB_2 film formation.

2.2.2. Growth of MgB_2 thin films on Al_2O_3 substrates

The following is a description of the MgB_2 thin-film growing process: A number of occasions, the process chamber was purged using extremely pure (99.9999%) argon (Ar) gas. Subsequently, the reactor was filled with the susceptor, substrate, and a quantity of 99.99 percent magnesium chips (diameter: 2 to 3 mm). Under operating pressure in ambient hydrogen gas (H_2), the substrate and solid magnesium chips that are positioned on the same susceptor are simultaneously heated inductively to the desired temperature. The magnesium bits melt when the temperature reaches the desired level, creating a high vapor pressure near the substrate. Subsequently, the precursor gas B_2H_6 (5% in H_2 gas) is introduced into the chamber and undergoes high-temperature breakdown surrounding the substrate. The following chemical equation describes how the atoms from the broken-down precursor gas interact with the magnesium vapor to form thin coatings on the substrate:

$$B_2H_6 + Mg \rightarrow MgB_2 + 3H_2, \tag{2.1}$$

When the precursor gas is turned off and the susceptor is cooled to ambient temperature in H_2 gas, the deposition process comes to a stop. Since single-crystal Al_2O_3 has the same hexagonal structure as MgB_2 and is useful for real-world applications, it was employed as the substrate in this work. Figure 2.3 illustrates the various morphologies of MgB_2 that may be produced by varying growth parameters, such as temperature, pressure, Mg concentration, growth periods, and so on (columnar structure, ab-plane orientated, flower, nanowire, nanorod, single-crystalline). You may find the growth conditions for them in [73].

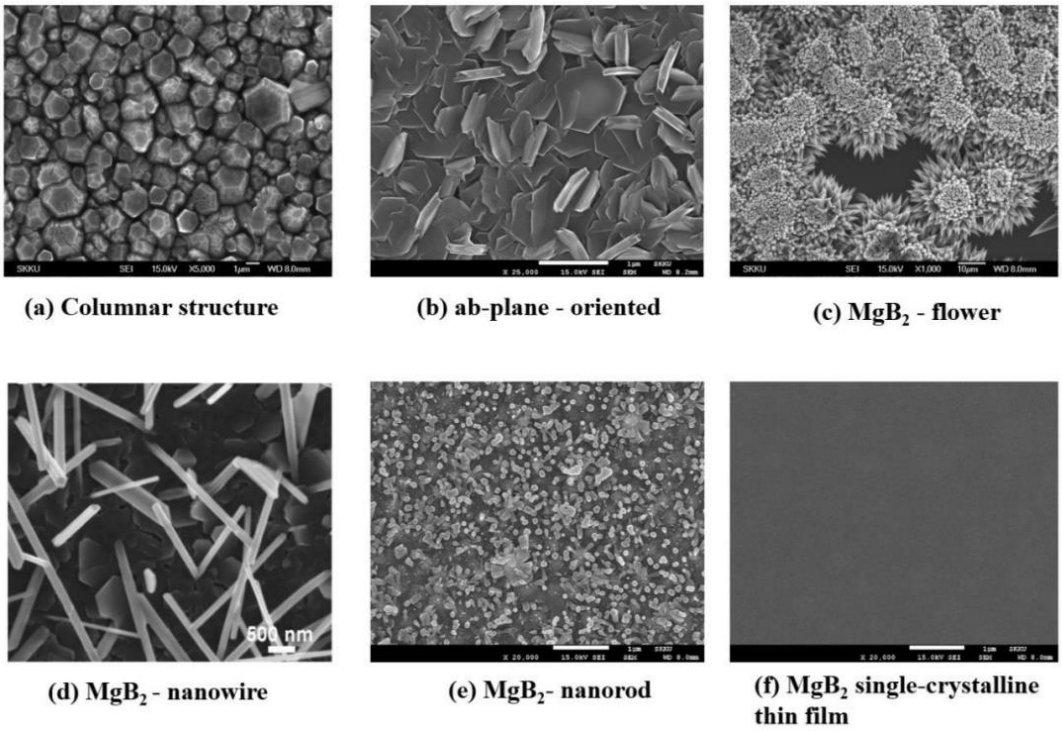

Figure 2.3. Different morphologies of MgB_2 grown on Al_2O_3 substrates using HPCVD [20,73].

The Volmer-Weber growth mode was generally followed by the MgB_2 film's growth mechanism. In such case, the tiniest stable clusters form islands by nucleating on the substrate and growing in three dimensions. Islands of hexagon-shaped MgB_2 initially emerge on the substrate, and as the growth progresses, they grow and unite into a continuous film at a greater film thickness [87]. This growth method led to the formation of columnar structures in the majority of MgB_2 thin films (Figure 2.3(a)). Nevertheless, as Figure 2.3(f) illustrates, we were able to effectively create MgB_2 thin films with single-crystal quality by maximizing the HPCVD growth conditions. Grain boundaries are absent from the films' very smooth surface. The perfect domain-lattice matching between MgB_2 and Al_2O_3 is thought to be the cause of the development of single-crystalline MgB_2 films on sapphire substrates [76]. The characteristics of it will be further investigated and given later. Table 2.3 displayed the growth conditions for singlecrystalline MgB_2 thin films using HPCVD at different thicknesses. In these circumstances, the cohesive interactions between MgB_2 molecules and substrates

might improve and help a bigger single-crystal domain emerge. Superconducting samples of superior quality with few imperfections are essential for a systematic and accurate investigation of the impacts of disorder. In the main portion of this work, we studied the effect of disorder on vortex dynamics using single-crystalline MgB_2 thin films as pristine samples.

Table 2.3. HPCVD growth conditions of single-crystalline MgB_2 thin films with various thicknesses [73,87]

Thickness (nm)	Temperature (°C)	Pressure (Torr)	Flow rate (sccm) ($H_2 - B_2H_6$)	Deposition time (minutes)	Magnesium amount (g)
130	710	210	125-25	4	2.5
410	710	210	100-50	5	2.5
850	710	210	100-50	10	3
1300	710	210	100-50	15	3

2.2.3. Ion irradiation of MgB_2 thin film

Quantized magnetic flux lines (flux lines) that penetrate superconductors in a magnetic field can be immobilized to control the in-field J_c. Pining centers (PCs) are crystalline imperfections and impurities in the specimen that impede the mobility of flux lines. Therefore, one important tactic to enhance the in-field performance of superconductors is to artificially implant crystalline imperfections as efficient PCs. Doping non-superconducting secondary phases to create effective PCs in MgB_2 thin films has been an attempt over the past fifteen years or so.

The size, distribution, direction, and dimensionality of PCs all affect the flux pinning effect. Specifically, as Figure 2.4 illustrates, the dimensionality of PCs has a substantial impact on the flux pinning feature. One-dimensional PCs, like columnar defects (CDs), for instance, show a preference direction for flux pinning: along their long axis, the magnetic field direction is where the intense flux pinning takes place. In contrast, three-dimensional PCs, like nanoparticles, have morphologies that lack associated orientation for flux pinning, which produces an isotropic pinning force

against any magnetic field direction. The change of the J_c properties of MgB_2 thin films is significantly influenced by these PC characteristics; their size and shape, for example, should be tailored to each application's needs.

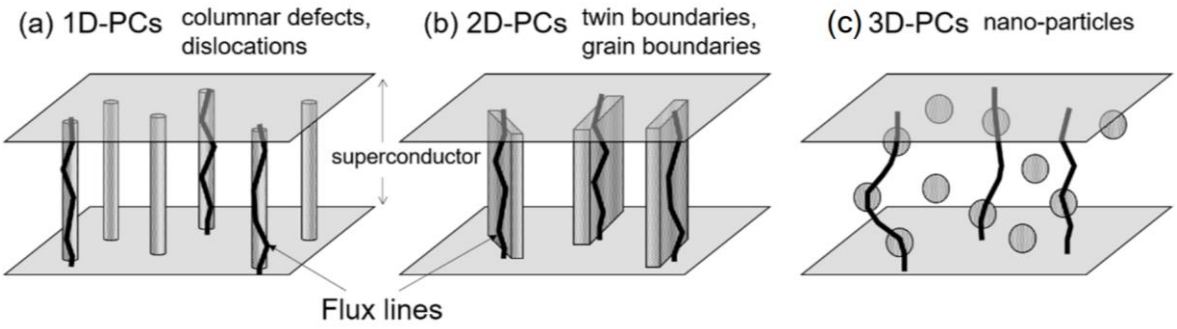

Figure 2.4. The different dimensional categories for PCs: (a) 1D columnar (linear) defects, (b) 2D planar defects such as twin boundaries, and (c) 3D nano-particle [83]

High-T_c superconductors exposed to fast heavy-ion irradiation create amorphous CDs of damaged material parallel to the projectile direction by employing the electron excitation method rather than the nuclear collision process. In reality, the CDs produced by radiation serve as one-dimensional PCs. The orientation of the one-dimensional PCs determines the preferred direction of flux pinning. Therefore, it is projected that heavy-ion irradiation will change the anisotropy of J_c in high-T_c superconductors by changing the direction of irradiation. Additionally, the size and form of CDs are greatly influenced by the electronic stopping power Se, which is the energy loss of the damaging ion per unit of length by using electronic excitation in the target material. Whereas continuous CDs with thick diameter form with higher Se beyond a particular value, discontinuous CDs with thin diameter are detected at intervals along the ion route at lower Se. In particular, discontinuous CDs may provide more effective flux pinning across a wide magnetic field angular band since their ends can operate as PCs throughout magnetic field directions slanted from their long axis. Consequently, the discontinuity of CDs has a strong effect on the direction-

dispersion of CDs and the modification of the J_c anisotropy in high-T_c superconductors.

One important advantage of utilizing heavy-ion irradiation for CD creation is that it allows for the preparation of any CD configuration by varying the irradiation intensity and the incidence direction without requiring sample manufacturing (see Figure 2.5). This is due to the fact that the pinning structure may be efficiently constructed to meet the requirements of different applications, which would be advantageous for the development of coated conductors with excellent performance. Furthermore, we might be able to discover new physics of flux line dynamics because to the distinctive pinning structures that the irradiations have created. The design criteria for the optimal pinning landscape can be provided by heavy-ion irradiation to high-T_c superconductors, which can increase the potential for flux pinning and put J_c near the assumed threshold of critical current density, also referred to as the pair-breaking critical current density.

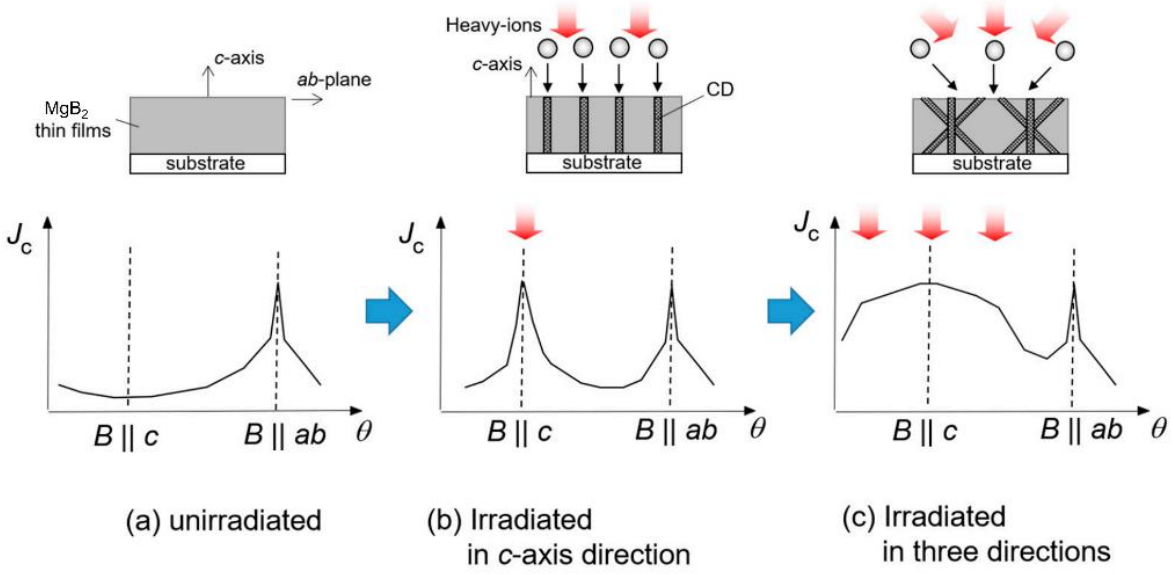

Figure 2.5. Modification of the J_c anisotropy by controlling the irradiation directions (a) typical J_c anisotropy of unirradiated high-T_c superconductors, (b) modified J_c anisotropy with CDs along the c-axis, (c) modified J_c anisotropy with direction-dispersed CDs [83]

On c-cut Al_2O_3 substrates, MgB_2 that is 412-nm thick and highly c-axis orientated was created by utilizing a hybrid physical-chemical vapor deposition technique (HPCVD). High-purity (99.99%) magnesium particles were positioned on a susceptor together with an Al_2O_3 substrate. Using pure H_2 gas at a flow rate of 80 sccm, the susceptor was inductively heated to 700 °C at 80 Torr. Film deposition was started by supplying B_2H_6 (5% in H_2) gas at a flow rate of 20 sccm once the temperature had stabilized. Ion irradiation was carried out at room temperature using the HUS-5SDH-2 twin pelletron accelerator systems provided by the VNU University of Science in Vietnam (Figure 2.6).

Figure 2.6. The HUS-5SDH-2 tandem pelletron accelerator system at the VNU University of Science in Vietnam

Light-ion irradiation (e.g., carbon and oxygen) under low energies (a few hundred keV) considerably enhances in-field J_c and B_{c2} in MgB_2. This is due to the lattice disorder caused by low-energy ion irradiation, which serves as effective point-like

pinning sites [39,63]. In the meantime, it has been demonstrated that rapid heavy-ion irradiation enhances the in-field J_c of iron-based superconductors and high-T_c cuprates by producing ion tracks, which function as columnar defects. Other research, however, demonstrated that the J_c of MgB_2 was not considerably altered by the high energy (on the order of GeV) implantation of heavy ions (e.g., silver and gold) [46,79]. The effects of intermediate-energy (MeV) heavy-ion irradiation on MgB_2 films, however, have not been well studied.

The Monte Carlo simulation software of the Stopping and Range of Ions in Matter (SRIM) was used to calculate the average projected ranges (Rp) as well damage events of the Sn^{2+} ions [93,94]. 2 MeV of energetic Sn^{2+} ions had been exposed to doses of 2×10^{12} (2E12), 2×10^{13} (2E13), 5×10^{13} (5E13), and 7×10^{13} (7E13) atoms/cm^2 at a tilting angle of 7° in order to prevent channeling effects. The names and details of the samples are listed in the following chapter.

According to an SRIM simulation, the concentration of Sn ions irradiated onto a 412-nm-thick MgB_2 thin film on c-cut Al_2O_3 substrate peaked at the estimated mean projected range R_p = 612 nm of 2 MeV Sn ions, as shown in Figure 2.7. (a). The majority of the ions are found in the Al_2O_3 layer after passing through the MgB_2 layer. The MgB_2 layer exhibits a comparatively consistent total number of target vacancies (Figure 2.7.b), indicating that heavy ions can efficiently generate lattice displacements.

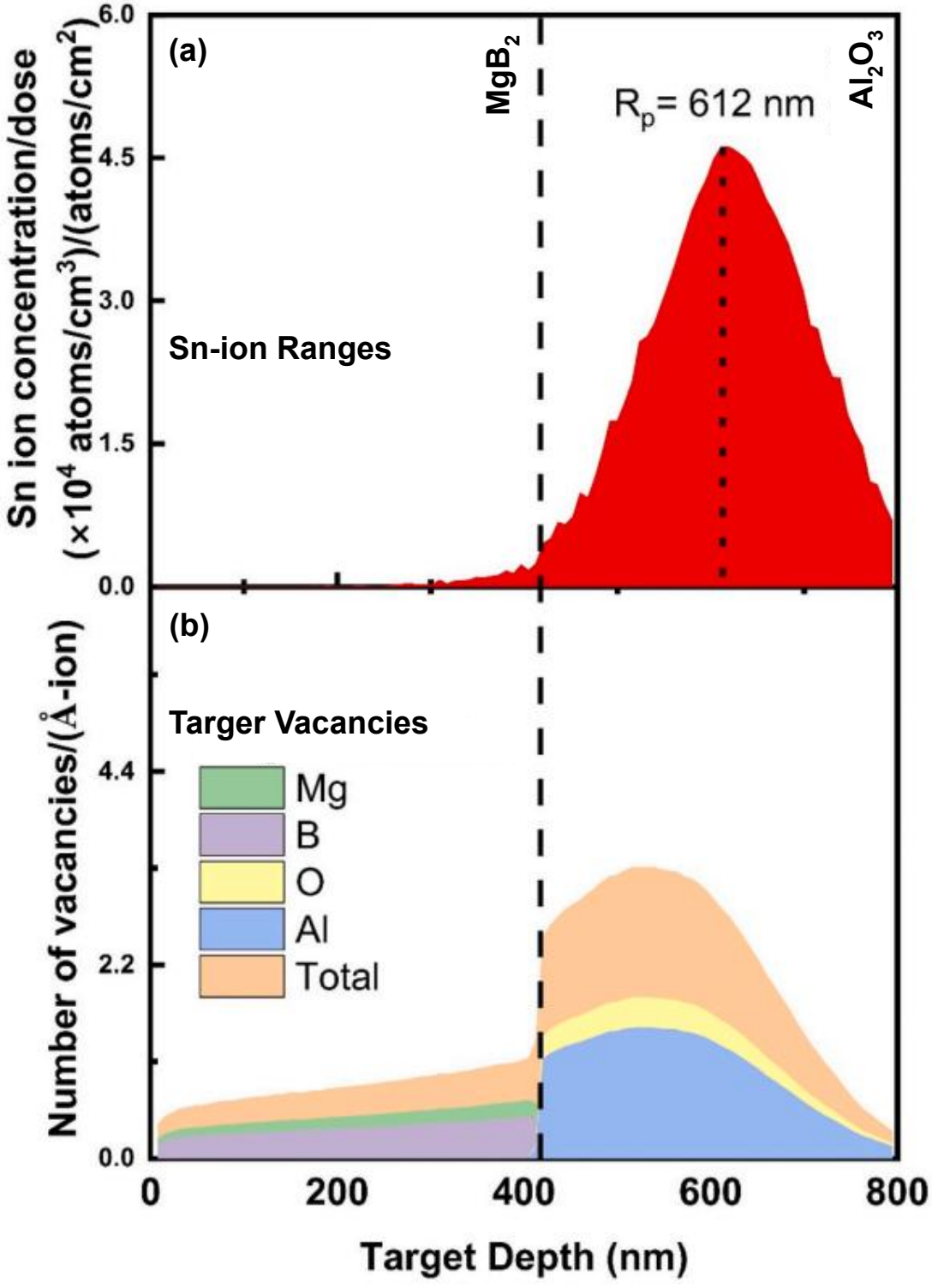

Figure 2.7. (a) Range of 2 MeV Sn ions irradiated into 412 nm thick MgB_2 film grown on c-cut Al_2O_3 substrate, (b) number of target vacancies created by 2 MeV Sn-ion irradiations as a function of target depth [49]

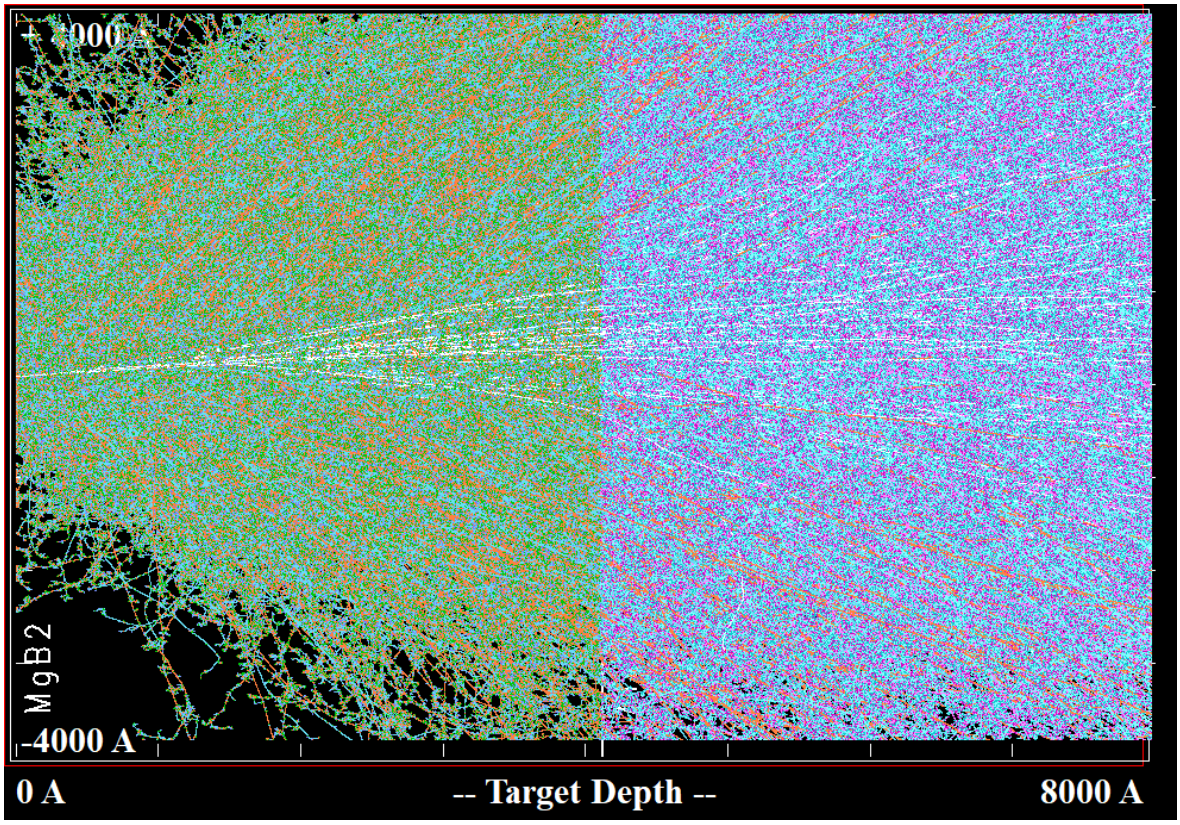

Figure 2.8. 2 MeV Sn ion distribution using STRIM

2.3. Measurement methods

2.3.1. X-ray diffraction (XRD)

One method for examining the crystal structure of materials is X-ray diffraction (XRD). The atoms in the crystal lattice interact with the X-rays when they are directed at a crystalline substance, causing the atoms to scatter, or diffract, the X-rays in different directions. It is possible to identify and examine the pattern of scattered X-rays to ascertain the atomic arrangement within the crystal lattice. Bruker D8 Advance model at Faculty of Physics, VNU University of Science was used to determine the crystal structures of MgB_2 bulk and thin films. The study is predicated on the constructive interference of a crystalline sample with monochromatic X-rays: A cathode ray tube produces the Xrays, which are then focused, collimated, and directed toward the sample after being filtered to produce monochromatic radiation.

When Bragg's Law is satisfied, the incident rays' interaction with the sample results in constructive interference as well as a diffracted beam [12]:

$$n\lambda_{\mathrm{Cu-K}\alpha} = 2dsin(\theta) \tag{2.2}$$

where n is the reflection order, $\lambda_{\mathrm{Cu\text{-}K}\alpha}$ is the radiation wavelength, d is the interplanar spacing of the crystal and θ is the angle of incidence. This law links the diffraction angle and lattice spacing in a crystalline sample to the wavelength of electromagnetic radiation. This experiment involved gradually rotating the sample to alter the incident angle of the X-ray source (CuKα) to the sample. In order to identify the diffracted X-ray, a detector was rotated twice the incidence angle. The distinctive fingerprint of the crystals included in the sample is provided by the distinctive x-ray diffraction pattern produced during a standard XRD investigation. This fingerprint can be used to identify the crystalline form when it is correctly read and compared to conventional reference patterns and measurements.

The measured XRD data was treated in the following steps: background determination, profile fitting, as well refinement using the Rietveld technique. The phase identification was determined using the Inorganic Crystal Structure Database (ICSD) along with the Crystallography Open Database (COD).

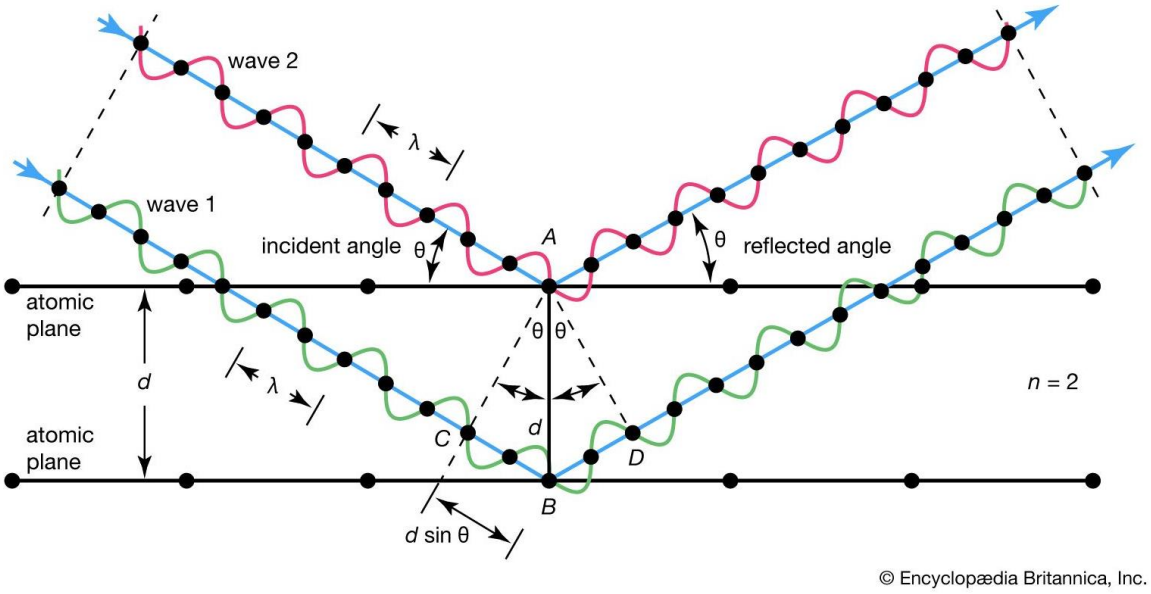

Figure 2.9. Bragg's Law reflection [12]

Using Bragg's law and Miller's indices, the lattice constants of MgB2 have been calculated for a tetragonal structure [75]:

$$\frac{1}{d_{\mathrm{hkl}}^2} = \frac{4}{3}\left(\frac{h^2 + h.k + k^2}{a^2}\right) + \frac{l^2}{c^2} \tag{2.3}$$

where d_{hkl} is the interplanar spacing, h, k, l are Miller's indices and a, c are lattice constants.

2.3.2. Physical property measurement system (PPMS)

2.3.2.1. DC susceptibility

A direct current (DC) field can be used to conduct susceptibility measurements, which provide information on the static magnetic characteristics. The measurements of DC magnetization (M). The Quantum Design PPMS EverCool II systems' vibrating sample magnetometer (VSM) option was used for these measurements, which were carried out with an applied field of 10 Oe perpendicular to the surface. Using zerofeld cooled conditions, T_c was measured between 10 and 50 K with a 10 Oe applied feld. The "critical temperature", or T_c, was the temperature that was where the susceptibility departed from linearity.

2.3.2.2. Resistivity vs. temperature measurement

The transport characteristics of MgB_2 bulk and thin films were measured using a physical property measurement system (PPMS, Quantum Design). In this system, a magnetic field of up to ±9 Tesla may be applied, and temperature can be constantly changed between 1.9 K and 400 K. We utilized PPMS's resistivity function to measure electro-transport. The resistivity option PPMS puck with 12 linked channels is displayed in Figure 2.10 (a). Following sample mounting on pucks, the PPMS probe the system's central component was installed. The PPMS probe's schematic perspective is displayed in Figure 2.10 (b). Furthermore, by utilizing a revolving puck to alter the angle between the magnetic field and the sample's plane, PPMS can measure the angle-dependent signals.

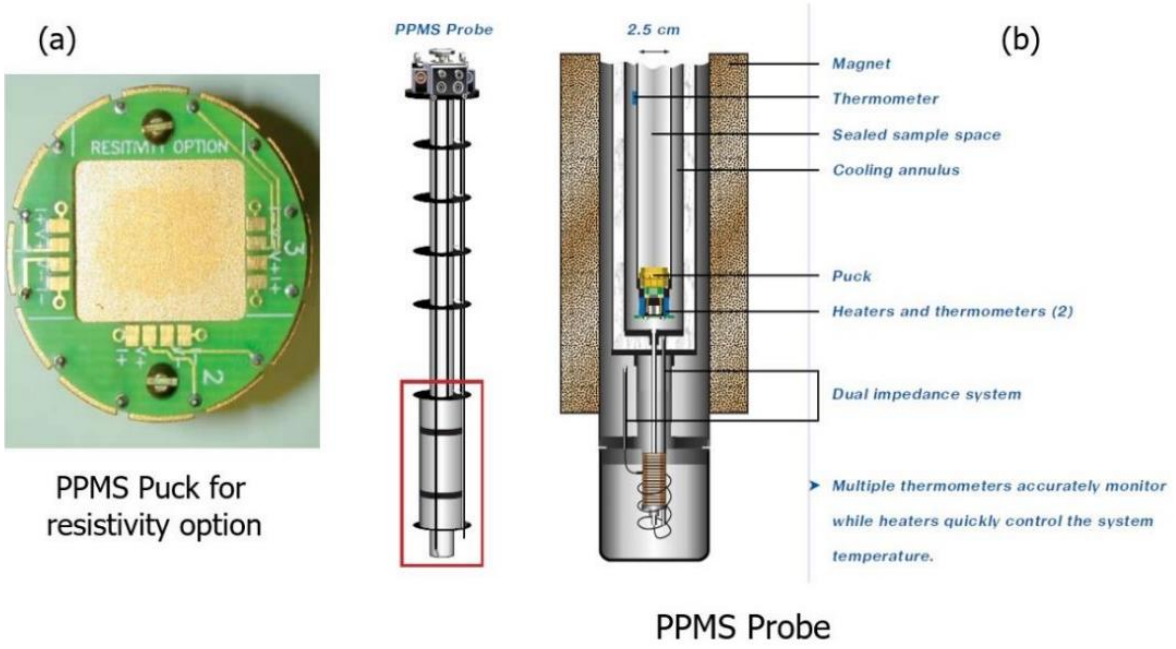

Figure 2.10. (a) The PPMS puck for resistivity option, (b) the schematic view of PPMS probe [36].

2.3.2.3. Magnetization vs. field measurement

This dissertation also used the PPMS to perform the magnetization of MgB_2 bulk and thin films. It is possible to apply a magnetic field of up to ± 5 Tesla and regulate the temperature continuously between 2 K and 400 K. With a resolution of less than ~ 10^{-8} emu, the SQUID sensor is the brains of the PPMS. A Physical Property Measurement System (PPMS) is a multipurpose laboratory tool that may be used to measure a variety of materials' physical characteristics at different magnetic fields and temperatures. Since the PPMS is a cryogen-free system, liquid helium is not necessary for its operation. The PPMS consists of a superconducting magnet, a cryostat, as well a number of measurement instruments and accessories. The sample is cooled to low temperatures using a cryostat, and high magnetic fields are produced using a superconducting magnet. Numerous physical characteristics of the sample are measured using the measurement probes and accessories. The Bean's critical state model was used to calculate the J_c of the magnetization hysteresis (M-H) loop.

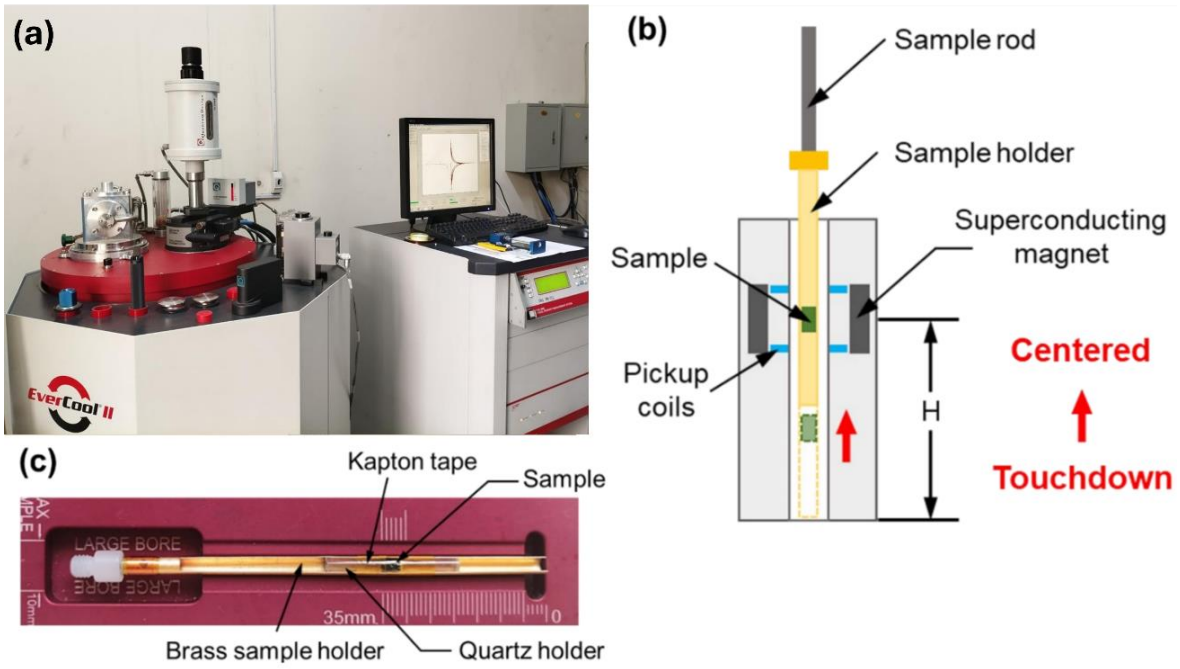

Figure 2.11. (a) The Physical Property Measurement System (PPMS), (b) the interior schematic diagram of the standard coilset puck and the touchdown centering operation, (c) the configuration of the mounted sample [26].

According to this model, each filament located within the sponge both carries the critical current or zero at all. The inner filaments are protected from an external magnetic field by surface barrier current. Only at that time the surface barrier current reaches its critical value can the field flow through. When the field is raised, filaments around the center begin to transport the critical current, and the flux finally reaches the sample's core. All of the filaments experience current flow when the field is lowered to zero, trapping the flux within the sample. The critical current in the filaments gradually reverses when a field is applied in the other direction. By using the Ampere's law: $\nabla \times B = \mu_0 J_c$ and the magnetic flux density expression: $B = \frac{1}{V}\int Hdv$, the Bean's formula was defined as $J_c = 30\Delta M/d$, where $\Delta M = M^+ - M^-$ is the width of hysteresis loop, d is the characteristic length [9].

The Bean's model was adjusted as follows for the bulk samples [9]:

$$J_c = \frac{20\Delta M}{a\left(1 - \frac{a}{3b}\right)} \tag{2.4}$$

where a and b are the sample dimensions perpendicular to the magnetic field. The M^+, M^-, and ΔM practical estimation was described in Figure. 2.12.

The Bean's model was adjusted as follows for the thin film samples [9]:

$$J_c = \frac{30\Delta M}{r} \tag{2.5}$$

where r is the radius corresponding to the total area of the film surface perpendicular to the magnetic field and ΔM is the height of the M − H curves.

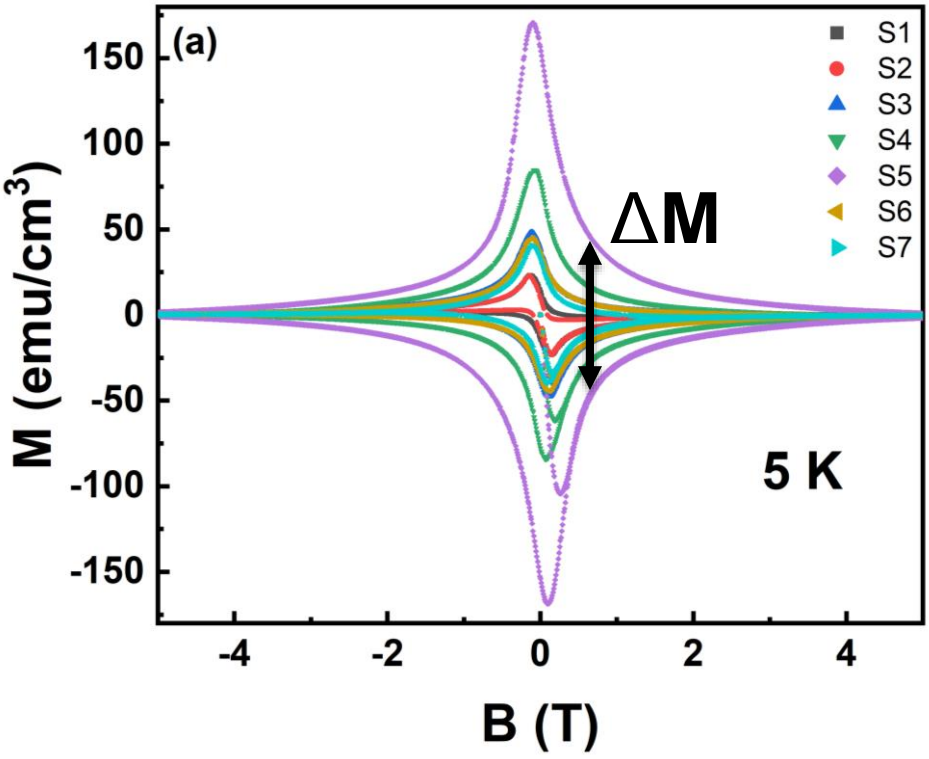

Figure 2.12. Illustration of estimation of ΔM from the half of a hysteresis loop of a MgB_2 sample

2.3.3. Electron-phonon coupling constant in MgB_2 superconductors

Despite the fact that the boron plane provides a significant portion of MgB_2's superconducting properties, the active mode of Raman (E_{2g}) is closely tied to band

electronic transport. In consequently, the E_{2g} mode can be effectively examined using the Raman spectrum, which may yield valuable information on crystal symmetry, particle size, and contaminants.

The Raman spectra were measured at room temperature using the WITec Micro-Raman Spectrometer System (model ALPHA300 M), which has an incident green laser using a 531.97 nm wavelength, 600 g/mm grating, and a Raman shift range of 200-1000 cm^{-1}.

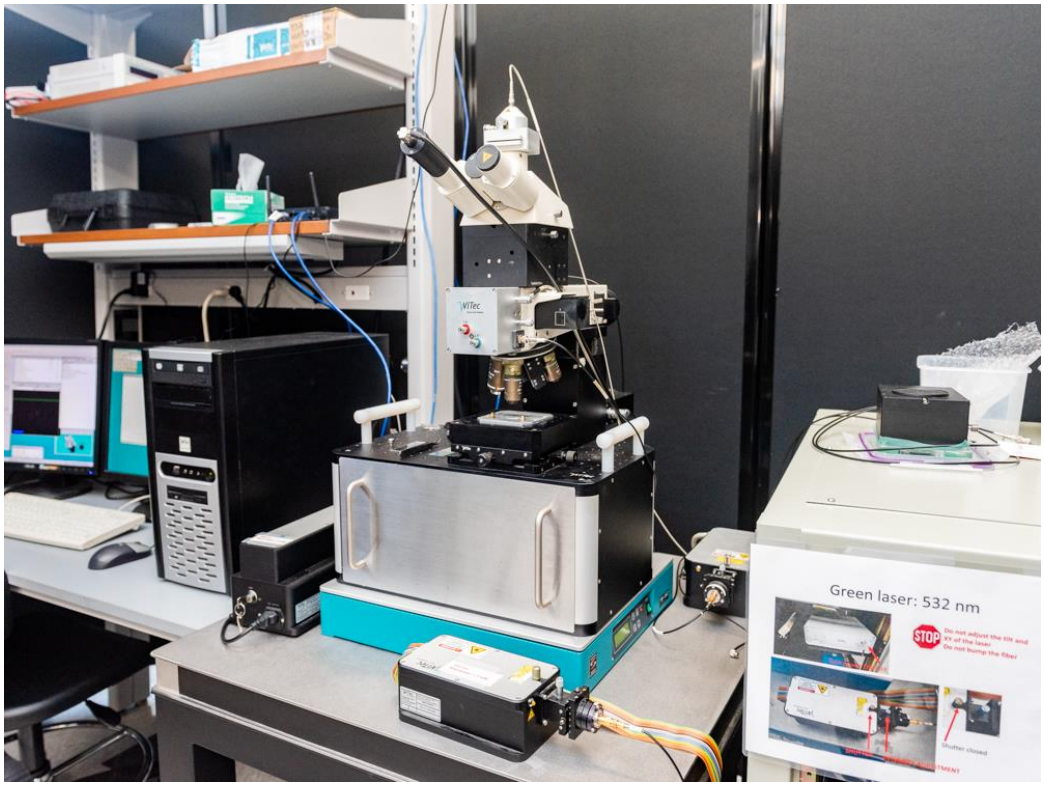

Figure 2.13. Witec Micro-Raman Spectrometer Alpha 300

According to the McMillan formular [55], the average phonon frequency and critical temperature are inversely related. Therefore, the E_{2g}, which is the active frequency of the phonon of mode in MgB_2 has an analogous effect on T_c fluctuation. Allen-Dynes modified the McMillan formula used to test the BCS theory [2], in order to fully comprehend the contribution of the E_{2g} mode to the T_c value in our MgB_2 samples:

$$T_c = \frac{\langle \omega_{\log} \rangle}{1.2} \exp\left(-\frac{1.04(1 + \mathrm{EPC})}{\mathrm{EPC} - \mu^*(1 + 0.62 * \mathrm{EPC})} \right) \tag{2.6}$$

where $\langle\omega_{log}\rangle = (690 \times \omega^2_{E2g} \times 390)^{0.25}$ is the E_{2g} mode mean phonon frequency , the MgB_2 superconductor system has a phonon frequency of 390 cm^{-1} and 690 cm^{-1} for other modes. EPC illustrates the electron–phonon (e-ph) coupling constant, and the value of μ*, the Coulomb pseudopotential, is assumed to be 0.13 [91].

2.3.4. Magnectic force measurement

Characterizing how superconductors behave in the presence of magnetic fields is crucial for understanding and comparing fundamental characteristics in various classes of superconductors, from heavy fermion systems to high temperature cuprate and pnictide to conventional metallic, as well as for identifying and improving materials for applications.

Our objective is to determine the absolute value of the pinning force for single Abrikosov vortices and to directly explore the spatially resolved absolute value of the London penetration depth using our special He-4 MFM with vector magnet capabilities and a simple comparing method.

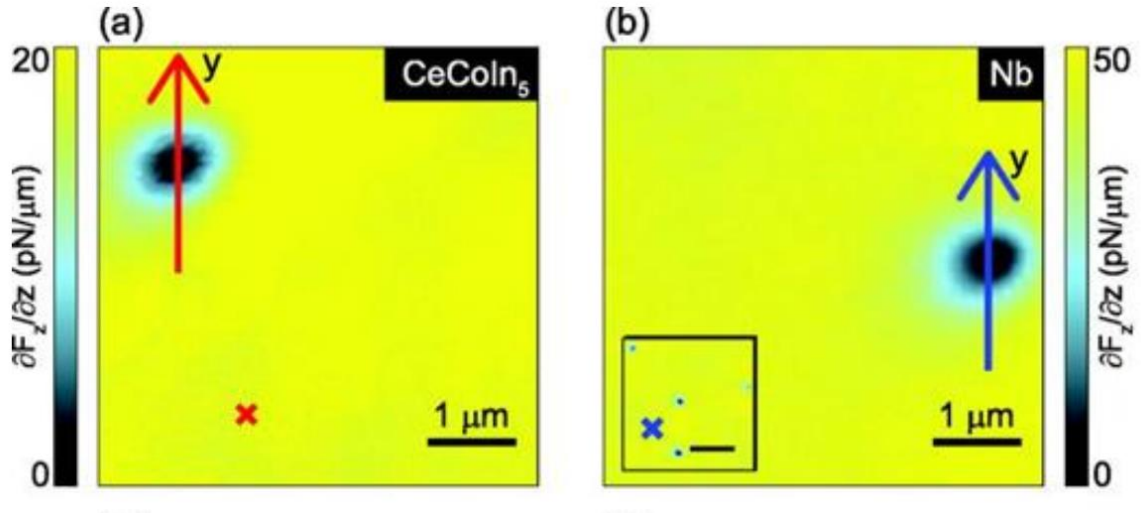

Figure 2.14. MFM image of (a) $CeCoIn_5$ and (b) Nb obtained in the superconducting state at T = 0.5 K with a tip-sample lift height of 300 nm [84].

Chapter 3: FABRICATIONS OF PURE MgB_2 BULK SUPERCONDUCTORS

Within this chapter, the superconducting characteristics of MgB_2 bulk samples produced under various circumstances were examined. The purpose of this chapter is exploring the condition which might help to fabricate MgB_2 bulk samples showing high T_c and high J_c compared to another resaearch. *Ex-situ* MgB_2 bulk samples were sintered at various temperatures and periods after being further combined with Mg and B in varying proportions. The contributing factor of electron-phonon coupling constants (EPC) has been studied using Raman spectroscopy. To examine the superconducting properties, the dependency on the magnetic field of magnetization (M(H)) and the temperature of magnetization (M(T)) were assessed. The contribution of EPC, whose value is nearly proportional to the variation of critical temperature, was calculated using the McMillan formular, which is modified by Allen-Dynes, and the frequency of phonon centered in the mid peak center ω_2 (E_{2g}). Raman spectrum investigation revealed that the MgB_2 bulk sample supplemented with 0.5 mol Mg then sintered at 1000 °C for an hour had the lowest EPC value, which was 1.094. The sample also had the highest critical current density and the lowest critical temperature. Applying the collective pinning theory, the small bundle field (B_{sb}) and the big bundle field (B_{lb}) were derived, showing that, under the right sample fabrication conditions, the small and large bundle regimes expand. According to the normalized small bundle field (b_{sb}) and normalized critical current density (j) temperature dependency, δT_c pinning is the most common flux pinning mechanism in all MgB_2 bulk samples. By examining the pinning properties, the Dew-Hughes model verified that the addition of Mg and B causes surface pinning in the matrix.

Therefore, this dissertation will investigate how the T_c, J_c, and volume pinning force F_p are affected by adding different amounts of Mg and B to *ex-situ* MgB_2 bulks that were then sintered at different temperatures and periods. The application of Raman spectroscopy, a non-destructive chemical analysis method, was used to ascertain the

impact of distinct phonon characteristics on T_c because MgB_2 is a phonon-enabled superconductor. Different bulk samples of MgB_2 were analyzed to determine how the disorder effect and EPC changed over time [6,50]. Raman spectroscopy was used to systematically investigate the EPC behavior in order to study the T_c variations of *ex-situ* MgB_2 bulks. Sample S5 had the lowest T_c value after adding 0.5 mol Mg then sintering it for an hour at 1000 °C, but its J_c enhancement had the highest value. These findings suggest that adjusting the T_c, J_c, and F_p mechanism depends critically on the displacement caused by the insertion of Mg and B as well as the sintering temperature. Additionally, the EPC obtained through the Raman spectroscopy technique and its relationship to superconducting properties were investigated. After the disorder was identified, researchers looked into how it related to and affected the superconducting characteristics of bulk MgB_2 samples. The samples are provided in Table 3.1 along with their names and descriptions.

Table 3.1. Details of MgB_2 bulk samples names and fabrication conditions

No.	**Sample**	**Sample Name**
1	Pure *ex-situ* MgB_2 (600 °C – 1 hour)	S1
2	Pure *ex-situ* MgB_2 (700 °C – 1 hour)	S2
3	Pure *ex-situ* MgB_2 + 0.5 mol Mg (700 °C – 1 hour)	S3
4	Pure *ex-situ* MgB_2 + 0.5 mol Mg (700 °C – 3 hours)	S4
5	Pure *ex-situ* MgB_2 + 0.5 mol Mg (1000 °C – 1 hour)	S5
6	Pure *ex-situ* MgB_2 + 30 wt.% (1.5 Mg + 2 B) (700 °C – 1 hour)	S6
7	Pure *ex-situ* MgB_2 + 30 wt.% (1.5 Mg + 2 B) (800 °C – 1 hour)	S7

3.1. Effect of sample fabrication conditions on T_c of MgB_2 bulk superconductors

One of the most important key factors which has been used to determine the superconductivity of the samples is value of T_c. In this chapter, the superconducting transition and values of T_c were deduced from M(T) measurement. Figure 3.1 displays the normalized DC susceptibility of the samples as a function of temperature. Data were gathered between 10 K and 50 K while a 1 mT magnetic field was present. A significant degree of homogeneity and crystallinity was indicated by the sharp transition seen in all samples [59]. The temperature wherein the susceptibility deviated from linearity was determined to be the value of T_c. The value of T_c fell precipitously to 38.1 K (for sample S5) after stabilizing at 38.5 K (for samples S1, S2, S3, as well S4). Following that, T_c progressively rose to 38.6 K for sample S6 and 38.8 K for sample S7. The manufacturing of MgB_2 bulk has been carried out by adding Mg and raising the sintering temperature, which would greatly minimize the formation of MgO secondary phase, as was previously reported where Mg as well SiC were added [83], respectively. Additionally, MgB_2 breakdown was inhibited and grain coupling was improved. Consequently, a smaller decrease in T_c might be achieved. The slight alteration in T_c is consistent with the samples' lattice structure having very little deformation. The MgB_2 structure-inducing disorder in lattice locations can be introduced by additions. The transition temperature is lowered by the disorder. The distribution of oxygen as well as hydrogen in the material structure, as well as the creation of grains of higher borides, can likely be influenced by the additives and sintering temperature, which in turn might affect the superconducting properties. It would be credited with being the cause of S5's lowest T_c. However, it also showed that raising the sintering temperature will cause the sample to become more homogeneous, or connected between grains, which is likely to result in a dramatic change in the S5 sample [34,58].

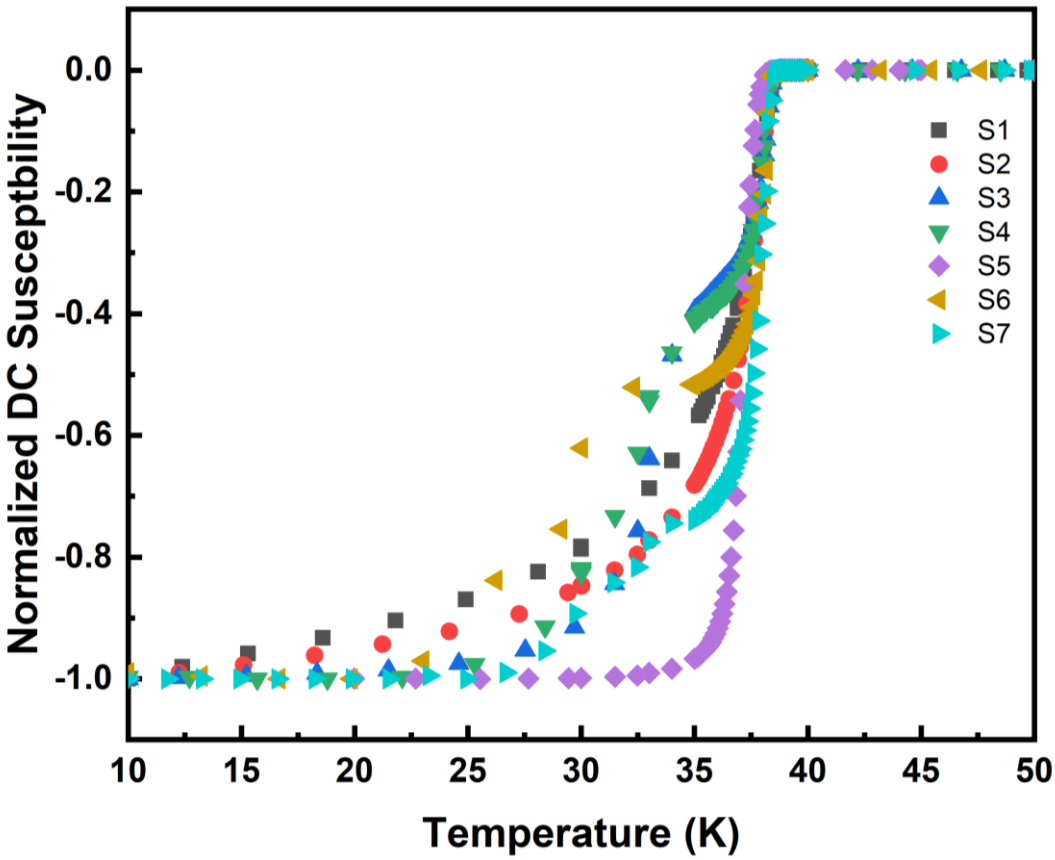

Figure 3.1. Normalized DC susceptibility for ex-situ MgB_2 bulk samples produced under various circumstances as a function of temperature.

Additionally, the T_c variation of MgB_2 was significantly impacted by the alteration of strain-induced local structure, i.e., the disorder and deformity of the crystal lattice [15]. The unfinished reaction that occur between Mg and B while the heat treatment following the addition may be the origin of the second transition in Figure 3.1, which shows inhomogeneity within the samples. Because *ex-situ* MgB_2 particles impede the diffusion of Mg and B in the mixture, their presence may slow down the formation of the MgB_2 phase. A single-step transition was noted for the S5 sample, which is in line with the sample's increased J_c as a result of improved grain connection. To gain a thorough knowledge of the T_c change, measurements and analyses of Raman spectroscopy of MgB_2 bulk samples were conducted.

3.2. Explaining the possible reason for the changes in values of T_c of MgB_2 bulk superconductors

It has been well known that the variations of T_c of MgB_2 superconductors were likely to link to the formation of lattice distortions [12,51,56,71]. Basing on these previous investigations, the possible reason for the changes in values of T_c of the MgB_2 bulk superconductors obtained in Figure 3.1 was going to explained in Figure 3.2. Given that MgB_2 is a phonon-mediated superconductor, electron–phonon interactions are consistent with the pairing mechanism that gives it its superconductivity. Among the optical modes of MgB_2, including A_{2u}, B_{1g}, E_{1u}, and E_{2g}, the E_{2g} phonon mode is the only initial-order active mode [89]. The shorter phonon ridge, which is primarily located at 455–490 cm^{-1}; the intermediate phonon ridge, which mainly focuses at 560–610 cm^{-1} (mode E_{2g}); along with the greater phonon ridge, which is largely focused at 740–800 cm^{-1}, are contained in a Raman shift peak that is around 200–1000 cm^{-1}. The Raman spectra of MgB_2 also showed a broadening of the E_{2g} ridge due to the higher phonon density of MgB_2 superconductors [51]. Despite the fact that the boron plane accounts for the majority of MgB_2's superconducting characteristics, the Raman active mode, or E_{2g} mode, is strongly related to the electronic transport of bands. As a result, the E_{2g} mode can be effectively examined using the Raman spectra, which may yield valuable data on particle size, impurities, as well crystal symmetry. Raman scattering is significantly impacted by residual stress along with disorder [15], which can also alter phonon lifespan and phonon frequency. A broad Raman optical mode at approximately 600 cm^{-1} to 630 cm^{-1} was found by measurements [71]. It is anticipated that the E_{2g} mode frequencies will be around 665 cm^{-1} (82 meV) and 515 cm^{-1} (64 meV) [44]. The Raman shift peak at the active phonon mode (E_{2g} mode) oscillated at approximately 560–610 cm^{-1}, which is consistent with the data above.

Figure 3.2 depicts the Raman spectrum measurement results of the *ex-situ* MgB_2 bulk samples also demonstrates the addition of Mg and B. The E_{2g} peak's intensity rose while its half-width fell in samples S1 and S2. In the range of 570.72 and 573 cm^{-1}, the E_{2g} peak barely moves. Samples S3 and S4 show a decline in E_{2g} peak intensity

although a rise in peak half-width for samples S3 through S5. Compared to samples S3 and S4, sample S5's E_{2g} peak has the largest amplitude despite a notable drop in intensity. In comparison to samples S1 and S2, the optimal location of E_{2g} has moved to the right in samples 579.40, 580.23, and also 582.08 cm^{-1}. The E_{2g} shift was evident in all three of the 0.5 mol Mg added MgB_2 samples, including S5. The observed shift has most likely been caused by lattice distortions. While the half-width reduced for samples S6 as well as S7, the E_{2g} peak intensity rose suddenly. Furthermore, samples S6 and S7 showed a shift to the left in their E_{2g} peak positions, dropping to 572.21 and 567.34 cm^{-1}, respectively, with sample S7 exhibiting the lowest E_{2g} peak position. Figure 3.3 (a) shows the change in the location of the E_{2g} peak and T_c. The T_c of samples S1 and S2 is same, and the E_{2g} peak's location is almost unchanged. The peak location of E_{2g} changes somewhat in samples S3 through S5, but samples S3 and S4 share the same T_c of 38.5 K. In sample S5, however, the ideal location of E_{2g} quickly moves to the right as T_c drops. As seen in examples S4 and S5, the ideal location of E_{2g} moves to the right and rises from 580.23 to 582.08 cm^{-1} when T_c decreases from 38.5 K to 38.1 K. T_c rises from 38.6 K to 38.8 K for samples S6 and S7 as the location of the E_{2g} peak falls. Consequently, a considerable decrease in E_{2g} is the cause of the observed decline in T_c. The locations of the E_{2g} peaks in each sample are listed in Table 3.1. This change might be explained by lattice distortions caused by the inclusion of Mg and B. This effect has been seen in both bulk and thin-film samples of MgB_2 [51,87]. The existence of strong electron-phonon (e-ph) coupling constant (EPC), phonon-phonon (ph-ph) interaction, and lattice relaxation at the Mg and B impurity site might all be responsible for the shift in the E_{2g} peak's intensity, breadth, and location. This outcome is somewhat similar to the change in T_c.

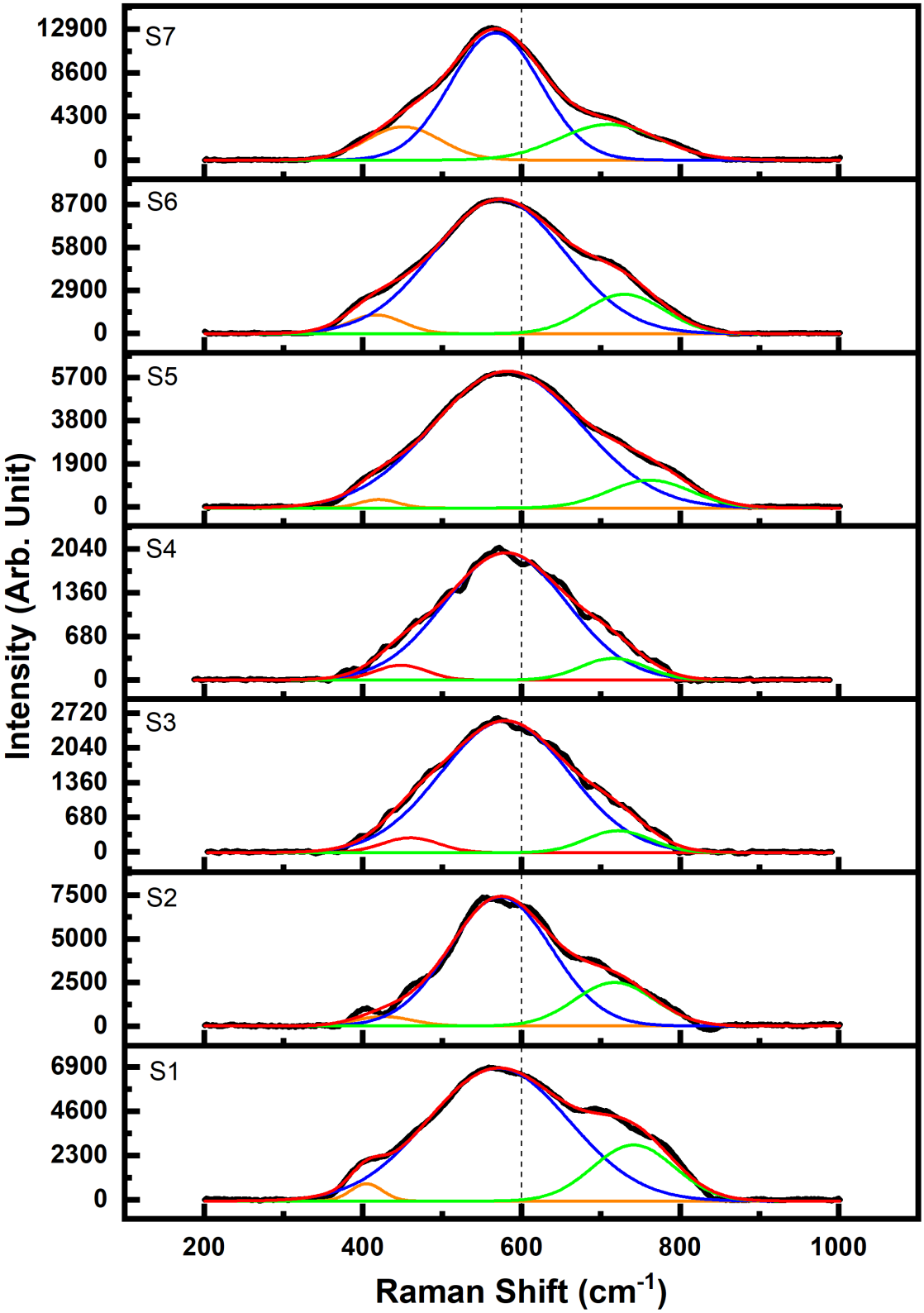

Figure 3.2. Raman spectra of ex-situ MgB_2 bulk samples made under various circumstances, fitted to the E_{2g} mode (blue), the shorter and larger phonon ridge (orange and green).

To get the quantitative analyses, the theoretical model relating T_c and EPC is going to use. Critical temperature is inversely related to the average phonon frequency, according to the McMillan formula [54]. Consequently, the active frequency of the phonon of the E_{2g} mode in MgB_2 has an analogous effect on T_c fluctuation. In order to fully comprehend the contribution of the E_{2g} mode to the T_c value in our MgB_2 bulk samples, the BCS theory was assessed using the Allen-Dynes-revised McMillan formular [2]:

$$T_c = \frac{\langle \omega_{\log} \rangle}{1.2} \exp\left(-\frac{1.04(1 + \mathrm{EPC})}{\mathrm{EPC} - \mu^*(1 + 0.62 * \mathrm{EPC})} \right), \tag{3.1}$$

where $\langle \omega_{\log} \rangle = (690 \times \omega^2_{E2g} \times 390)^{0.25}$ is the E_{2g} mode overall phonon frequency, with the phonon frequency of the remaining modes in the MgB_2 superconductor system is 390 cm^{-1} along with 690 cm^{-1} [44]. The Coulomb pseudopotential (μ*) of 0.13, coupled with EPC, represents the electron-phonon (e-ph) coupling constant. The method may be used to determine EPC values for all ex-situ MgB_2 bulk samples by taking the critical temperature T_c value provided in Figure 3.1 and the frequency of the E_{2g} mode indicated in Figure 3.2. Figure 3.3 (b) depicts the change in EPC values and T_c. The EPC value first falls from 1.102 to 1.094, then rises to 1.109 and 1.116. S5 has the lowest T_c as well as EPC values (1.094). Therefore, the decrease in T_c brought about by the addition of Mg and B is caused by the decrease in the Raman shift as well as the EPC value, which decreases as the Raman shift gets better. Similar to this, a disorder that occurs when Mg and B are added to *ex-situ* MgB_2 bulk samples is the cause of higher impurity rates. The EPC constant is reduced in relation to changes in the electronic system brought on by a disturbance that impacted MgB_2's superconducting mechanism.

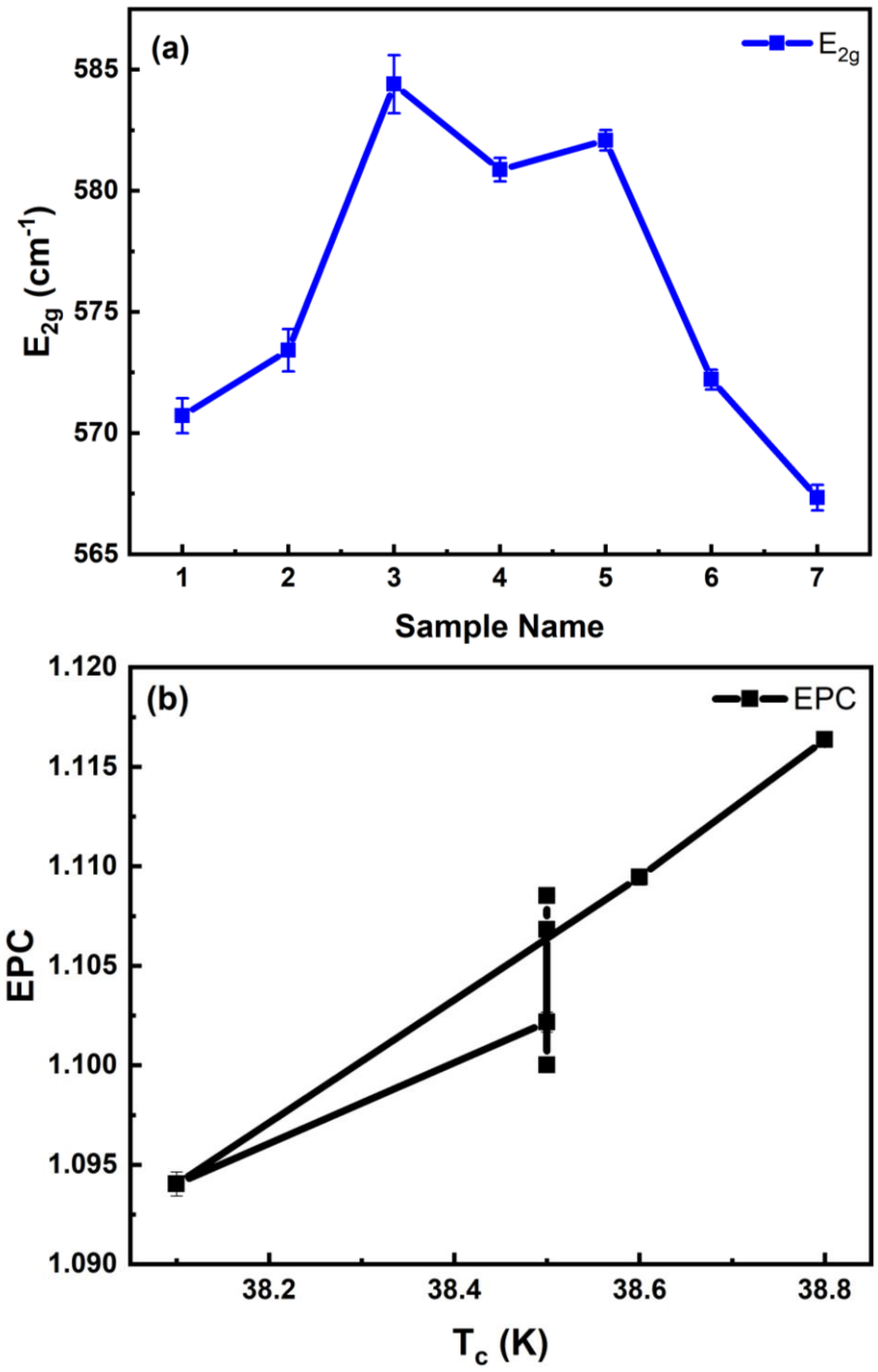

Figure 3.3. (a) Dependence of the E_{2g} peak position on sample fabrication condition, (b) Dependence of the electron–phonon coupling constant (EPC) on the critical temperature (T_c)

The Raman spectra of *ex-situ* MgB_2 bulk samples is often significantly influenced by the incorporation of Mg as well as B fluence. Due to the variations in the E_{2g} peak brought on by the hardness and softening of phonon, the incorporation of Mg as well

as B to MgB_2 acts as a phonon-toughening and phonon-loosening layer. The results of fitting a Gaussian distribution to each Raman observation are shown in Table 3.2. Gaussian fitting was used to estimate the peak location of each sample in the analysis of the Raman spectra modification of the *ex-situ* MgB_2 bulk samples.

Table 3.2. Results summary for bulk samples of MgB_2: Onset of critical temperature $T_{c\text{-}onset}$, the frequency of the E_{2g} mode, the electron–phonon coupling constant (EPC)

Sample	Sample Name	$T_{c\text{-}onset}$ (K)	E_{2g} (cm^{-1})	EPC
Pure *ex-situ* MgB_2 (600°C – 1 hour)	S1	38.5	570.72	1.109
Pure *ex-situ* MgB_2 (700°C – 1 hour)	S2	38.5	573.42	1.107
Pure *ex-situ* MgB_2 + 0.5 mol Mg (700°C – 1 hour)	S3	38.5	584.40	1.100
Pure *ex-situ* MgB_2 + 0.5 mol Mg (700°C – 3 hours)	S4	38.5	580.87	1.102
Pure *ex-situ* MgB_2 + 0.5 mol Mg (1000°C – 1 hour)	S5	38.1	582.08	1.094
Pure *ex-situ* MgB_2 + 30 wt.% (1.5 Mg + 2 B) (700°C – 1 hour)	S6	38.6	572.21	1.109
Pure *ex-situ* MgB_2 + 30 wt.% (1.5 Mg + 2 B) (800°C – 1 hour)	S7	38.8	567.34	1.116

3.3. Effect of sample preparation conditions on J_c of MgB_2 bulk superconductors

Samples tested at 5 K, 10 K, 15 K, 25 K, and 30 K had M–H hysteresis loops, as shown in Figure 3.4. The loops demonstrate that there is no flux leap. The wider

loops, ΔM, reflect the increase in J_c of the samples when they are fabricated under various conditions.

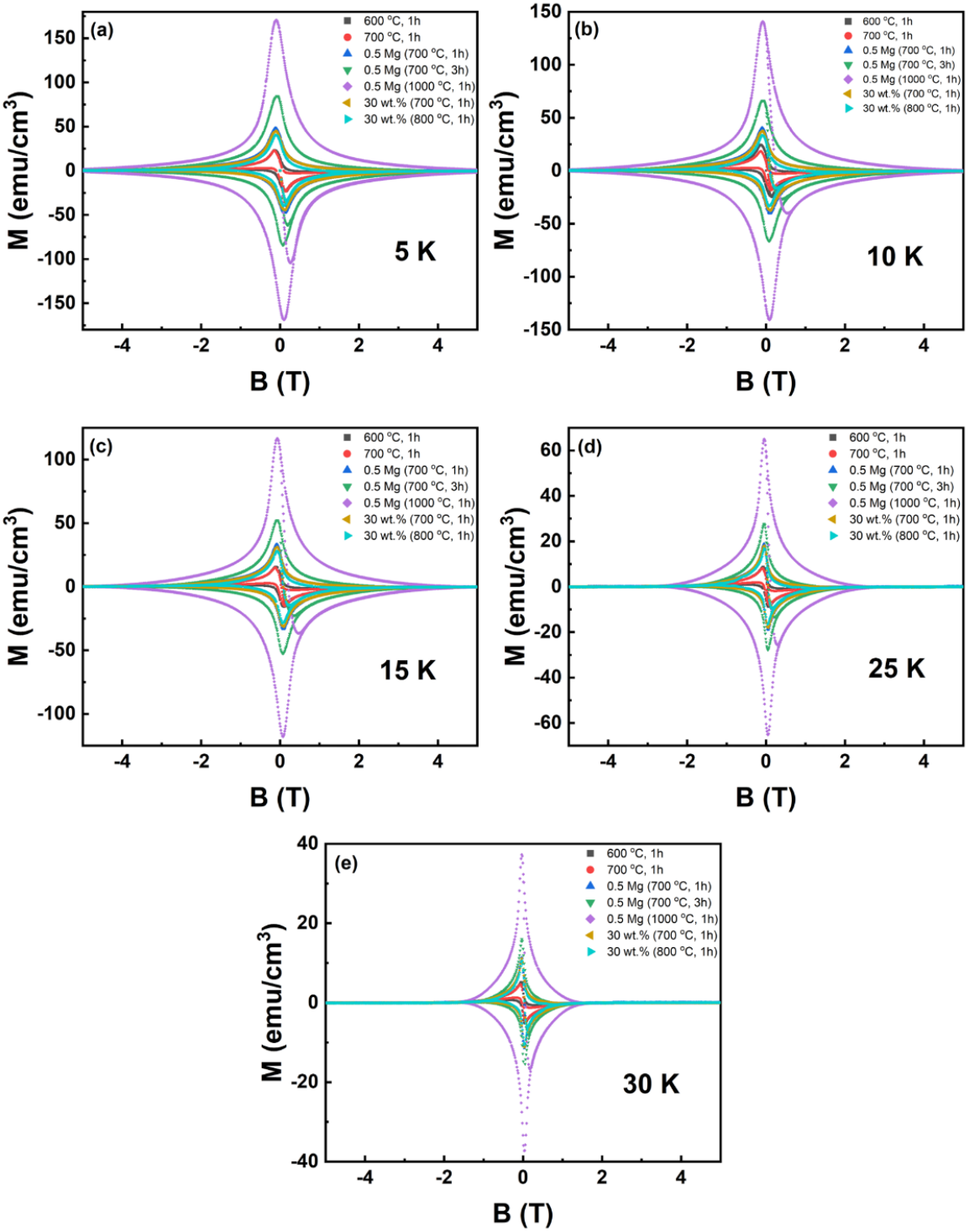

Figure 3.4. M-H hysteresis loop for ex-situ MgB_2 bulk samples fabricated at different conditions at (a) 5 K, (b) 10 K, (c) 15 K, (d) 25 K and (e) 30 K.

The following adjusted Bean's model was used to get the field-dependent J_c of each sample [17]:

$$J_c = \frac{20\Delta M}{\left[a\left(1 - \frac{a}{3b}\right)\right]}, \tag{3.2}$$

where a as well as b are perpendicular to the applied magnetic field sample dimension, and ΔM is the magnetization hysteresis width. The field dependency of J_c for MgB_2 bulk samples at temperatures of 5 K, 10 K, 15 K, 25 K, and 30 K is shown on a double-logarithmic scale in Figure 3.5 (a–e). In contrast to sample S1, sample S2's J_c value dropped as the sintering temperature rose. At all temperatures and studied fields, samples S3, S4, S5, S6, and S7 exhibit significantly higher J_c. Specifically, sample S5 showed the largest J_c improvement, whereas another MgB_2 bulk sample showed a somewhat smaller increase. Additionally, after evaluating every sample, J_c gradually lowered the applied field on these samples. In comparison to other MgB_2 bulk samples, J_c decreased to 100 A/cm^2 at a higher irreversible field. These results suggest that, with appropriate sample preparation, the inclusion of Mg as well B might be utilized as an additional pinning center, improving J_c beneath external field settings [20,47,48]. Weakened inter-grain connection might be the cause of the impairment shown in samples S2.

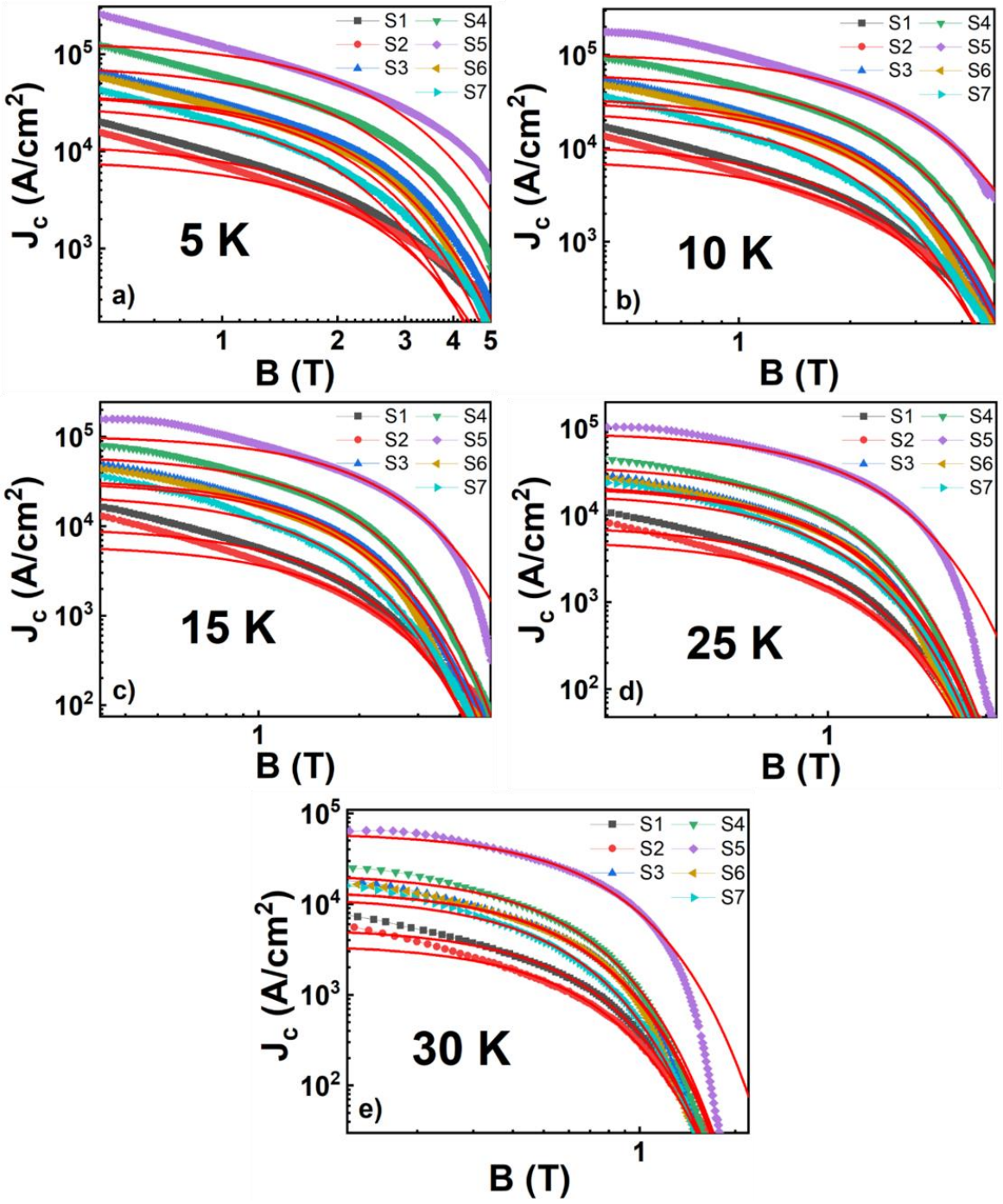

Figure 3.5. Using collective pinning theory, the field dependency of J_c for ex-situ MgB_2 bulk samples manufactured at various temperatures (a) 5 K, (b) 10 K, (c) 15 K, (d) 25 K, and (e) 30 K was described. Using Equation (3.3), solid lines represent curves that fit.

The most effective sample manufacturing for J_c augmentation was examined, along with the effects on including Mg and B. However, it is necessary to ascertain how the

addition of Mg and B affects each field regime in addition to the flux pinning process. The collective pinning hypothesis of Blatter *et al.* describes the vortex behavior of high-temperature superconductors and aids in the study of the vortex pinning process [11]. According to the hypothesis, the way that J_c is shown varies depending on the magnetic field regime. J_c in the magnetic field has been separated into three regimes by the crossover fields, such as B_{sb} and B_{lb} [11]: the single vortex regime, the small bundle regime, and the large bundle regime. The field that moves from the single vortex regime to the small bundle regime is called B_{sb}, whereas the field that moves from the small bundle regime to the large bundle regime is called B_{lb}. J_c in the field is almost flat in the single vortex regime, where each vortex is individually pinned. Flat J_c was broader in samples S3, S4, S5, S6, as well as S7, suggesting that there were more pinning centers in these samples. As the magnetic field intensity increases, the vortex density exceeds the pinning center density, resulting in collaborative pinning of the vortices [11]. The pinning process evolved from a single vortex to tiny bundle pinning. The following exponential rule adequately explains the sharp decline in field-dependent J_c in this regime [44]:

$$J_c(B) = J_c(0)exp\left[-\left(\frac{B}{B_0}\right)^{\frac{3}{2}}\right], \tag{3.3}$$

where B_0 is the normalizing parameter. The fitting curves at 5 K, 10 K, 15 K, 25 K, then 30 K are shown as solid red lines in Figure 3.5 (a–e). The dissimilarity between the lower and higher fields has been used to calculate the values of the crossover fields B_{sb} along with B_{lb}, respectively, based on the findings of fitting the tiny bundle regime. The estimate process employed $-\log[J_c(B)/J_c(0)]$ as a function of B in a double-logarithmic plot, as stated by Ghorbani *et al.* [38]. Table 3.3 displays the B_{sb} along with B_{lb} values. In samples S1, S2, S3, S4, as well S5, B_{sb} and B_{lb} increased, whereas in samples S6 and S7, they decreased. At lower temperatures, B_{sb} and B_{lb} increased significantly. For sample S5, the B_{sb} value at 5 K was only 0.057 T and 0.008 T, which was higher than that of samples S3 and S4, respectively, whereas at 10 K, the B_{sb} value reached 0.261 T with 0.249 T higher, while at 15 K, it was 0.356

T with 0.303 T higher. Comparing sample S5 to samples S3 and S4, the B_{lb} value is likewise 0.105 T and 0.088 T more at 5 K, 0.639 T along with 0.588 T greater at 10 K, and 0.923 T along with 0.465 T greater at 15 K. Sample S5 had the greatest B_{sb} and B_{lb} values when compared to the other samples at all temperatures, ranging from 5 K to 30 K. The B_{sb} increase in samples S1, S2, S3, S4, as well as S5 showed that the single vortex had enlarged, which is linked to the rise in the number of pinning centers. Furthermore, these samples' B_{lb} rise showed that the supplemental pinning center operated efficiently under the collective pinning regime. The inclusion of Mg and B, together with the best sample preparation, which is linked to the enhancement of J_c at a high external magnetic field, widened the regime of small and big bundles. A vortex might have been independently pinned by a pinning center in the single vortex regime, when the magnetic field is less than B_{sb} [26]. Therefore, the appearance of additional flaws and impurities as additional pinning centers was probably proof of the enlargement of the single vortex regime. These fabricated pinning centers showed a significant collective pinning potential by extending the tiny bundle regime.

Table 3.3. Bulk samples of MgB_2 at 5, 10, 15, 25, and 30 K were measured for B_{sb} and B_{lb} values.

Sample	**5 K**		**10 K**		**15 K**		**25 K**		**30 K**	
	B_{sb} (T)	B_{lb} (T)	B_{sb} (T)	B_{lb} (T)	B_{sb} (T)	B_{lb} (T)	B_{sb} (T)	B_{lb} (T)	B_{sb} (T)	B_{lb} (T)
S1	0.996	3.380	0.848	3.083	0.801	3.069	0.458	2.099	0.267	1.164
S2	1.152	3.474	0.978	2.977	0.952	3.092	0.475	1.924	0.288	1.131
S3	1.182	3.725	0.997	3.952	0.804	3.205	0.481	1.974	0.296	1.131
S4	1.231	3.742	1.009	4.003	0.857	3.663	0.490	2.124	0.304	1.208

S5	1.239	3.830	1.258	4.591	1.160	4.128	0.525	2.369	0.336	1.310
S6	1.026	3.521	0.981	3.652	0.781	3.102	0.443	1.791	0.297	1.086
S7	0.657	2.684	0.632	2.295	0.514	2.107	0.332	1.236	0.212	0.792

It was found that the J_c value of the MgB_2 bulk samples rose the greatest when they were manufactured in the *ex-situ* condition of Pure *ex-situ* MgB_2 + 0.5 mol Mg sintered at 1000 °C for one hour. In particular, when the field was set to 0.1 T, the J_c value reached around 1.2×10^5 A/cm^2, which is almost 5 times greater than the J_c value of the samples used in prior research, which was approximately 2.4×10^4 A/cm^2. The J_c of this sample was about 3.2 times greater than the field of 0.5 T, approximately 2.3 times higher at the field of 1 T, approximately 1.3 times higher at the field of 1.5 T, and approximately 1.2 times higher at the field of 2 T when compared to the J_c of prior research. The specific comparison results are shown in Table 3.4 below.

Table 3.4. Comparison of J_c values of sample S5 with other samples in previous studies

Samples	J_c (A/cm^2) at 25 K					Ref.
	0.1 T	0.5 T	1 T	1.5 T	2 T	
Pure *ex-situ* MgB_2 + 0.5 mol Mg (1000 °C – 1h) (S5)	1.2×10^5	7.0×10^4	4.0×10^4	1.6×10^4	0.8×10^4	This work
MgB_2 sample annealed at 700 °C for 15 min at pressures 1 GPa	2.4×10^4	2.2×10^4	1.7×10^4	1.2×10^4	0.7×10^4	[24]
MgB_2 samples with 10 wt % silicone-oil addition annealed at 600 °C	8.9×10^4	3.6×10^4	0.7×10^4	1.1×10^2	0.6×10^2	[27]

3.4. Effect of sample preparation conditions on flux pinning mechanism of MgB_2 bulk superconductors

The significant increase in J_c necessitates an investigation of the flux pinning process by incorporating Mg as well B on the MgB_2 bulk superconductor. In type-II superconductors, the primary effective vortex-pinning center contact is the core interaction [53]. Additionally, the kind of core contact has two main pinning processes, which include δl pinning and δT_c pinning. In the single-vortex pinning regime, Griessen *et al.* established the following guidelines for every pinning mechanism [31]:

For δl pinning:

$$J_{sv}(t)/J_c(0) = (1-t^2)^{\frac{5}{2}}(1+t^2)^{-\frac{1}{2}}, \quad (3.4)$$

For δT_c pinning:

$$J_{sv}(t)/J_c(0) = (1-t^2)^{\frac{7}{6}}(1+t^2)^{\frac{5}{6}}, \quad (3.5)$$

At 0.01 T, J_{sv} has been chosen as J_c based on the prior regime division [53]. The normalized critical current density, $j = J_c(\mathrm{T})/J_c(0)$, is shown against the normalized temperature, $t=T/T_c$, for all *ex-situ* MgB_2 bulk samples in Figure 3.6 (a). The Ginzburg–Landau coefficient (κ) differential resulting from oscillations in the critical temperature (T_c) is linked to the ascending pinning mechanism, δT_c, for the entire set of MgB_2 samples [53,70]. Previous studies on MgB_2 superconductors are in agreement with this finding. The relationship between B_{sb} and the critical current density in the context of collective pinning theory is as follows: $B_{sb} \sim j_{sv}B_{c2}$. The formula for the normalized temperature dependency of B_{sb} was derived by Qin *et al.* [70]:

For δl pinning:

$$B_{sb}(t)/B_{sb}(0) = [(1-t^2)/(1+t^2)]^{\frac{2}{3}}, \quad (3.6)$$

For δT_c pinning:

$$B_{sb}(t)/B_{sb}(0) = [(1-t^2)/(1+t^2)]^2, \quad (3.7)$$

These formulae were used to determine the normalized small bundle field b_{sb} *(=* $B_{sb}(t)/B_{sb}(0)$*)* values of samples at 5, 10, 15, 25, as well 30 K. The results are displayed in Figure 3.6 (b). The B_{sb} data is in agreement with the δT_c pinning expression. Consistent with the earlier *j-t* and b_{sb}-*t* studies, the results confirmed the dominance of the δT_c pinning mechanism in all MgB_2 bulk superconductors at different temperatures. The natural pinning center, which is identified by the grain boundaries of pure materials, is suitable for δT_c pinning. The production of defects, distortions, impurities, as well as dislocations as revealed by SEM, XRD, and MT studies is linked to δT_c pinning, according to Hapipi *et al.* [34,58]. Figure 3.6 (b) shows a minor shift from δT_c to δl pinning with the inclusion of Mg and B.

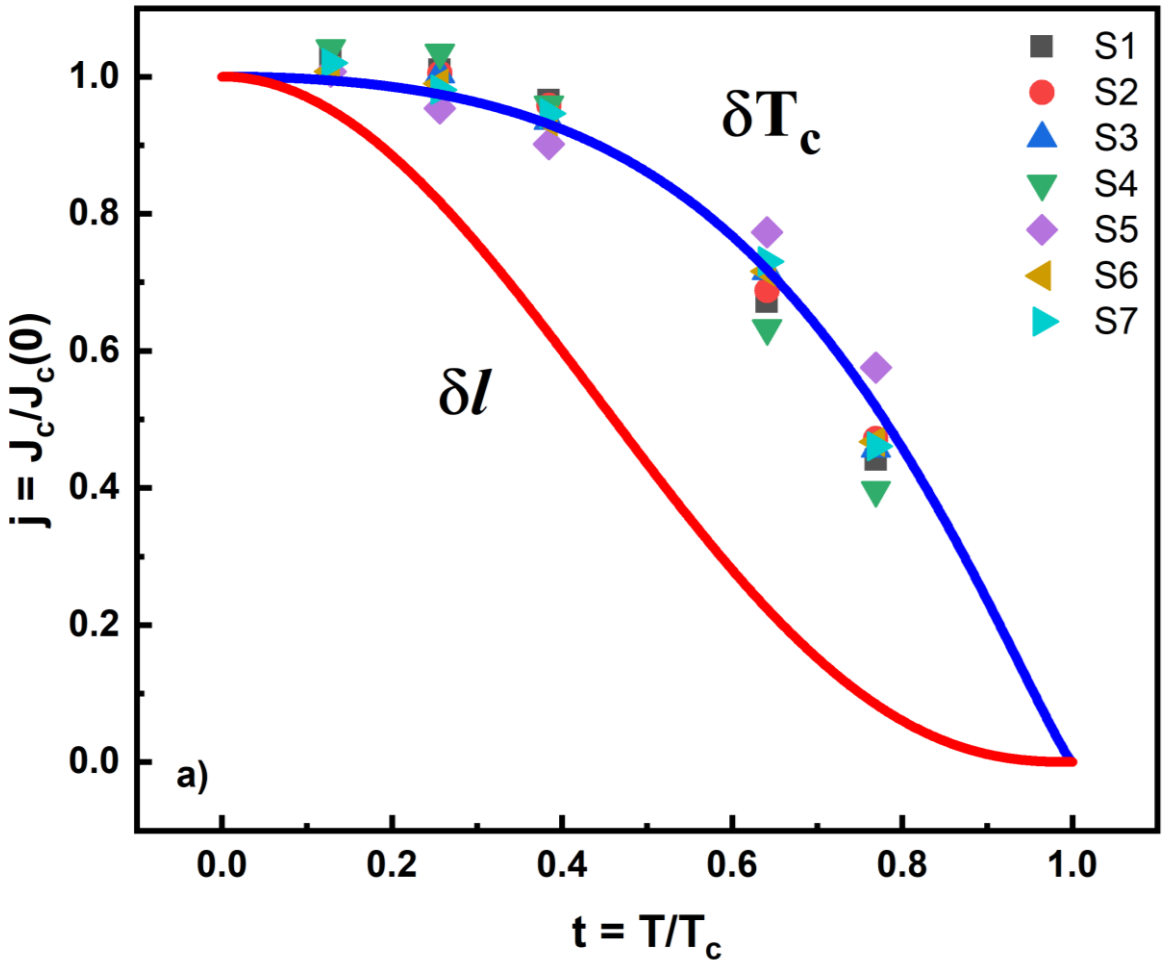

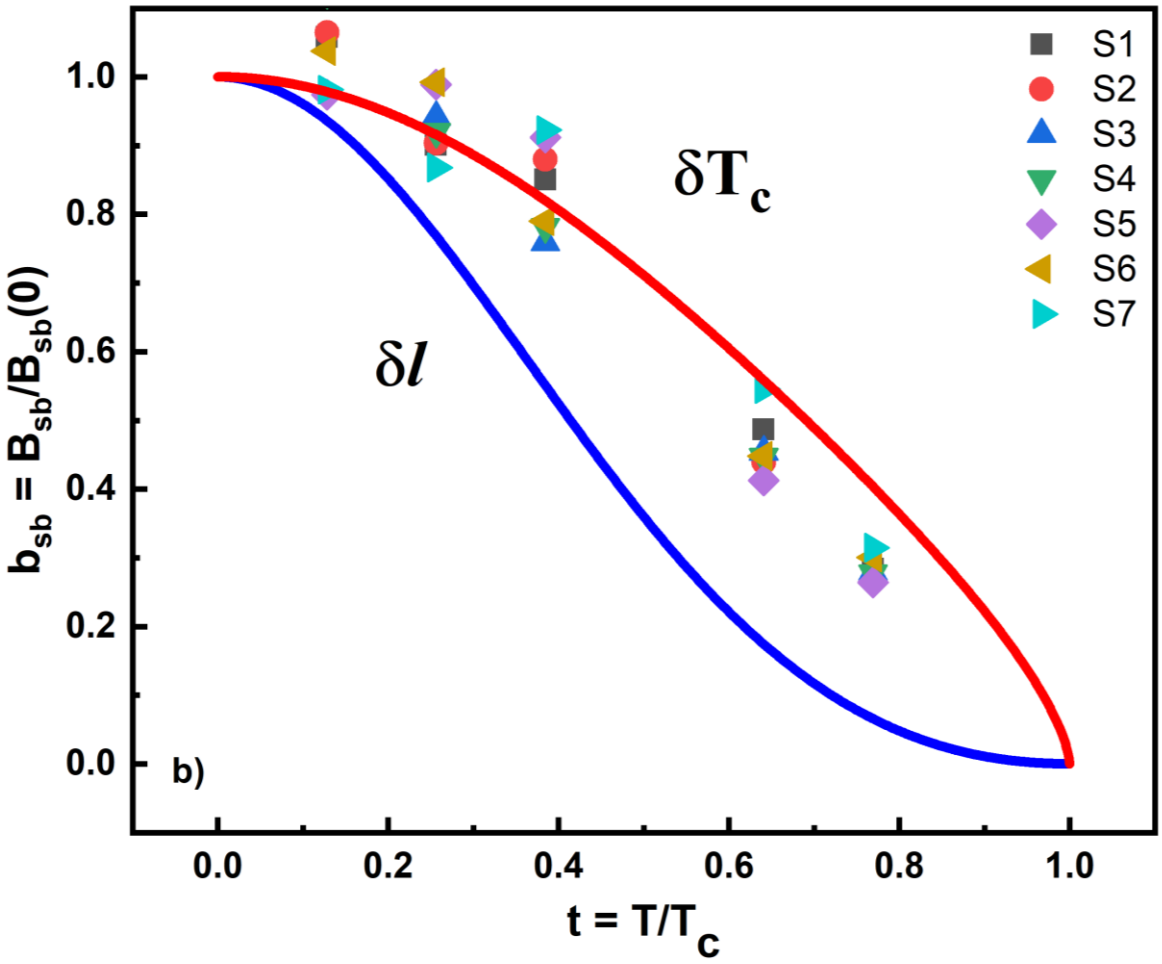

Figure 3.6. (a) Normalized J_c and (b) normalized B_{sb} for each sample's normalized temperature dependence. Using Eqs. (3.4) and (3.5), solid lines are curves that fit the δl and δT_c pinning mechanisms.

3.5. Effect of sample preparation conditions on geometry of pinning centers in MgB_2 bulk superconductors

The enhancements of J_c in type-II superconductors have been attributed to the improved flux – pinning properties in these materials [16,26,27,47]. We assessed the magnetic field dependency of F_p in MgB_2 bulk samples under various sample preparation circumstances in order to fully comprehend the effects of including Mg as well as B on the properties of flux pinning in MgB_2 bulk samples. The formula $F_p = B \times J_c$ was used to obtain the F_p values from the $J_c(B)$ data. Figure 3.7 displays the reduced flux pinning force density ($f_p = F_p/F_{p,max}$) as a function of the reduced magnetic field ($b = B/B_{irr}$), where a criteria of J_c = 100 A/cm^2 at 5 K was used to

define B_{irr}. In addition to increased strength, the most pertinent research on F_p-b revealed the dominant pinning centers on MgB_2 bulk samples, which call for more study utilizing the Dew–Hughes model [16,50]. The following function has been used to apply the Dew–Hughes model in order to examine the properties of the extra flux pinning centers [16]:

$$f_p = Ab^p(1-b)^q, \tag{3.8}$$

where the normalized flux pinning force density is $f_p = F_p/F_{p,max}$, whereas the fitting parameters are A, p, along with q. Using the Dew–Hughes model fitting line, Figure 3.7 shows f_p as a function of b throughout all *ex-situ* MgB_2 bulk samples. An novel pinning function for grain boundary (surface) pinning was implemented to match the data points, with fixed values of p = 0.5 and q = 2 (red line). Every sample's fitting parameters are similar for every temperature that was looked at. Sample q values are typically around 2, which corresponds to the core interaction, at all temperatures [26]. As a result, we could use the overall p or b_{peak} values from all the samples to examine the predominant kind of pinning centers in the data. The normal core surface pinning center (p = 0.5) was linked to the non-added sample's b_{peak} value and average values of p, which were 0.211 and 0.562, respectively [16]. The grain boundary pinning, which has been identified as the typical core surface pinning center, is the natural pinning center of the *ex-situ* MgB_2 bulk superconductor [46]. As previously examined by SEM images, the extra Mg as well B, together with variations in temperature and sintering time, resulted in improved grain coupling aided by the *in-situ* synthesis of MgB_2, which filled the gaps and joined the MgB_2 grains. Solid-state self-sintering occurred as the sintering temperature rose, strengthening the core surface pinning even further. This result was in line with the findings of the earlier j-t and b_{sb}-t analysis. This phenomena is linked to misoriented grain boundaries, voids, or porosity, as well as the porosity intension identified by SEM and XRD investigations in our earlier work [34].

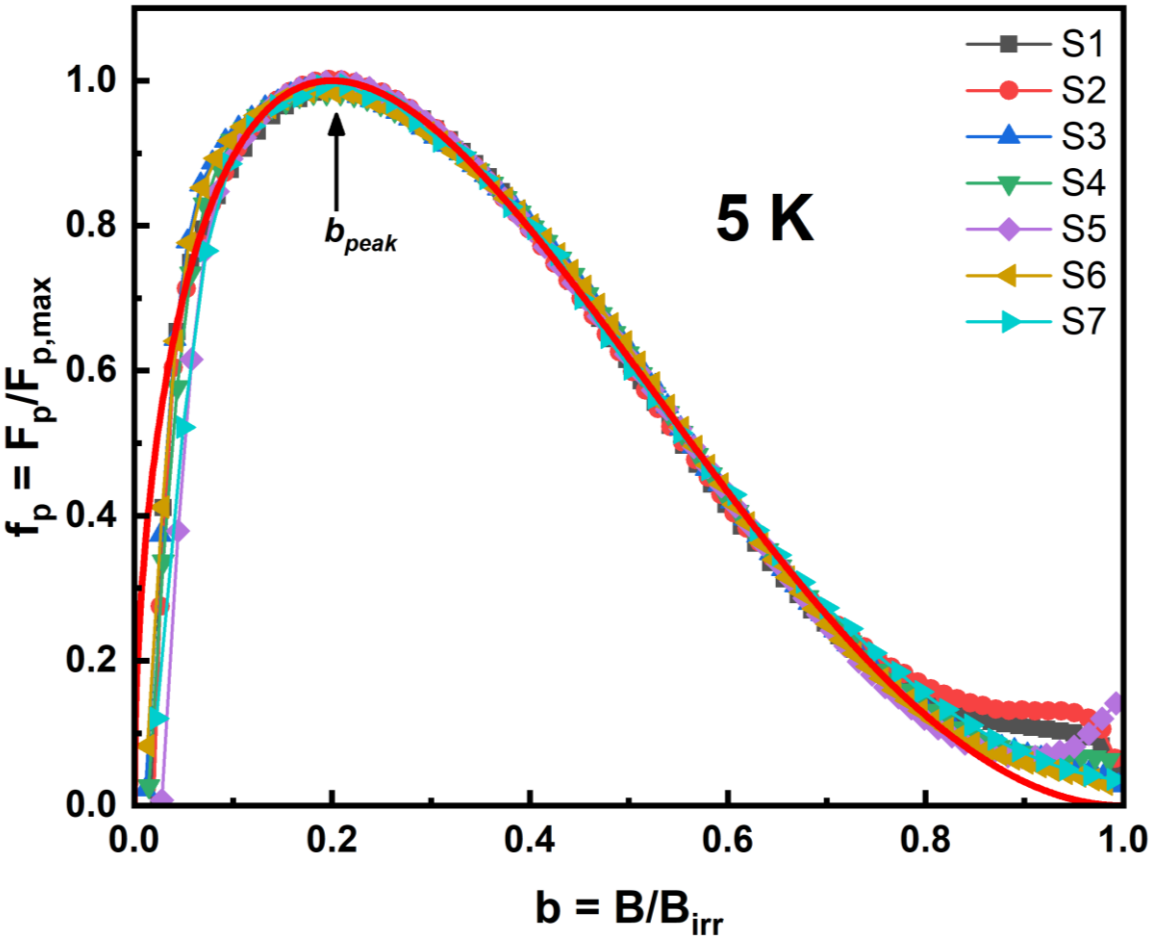

Figure 3.7. All samples' normalized field dependency at 5 K using a modified Dew-Hughes model scaling. Fitting curves using Equation (3.8) are represented by solid lines.

Conclusion of Chapter 3

The *ex-situ* MgB_2 bulk samples generated under different circumstances were examined for their local structure along with superconducting characteristics. We spoke about the superconducting and electron-phonon (e-ph) properties of bulk MgB_2 samples, including T_c, J_c, and F_p. T_c stays constant for samples S1–S3, decreases for samples S5, and rises for samples S6–S7, according to the temperature-dependent magnetization data, M(T). In order to explain the reported T_c, this dissertation discovered a significant correlation between the frequency of the E_{2g} mode and T_c. The shift in E_{2g} values matched the shift in T_c values. The link between EPC, E_{2g}, as well as T_c determined by the McMillan equation may support this conclusion.

Furthermore, the performance of superconducting transitions is significantly influenced by the EPC constant, which is ascertained by Raman spectroscopy. Our results suggest that variations in the EPC impact disordered strength-induced MgB_2 superconductivity, which can promote Cooper pair localization. After Mg and B were added, the samples' J_c(B) rose. Samples S3–S7 were the ones where the fabrication circumstances were altered the most, and sample S5 – Pure *ex-situ* MgB_2 + 0.5 Mg (1000 °C – 1 hour) – showed the biggest rise in J_c. According to pinning theory, J_c is suitably outfitted in tiny bundle mode. For every samples, the B_{sb} as well as B_{lb} values have been estimated between 5 and 30 K. The results show that the small and huge bundle modes expand with the incorporation of Mg as well B and with varying sintering conditions. In all *ex-situ* MgB_2 bulk samples, δT_c pinning was the most prevalent pinning mechanism, according to $j(t)$ and $b_{sb}(t)$ studies. In order to comprehend the function of Mg as well B addition in the flux pinning process, the normalized field dependency of f_p was investigated using the Dew–Hughes model. The additional centers are normal core surface pinning centers in all samples, according to the fitting parameters p and q. High-quality *ex-situ* MgB_2 bulk samples may thus be produced by optimizing the appropriate fabrication circumstances using the data obtained. In order to produce high-quality *ex-situ* MgB_2 bulk samples, the data obtained may therefore aid in releasing the appropriate fabrication conditions.

Chapter 4: ENHANCEMENTS OF CRITICAL CURRENT DENSITY OF MgB_2 BULK SUPERCONDUCTORS WITH CO-ADDITIONS OF B_4C AND Dy_2O_3

After optimizing the fabrication of MgB_2 bulk superconductors showing the high value of J_c, the further enhancements of J_c in MgB_2 bulk superconductors will be carried out. In addition to grain coupling, improving J_c requires the addition of rare earth oxides (ReO) [86] and carbon (C) [75] to create efficient flux pinning centers. Boron carbide (B_4C) has some benefits in this respect. It can be utilized as a precursor to react with magnesium instead of boron, forming C-doped MgB_2 with high field-dependent J_c [75]. However, because *ex-situ* MgB_2 has a high thermal stability, C substitution by B_4C addition can be difficult [78]. Another possible dopant to raise J_c is ReO materials [57]. This is particularly true for Dy_2O_3, which has been demonstrated to significantly increase J_c [86]. The creation of nano-scale DyB_4 after the interaction of Dy_2O_3 with B is thought to improve flux pinning in the samples [86]. For the *in-situ* reaction of Mg and B, it has also been reported that the co-addition of B_4C and Dy_2O_3 enhanced J_c (20 K) to 10^5 A×cm^{-2} at approximately 3 T [57]. Motivated by the two successes, this dissertation intend to use both B_4C and Dy_2O_3 to increase the J_c of *ex-situ* MgB_2 bulk superconductors. Additionally, magnesium powder was added to the samples to enhance the grain connection. Crystal structure, phase development, along with grain form were analyzed in connection with the samples' superconducting properties.

In this chapter, B_4C along with Dy_2O_3 were added to create MgB_2 bulk superconductors. The predominance of MgB_2 in each sample was verified by X-ray diffraction. Temperature-dependent resistivity as well as magnetization measurements in the in-field were used to assess the samples' superconducting characteristics. Each sample's B_{c2} and J_c were estimated. The findings show that the ideal addition levels of B_4C along with Dy_2O_3 result in notable improvements in B_{c2} and J_c. In the manufactured samples, δl pinning was shown to be the predominant pinning type based on collective pinning theory. Grain boundary-induced core surface

pinning was shown to be the predominant pinning mechanism, which is in line with the Dew–Hughes model estimates.

Along with the previously indicated addition of magnesium, trace quantities of B_4C along with Dy_2O_3 were also added. After fixing Dy_2O_3 at 2 weight percent, B_4C was added at 5 and 10 weight percent concentrations. This work set out to investigate how the coaddition of Mg, B_4C, as well Dy_2O_3 affected the crystal structure as well as superconducting characteristics of MgB_2. Collective pinning theory served as the foundation for the analysis of the pinning mechanism. The main interactions between pinning centers and vortices in type II superconductors are core and magnetic interactions. Localized distortions in superconducting characteristics coupled with periodic variations in the superconducting order parameter generate core interactions. This phenomena is especially important for high κ-valued type II superconductors. Core pinning is linked to random spatial changes in the transition temperature (δT_c pinning) in MgB_2 bulk superconductors, when κ is more than 20. In contrast, core interactions in high-temperature superconductors are mostly associated with variations in the charge-carrier mean free path (δl pinning), which are primarily brought on by crystal lattice defects. Additionally, a modified Dew–Hughes model for the flux pinning force density was used to identify the kind of pinning. The coexistence of δl and δT_c pinning was shown to be the primary pinning mechanism in MgB_2 bulk superconductors with the coaddition of Mg, B_4C, as well Dy_2O_3 when theoretical models were used. Two-dimensional surface pinning was then determined by analyzing the geometry of the pinning centers. Grain connection was probably increased by the coaddition of B_4C along with Dy_2O_3, which in turn improved B_{c2} and J_c [58,63]. Table 4.1 contains a list of the samples' names and information.

Table 4.1. Details of MgB_2 bulk superconductors with co-additions of B_4C and Dy_2O_3 samples names and fabrication conditions

No.	Sample	Sample Name
1	Pure MgB_2	Pure MgB_2
2	MgB_2 + 0.5 mol Mg	S5-1
3	MgB_2 + 0.5 mol Mg + 5wt.% B_4C	S5-2
4	MgB_2 + 0.5 mol Mg + 5wt.% B_4C + 0.5wt.% Dy_2O_3	S5-3
5	MgB_2 + 0.5 mol Mg + 5wt.% B_4C + 1.0wt.% Dy_2O_3	S5-4
6	MgB_2 + 0.5 mol Mg + 5wt.% B_4C + 2.0wt.% Dy_2O_3	S5-5
7	MgB_2 + 0.5 mol Mg + 10wt.% B_4C + 1.0wt.% Dy_2O_3	S5-6

4.1. Crystal structure of MgB_2 bulk superconductors with co-additions of B_4C and Dy_2O_3

Figure 4.1 (a) displays the XRD patterns of the bulk MgB_2 samples with 0.5 mol of additional Mg and with different B_4C along with Dy_2O_3 concentrations. In all samples, the MgB_2 phase, which features a hexagonal crystal structure and serves as a component of the P6/mmm space group, is mostly represented by the diffraction peaks. This is in agreement with the ICSD reference (98-009-2831). The strongest peaks connected to the (101) plane have been observed at around $2\theta \approx 42.5°$. Furthermore, peaks that corresponded to MgO (ICSD: 98-009-4096) were seen in all samples at around $2\theta \approx 62.1°$. MgO is most likely present because oxygen was added to the sample during sample preparation, most likely during pelletization, grinding, or closing the stainless steel tubes before heat treatment. During these activities,

highly reactive magnesium may have formed MgO as a result of this partial exposure to air [59]. While the simultaneous addition of B_4C along with Dy_2O_3 raised the intensities of the MgB_2 as well as MgO peaks, the addition of B_4C lowered them [59]. Prior research has shown that Dy_2O_3 combines with B and Mg to produce DyB_4 [18], but no discernible DyB_4 peaks were seen in our investigation. This absence might be explained by the MgB_2 that was generated prior to the chemicals being mixed in this experiment, which inhibited the production of DyB_4. Figure 4.1 (b) displays the estimated lattice characteristics of the manufactured samples. It shows that when B_4C along with Dy_2O_3 were codoped at different weight percentages, there was no discernible change in the *a*- or *c*-lattice properties.

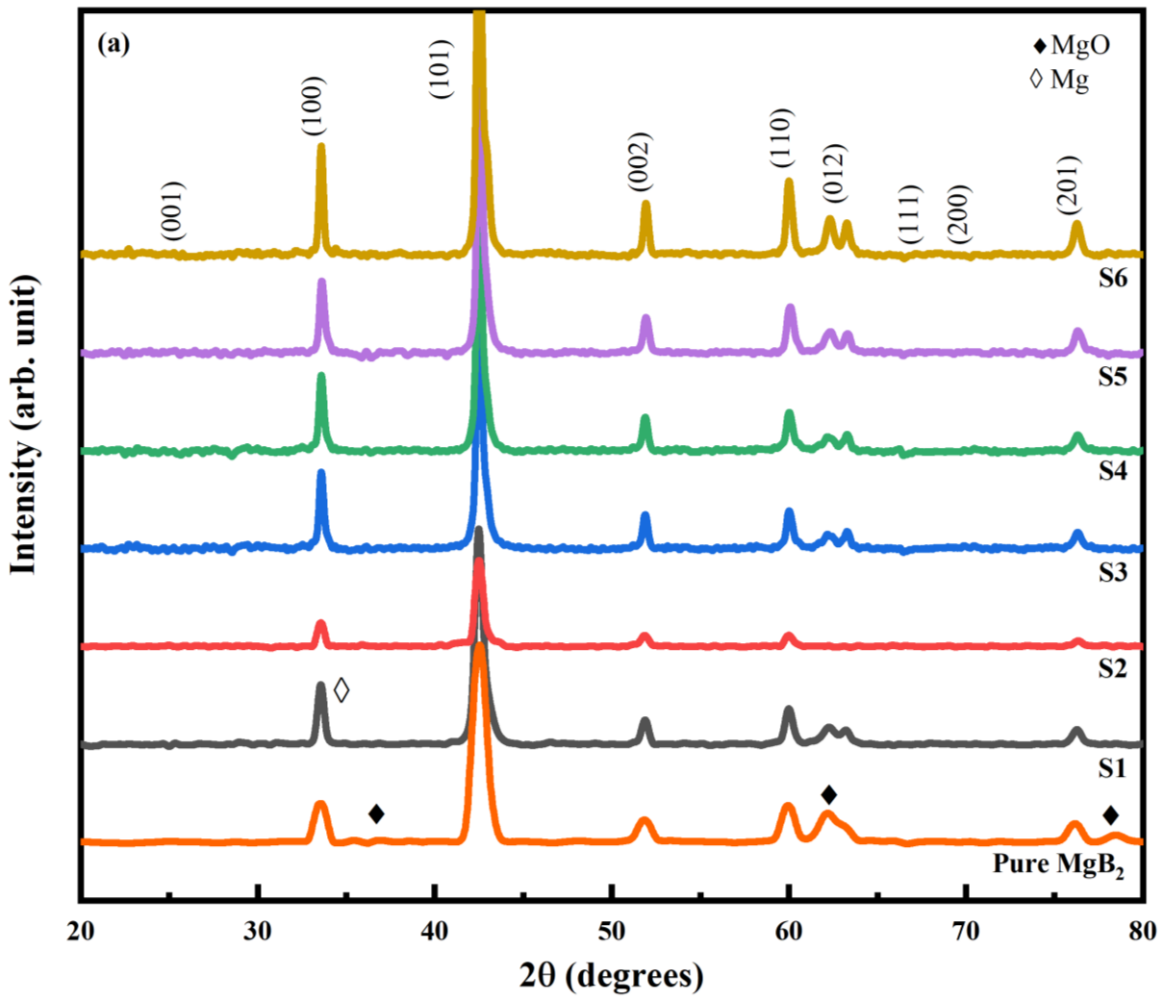

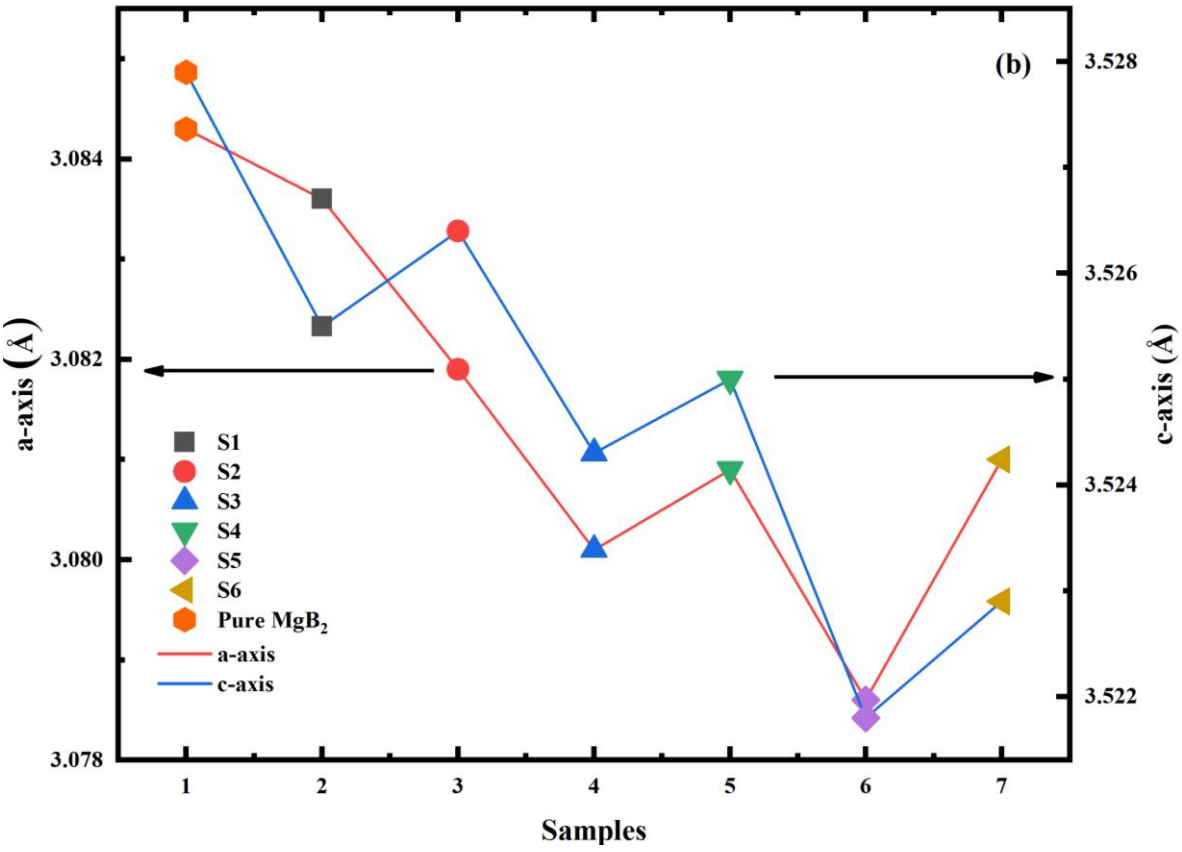

Figure 4.1. (a) XRD patterns and (b) a-axis as well as c-axis values of MgB_2 bulk samples.

4.2. Effect of co-additions of B_4C and Dy_2O_3 on T_c of MgB_2 bulk superconductors

After examining the crystal structure of MgB_2 bulks with co-additions of B_4C and Dy_2O_3, the variations of T_c and B_{c2} of these samples are going to investigate. In this chapter, resistivity versus temperature ($\rho(T)$) measurements were used to infer the superconducting transition as well as T_c values. Plots of normalized resistivity vs temperature, $\rho(T)/\rho(T = 41\ K)$, are shown in Figure 4.2 (a) for all samples in the 33–45 K range without an applied field. The temperature that occurred when $\rho(T)/\rho(T = 41\ K)$ equaled zero was determined to be the critical temperature (T_c) of the manufactured samples. The following was the main focus of the two observations: As the coaddition content increased, (i) the T_c dropped and (ii) the transition breadth widened. Table 4.2 contains a list of the T_c values. Sample S5-1 had a T_c of 38.57 K

[74], whereas sample S5-4 had the lowest T_c of 34.70 K. With the incorporation of B_4C along with Dy_2O_3, the transition width broadens, indicating a reduction in the samples' homogeneity and crystallinity [49,64].

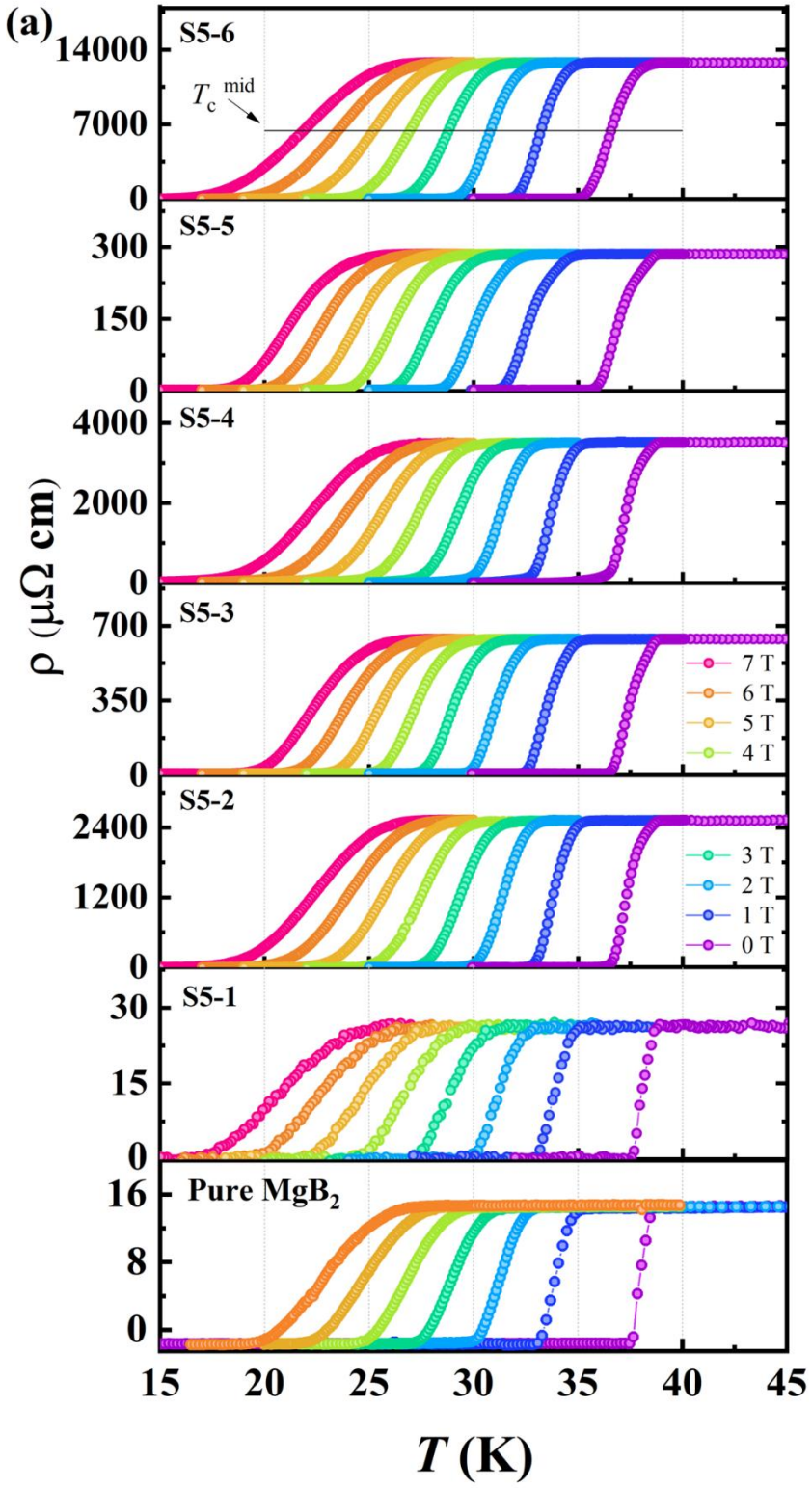

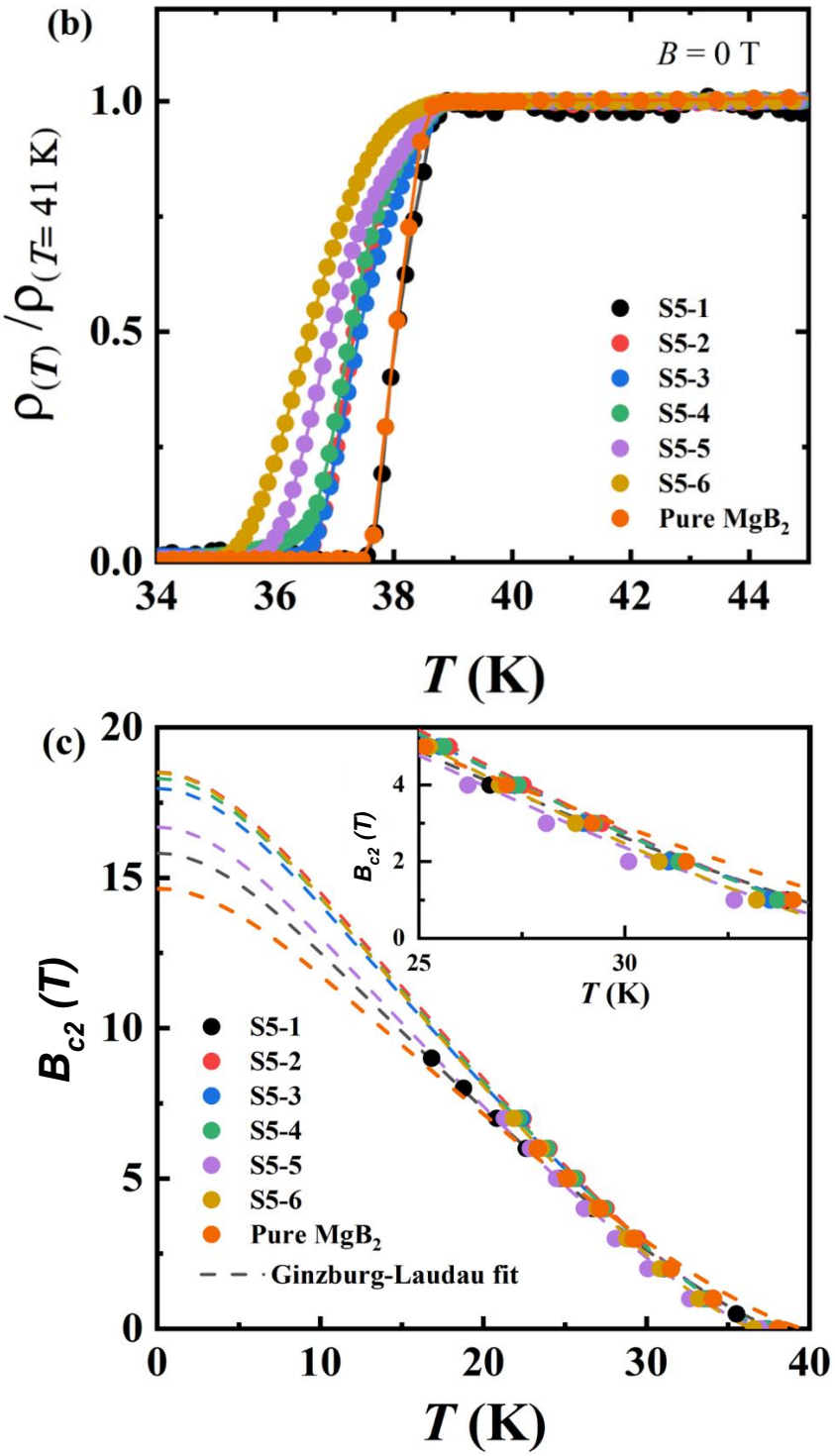

Figure 4.2. (a) Resistivity (ρ) as a function of temperature for MgB_2 bulk samples with the applied fields ranged from 0 T to 7 T; (b) normalized ρ(T)/ρ(41K), and (c) B_{c2} as a function of temperature for MgB_2 bulk samples.

4.3. Effect of co-additions of B_4C and Dy_2O_3 on B_{c2} of MgB_2 bulk superconductors

The effects of B_4C along with Dy_2O_3 on the upper critical field (B_{c2}) of the MgB_2 bulk samples were examined in addition to T_c. Under different magnetic fields, the electrical resistivity has been measured as a function of temperature. Figure 4.2 (b) displays the in-field resistivity vs temperature curve with the applied field scanned from 0 to 7 T. As the intensity of the magnetic field rises, the superconducting transition width grows monotonically. The 50% resistivity criteria during the superconducting transition was used to determine the value of B_{c2}. With the exception of sample S5-2, whose maximum value was 18.51 T, all of the doped samples had B_{c2} values larger than the sample S5-1, which had a value of 15.82 T. Five weight percent B_4C was the best dopant for raising B_{c2}. Figure 4.2 (c) displays the temperature dependence of B_{c2} for each sample. It demonstrates that all graphs follow a positive curvature close to T_c, which is explained by MgB_2's two-band superconductivity [33]. The B_{c2} (T) curves were described using two-band Ginzburg–Landau theory [5]:

$$B_{c2} = \frac{\theta^{1+\alpha}}{(1-(1+\alpha)\omega + l\omega^2 + m\omega^3)}, \tag{4.1}$$

where $\omega = (1-\theta)\theta^{1+\alpha}$, and $\theta = \left(1 - \frac{T}{T_c}\right)$. Simple expressions α, l, and m were found by experimentation [5]. The best fits were obtained with m = -1, l = 3, and α = 0.23. In Figure 4.2 (c), the fitting curves are displayed. The samples codoped using B_4C along with Dy_2O_3 had higher B_{c2}(T) values than S5-1. To illustrate the rise in B_{c2}(T), an extended region at roughly T = 30 K is shown in the inset of Figure 4.2 (c). The B_{c2}(0) value for sample S5-1 was calculated to be 15.82 T by projecting the B_{c2}(T) curves to T = 0 K. For sample S5-2, this value reached a high of 18.51 T. The coaddition of B_4C along with Dy_2O_3 may be responsible for this rise in B_{c2}, since it causes lattice deformation and probably increases impurity scattering. Consequently,

the samples' coherence length and the mean free path of the charge carriers were decreased, which raised B_{c2} [5,13,102].

In earlier research, the B_{c2} value of MgB_2 bulk samples doped with nanosized SiC was about 10.9 T [24], the B_{c2} value of MgB_2 bulk samples doped with carbon nanotube was approximately 11.5 T [117], and the B_{c2} of MgB_2 bulk samples codoped with B_4C along with Dy_2O_3 was all greater than 15 T. In particular, the B_{c2} value of sample MgB_2 + 0.5 mol Mg + 5wt.% B_4C (S5-2) is 18.51 T, which is around 1.6–1.7 times more than the doped samples in earlier investigations.

4.4. Effect of co-additions of B_4C and Dy_2O_3 on the improvement of J_c of MgB_2 bulk superconductors

The M–H hysteresis loops for the samples tested at 10 K, 15 K, 25 K, and 30 K are displayed in Figure 4.3. When they are created under different conditions, the bigger loops, or greater values of ΔM, indicate the rise in J_c.

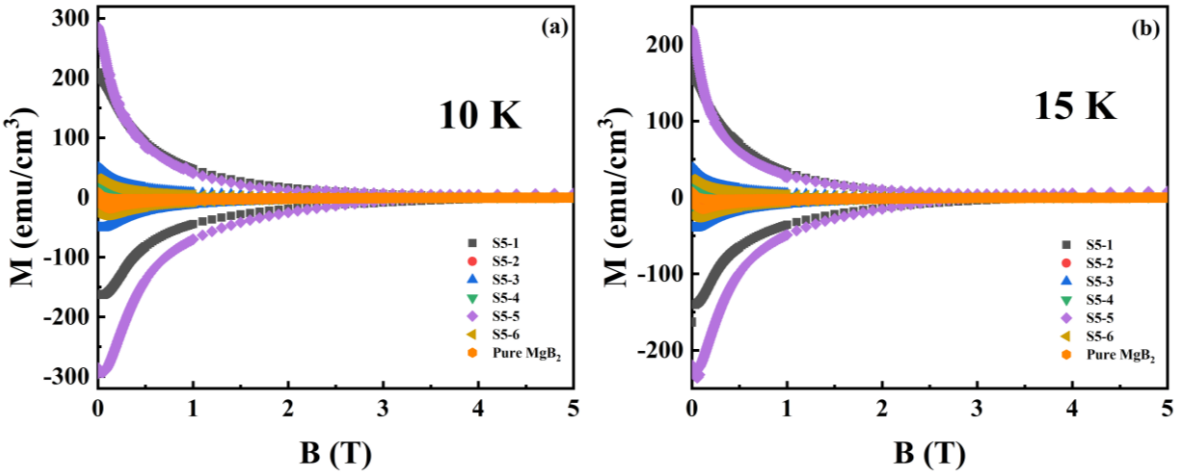

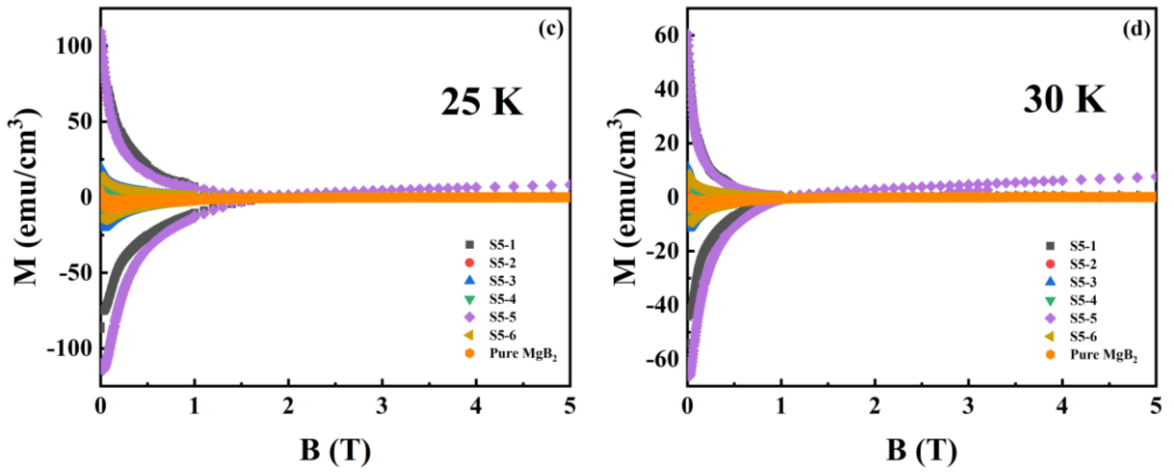

Figure 4.3. M-H hysteresis loop for MgB_2 bulk samples at (a) 10 K, (b) 15 K, (c) 25 K and (d) 30 K.

At T = 10 K, the samples' magnetization's field dependency was measured. The J_c of each sample was calculated from the magnetization hysteresis loops using the modified Bean's model as follows [17]:

$$J_c = \frac{20\Delta M}{\left[a\left(1-\frac{a}{3b}\right)\right]}, \tag{4.2}$$

where ΔM is the magnetization hysteresis breadth and a as well b as are the sample dimensions perpendicular to the applied magnetic field. The magnetic field dependency of J_c for the MgB_2 bulk samples at 10, 15, 25, and 30 K is displayed on a double-logarithmic scale in Figure 4.4 (a)–(d). At 10 K, the self-field J_c of the pure MgB_2 bulk sample was around 19 kA/cm². When Mg was added (sample S5-1) the self-field J_c was higher than when MgB_2 was pure. At all temperatures, S5's self-field J_c values rose while those of the other samples fell. Under magnetic fields, samples S5-3, S5-4, and S5-6 showed better J_c values that matched sample S5-1's curve. The inclusion of pinning centers, which probably raises the in-field Jc, may be the cause of these outcomes [13,39].

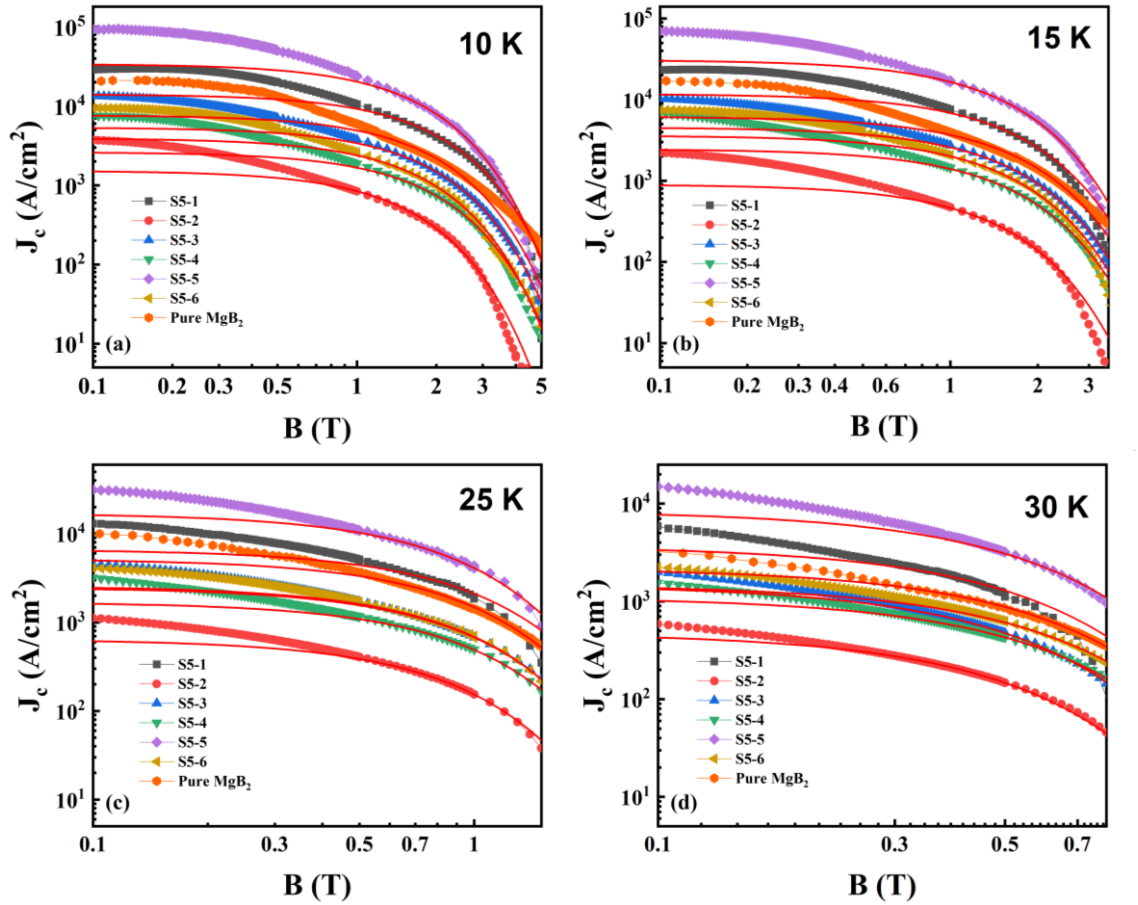

Figure 4.4. Field dependency of MgB_2 bulk samples on J_c (a) at 10 K, (b) 15 K, (c) 25 K and (d) 30 K.

The J_c value is further improved by the coaddition with a ratio of 5 wt.% B_4C + 2.0 wt.% Dy_2O_3, which is based on the manufacturing conditions described above. When compared to the doped samples that were used in earlier research, the J_c value of this sample increases by approximately 1.5-3.2 times when it is subjected to a field in the range of 0.1 to 2 T at 10 K. The specific comparison results are shown in Table 4.2 below.

Table 4.2. Comparison of J_c values of sample S5-5 with other samples in previous studies

Samples	J_c (A/cm^2) at 10 K					Ref.
	0.1 T	0.5 T	1 T	1.5 T	2 T	
MgB_2 + 0.5 mol Mg + 5wt.% B_4C + 2.0wt.% Dy_2O_3	1.0 ×10^5	5.5 ×10^4	3.0 ×10^4	1.0 ×10^4	0.9 ×10^4	This work
SiC doped MgB_2	4.6 ×10^4	2.2 ×10^4	1.3 ×10^4	0.8 ×10^4	0.6 ×10^4	[23]

By carefully examining the impacts of additives across various field regimes and the related flux pinning processes, the increase in J_c was calculated. In high-temperature superconductors, in which pinning is caused by uncorrelated disorder, the collective pinning theory has demonstrated efficacy in both elucidating vortex behavior and examining vortex pinning processes [11,73]. According to this idea, the intensity of the magnetic field affects J_c in several ways. In the J_c-B figure, J_c stays constant when the magnetic field is below B_{sb}, which is the point at which a single vortex gives way to a tiny vortex bundle pinning regime. Nevertheless, in-field J_c(B) shows exponential behavior when B exceeds B_{sb} (into the small bundle–pinning regime), which is expressed as follows [11]:

$$J_c(\mathrm{B}) = J_c(0)\exp\left[-\left(\frac{\mathrm{B}}{\mathrm{B}_0}\right)^{\frac{3}{2}}\right], \tag{4.3}$$

where the fitting parameters are B_0 together with $J_c(0)$. The sample moves from the small-bundle domain to the large-bundle regime when the magnetic field strength increases. Equation (4.3) was used to get the fitted curves at 10, 15, 25, as well 30 K, which are shown by the solid red lines in the figures. Finding the locations at which the results of experiments started to deviate from the fitted curve allowed us to

calculate the values of B_{sb} as well as B_{lb}. Table 4.3 shows the estimated values for B_{sb} along with B_{lb}. According to the collective pinning regime, sample S5-5's B_{sb} and B_{lb} values were obviously higher than those of the remainder of the samples, suggesting that the extra pinning centers worked [38]. The expansion of the small and big bundle regimes under high external fields was associated with the addition of B_4C and Dy_2O_3. The pinning centers functioned effectively under the collective pinning regime, as evidenced by the maintenance of the small-bundle regime for S5-5 [39,60].

Table 4.3. Values of T_c, B_{c2}, B_{sb} as well B_{lb} at various temperature of MgB_2 bulk samples with co-additions of B_4C and Dy_2O_3.

No.	Sample name	T_c (K)	B_{c2} (T)	10 K		15 K		25 K		30 K	
				B_{sb} (T)	B_{lb} (T)	B_{sb} (T)	B_{lb} (T)	B_{sb} (T)	B_{lb} (T)	B_{sb} (T)	B_{lb} (T)
1	Pure MgB_2	38.09	14.64	0.85	3.09	0.80	2.79	0.46	1.08	0.27	0.60
2	S5-1	38.57	15.82	1.01	3.87	0.87	2.84	0.52	1.14	0.35	0.63
3	S5-2	36.43	18.51	0.67	3.27	0.65	2.31	0.41	0.97	0.21	0.45
4	S5-3	36.61	17.97	0.91	3.69	0.79	2.63	0.50	1.11	0.31	0.61
5	S5-4	34.70	18.29	0.81	3.38	0.68	2.47	0.44	1.05	0.24	0.51
6	S5-5	36.10	16.68	1.16	3.91	0.91	3.14	0.59	1.46	0.42	0.87
7	S5-6	34.97	18.49	0.88	3.58	0.71	2.56	0.47	1.09	0.29	0.58

4.5. Effect of co-additions of B_4C and Dy_2O_3 on flux pinning mechanism of MgB_2 bulk superconductors

The two predominant forms under the core pinning categorization are δl as well as δT_c. While δT_c is probably connected to changes in the Ginzburg–Landau parameter near the T_c, δl is ascribed to variations in the mean free path of charge carriers near defect sites in the crystal structure. The formulae for the dependences of J_{sv} on the decreased temperature t (where $t = T/T_c$) are different from those for δl to δT_c pinning if J_{sv} is the value of J_c in the single vortex pinning regime [38,73,93].

For δl pinning:

$$\mathrm{J_{sv}(t)/J_c(0)} = (1-\mathrm{t^2})^{5/2}(1+\mathrm{t^2})^{-1/2}\,. \tag{4.4}$$

For δT_c pinning:

$$\mathrm{J_{sv}(t)/J_c(0)} = (1-\mathrm{t^2})^{7/6}(1+\mathrm{t^2})^{5/6}. \tag{4.5}$$

The link between B_{sb} as well as J_{sv} is B_{sb}–$j_{sv}B_{c2}$ at the conclusion of the single-vortex pinning phase [11,93]. As a result, the following equations [93] may be used to determine how B_{sb} depends on t:

For δl pinning:

$$\mathrm{B_{sb}(t)/B_{sb}(0)} = [(1-\mathrm{t^2})/(1+\mathrm{t^2})]^{2/3}\,. \tag{4.6}$$

For δT_c pinning:

$$\mathrm{B_{sb}(t)/B_{sb}(0)} = [(1-\mathrm{t^2})/(1+\mathrm{t^2})]^{2}\,. \tag{4.7}$$

Figure 4.5 shows how the δl and δT_c pinning equations are applied to the experimental findings. The curvatures of the charts representing δl and δT_c are positive and negative, respectively. The samples showed a potential coexistence of δl as well as δT_c pinning processes, which is comparable to the coexistence seen in bulk MgB_2 doped with impurities [38,39]. The pinning transformation in Figure 4.5 [38] shows that if δl pinning is predominant in low-temperature zones, then δT_c pinning plays a more significant role in higher-temperature regions. These results are in line with

earlier research [47]. Electron scattering rose and the residual resistivity ratio dropped when B_4C along with Dy_2O_3 were added to the samples. This strengthened the δl pinning by lowering the mean free route of the charge carriers.

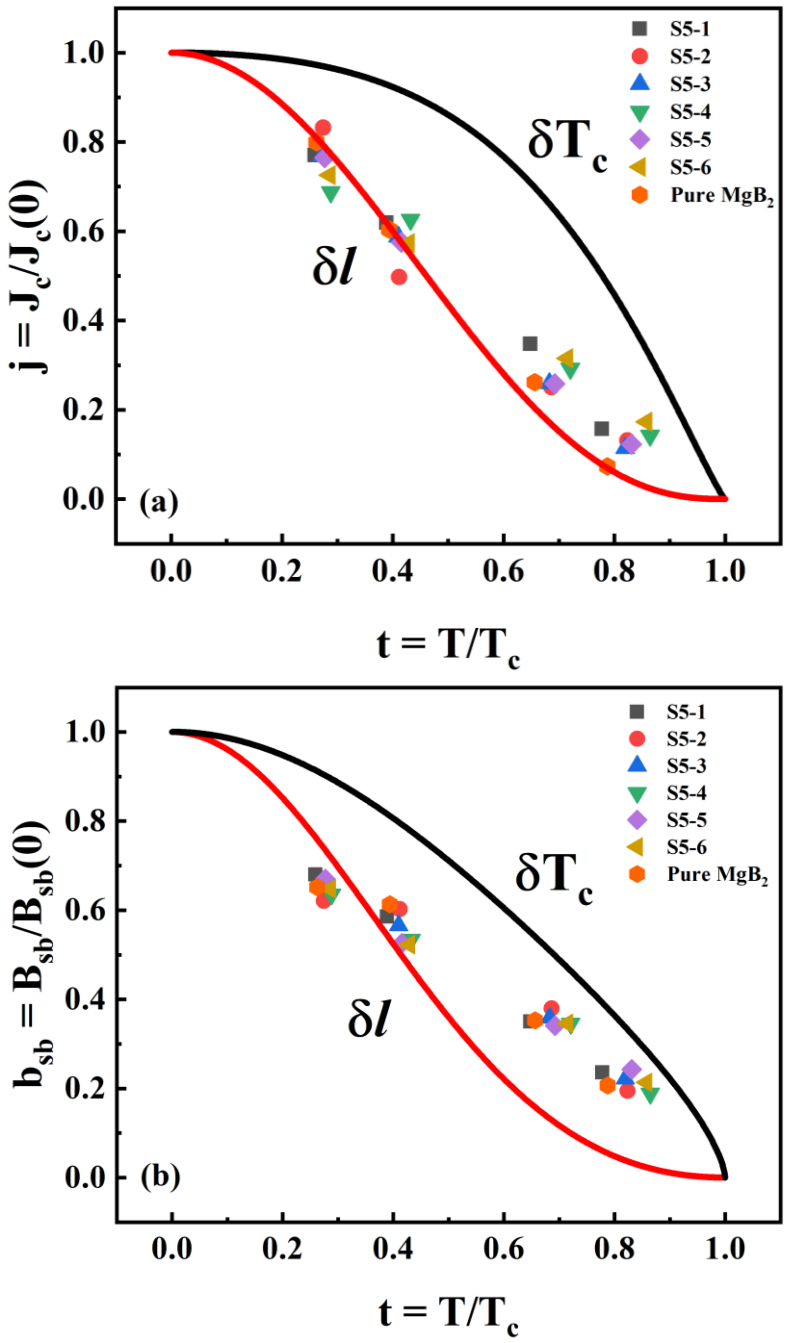

Figure 4.5. (a) Normalized temperature dependence of normalized J_c and (b) normalized B_{sb} for all samples.

4.6. Effect of co-additions of B_4C and Dy_2O_3 on geometry of pinning centers in MgB_2 bulk superconductors

The impact of incorporating B_4C along with Dy_2O_3 on the pinning qualities was further investigated using the magnetic field dependency of the flux pinning force density ($F_p = B \times J_c$) with the decreased magnetic field ($b = B/B_{irr}$) for all samples. J_c = 100 A/cm^2 at 10 K was used to establish the value of B_{irr} [70]. Figure 4.6 (a) displays F_p vs b plots, where sample S5-2 showed an increase in F_p. Figure 4.6 (b) illustrates how b affects the decreased flux pinning force density ($f_p = F_p/F_{p,max}$). The properties of other pinning centers may be investigated using the Dew–Hughes model [22].

$$f_p = \mathrm{Ab^p(1-b)^q}, \tag{4.8}$$

where the geometry of the pinning centers in the samples is represented by the fitting parameters p and q. In Figure 4.6 (b), the f-versus-b plots are displayed. When p = 1/2 and q = 2, the Dew–Hughes model predicts normal core-surface pinning; when p = 1 and q = 2, it predicts normal core point pinning. Average values of p yielded the best match to the experimental data. The location of b_{peak} was around 0.21, whereas that of $F_{p,max}$ (b_{peak}) was roughly 0.552. These data show that core-correlated pinning, which could be mostly linked to grain boundaries, was the predominant pinning in the sample [38]. A prior study demonstrated that the grain boundaries in MgB_2 bulk samples pin the intrinsic pinning centers' natural form. By filling the gaps and improving the connection between MgB_2 grains, the addition of 5 weight percent B_4C and 2.0 weight percent Dy_2O_3 may increase the significance of surface pinning. Figure 4.6 (c) illustrates the change in b_{peak} to a greater value.

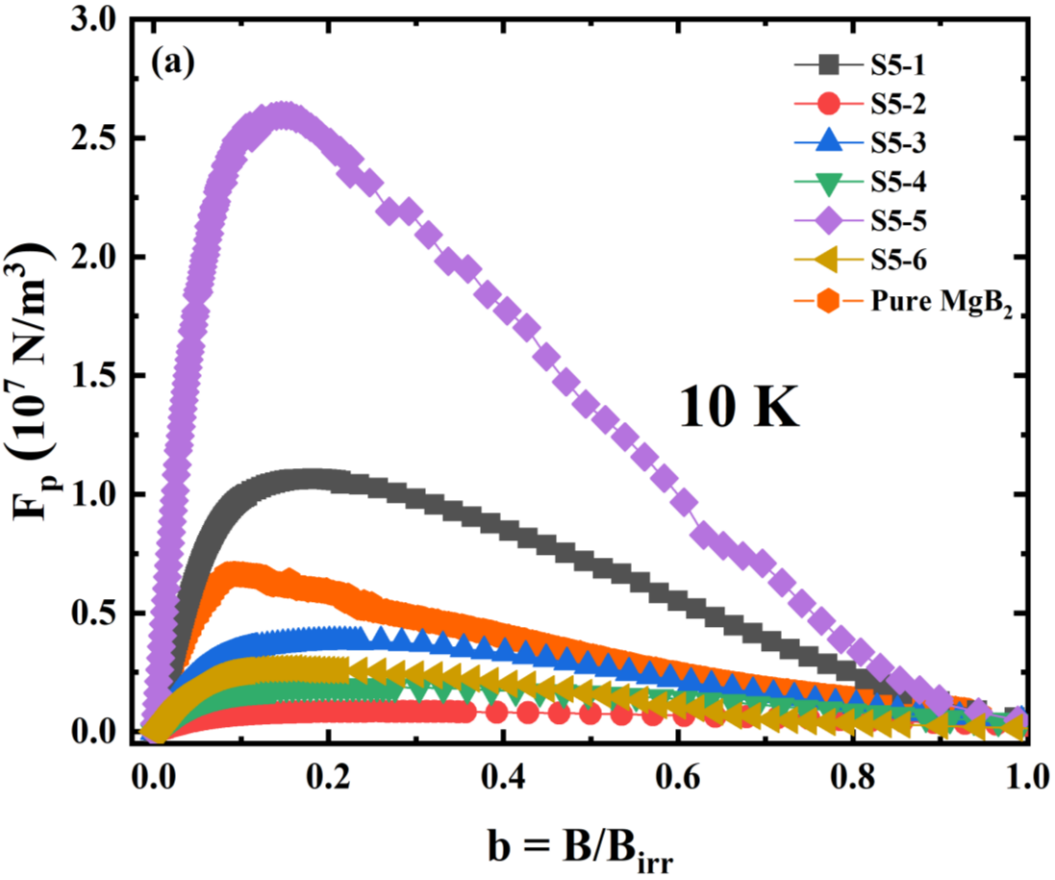
(a)
S5-1
S5-2
S5-3
S5-4
S5-5
S5-6
Pure MgB2
10 K
Fp (10^7 N/m^3)
b = B/Birr
3.0
2.5
2.0
1.5
1.0
0.5
0.0
0.0
0.2
0.4
0.6
0.8
1.0

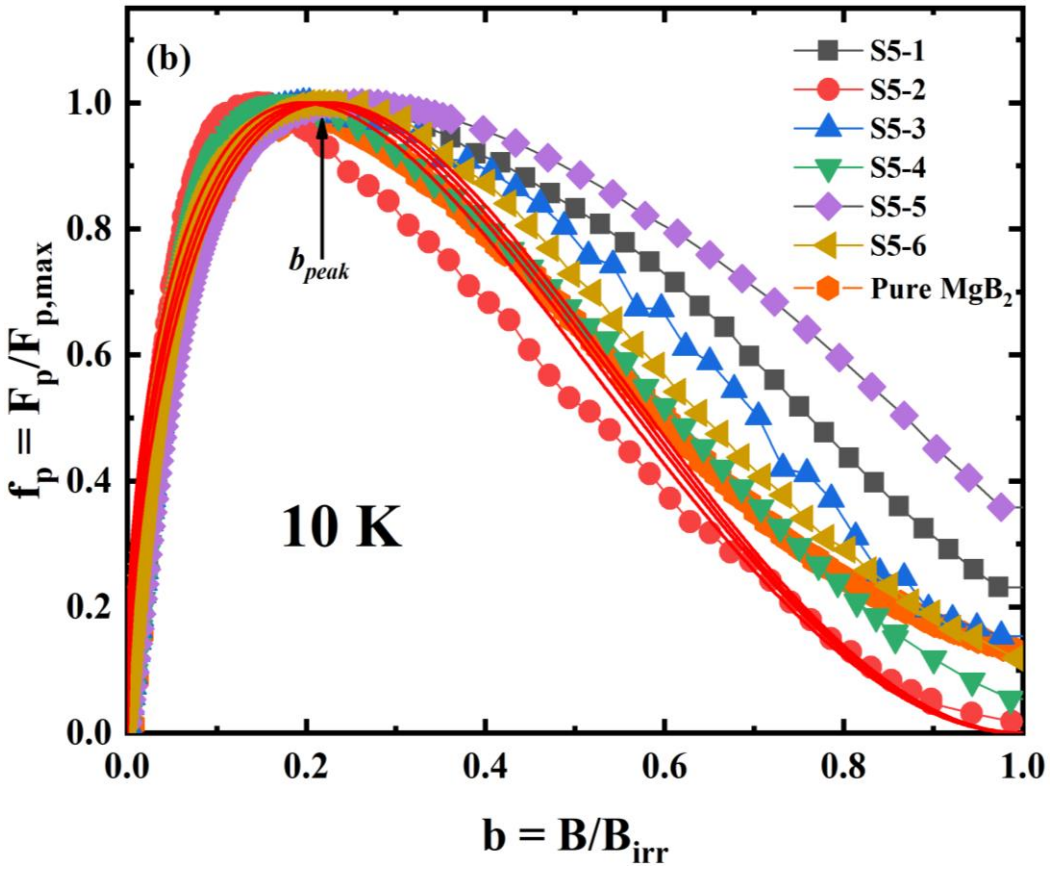
(b)
S5-1
S5-2
S5-3
S5-4
S5-5
S5-6
Pure MgB2
bpeak
10 K
fp = Fp/Fp,max
b = B/Birr
1.0
0.8
0.6
0.4
0.2
0.0
0.0
0.2
0.4
0.6
0.8
1.0

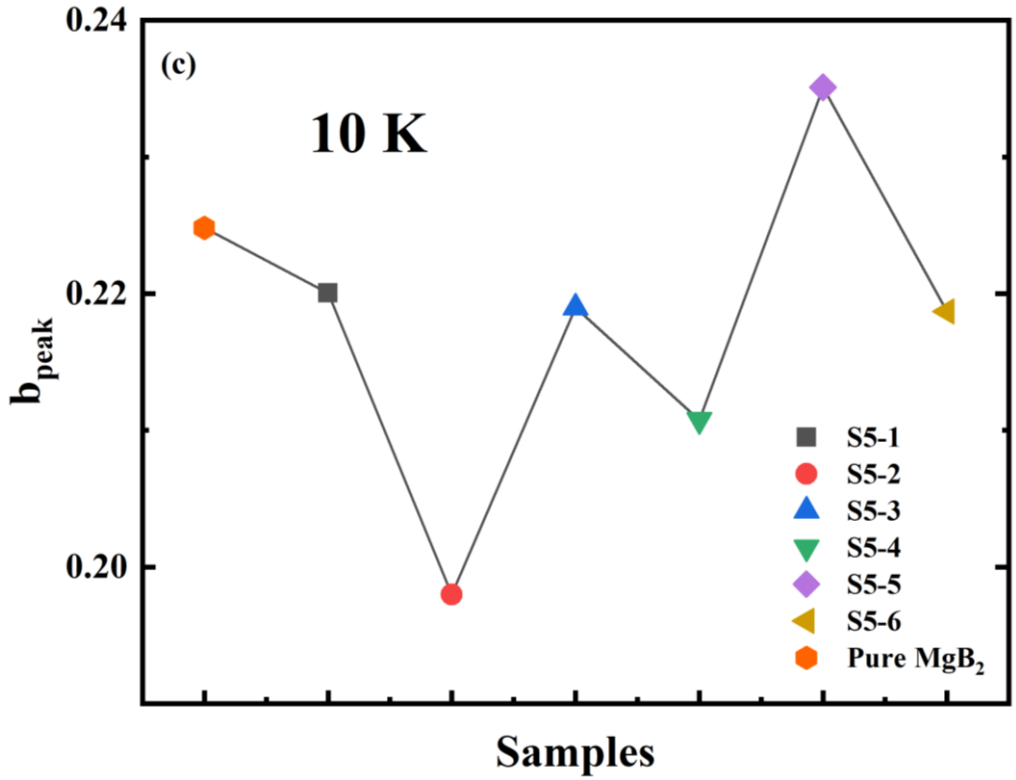

Figure 4.6. Reduced field dependency of MgB_2 bulk samples at 10 K in terms of (a) F_p, (b) f_p, and (c) b_{peak}.

Conclusion of Chapter 4

It is stated that MgB_2 bulk samples codoped with B_4C along with Dy_2O_3 have better flux pinning characteristics. The produced samples' crystal structures and superconducting characteristics, including their T_c, B_{c2}, and J_c, were thoroughly examined. XRD investigations showed that the incorporation of B_4C along with Dy_2O_3 caused slight lattice distortions, which corresponded to the slight change in the T_c derived from $\rho(T)$. The sample with the co-addition of 5 weight percent B_4C and 2.0 weight percent Dy_2O_3 showed the largest rise in J_c, which increased by about 5 to 8 times in the range of 0.1 to 2 T at 10 K. At the same time, the sample with 5 weight percent B_4C showed the largest increase in B_{c2}, increasing by approximately 1.6 to 1.7 times at 0 K. The thorough investigation of the temperature dependency of the dominant pinning mechanism in MgB_2 bulk samples with co-additions of B_4C along with Dy_2O_3 utilizing the collective pinning theory is one of the most intriguing

findings here; these investigations were recently conducted in several research. The results showed that δl pinning was the most common type of pinning. The samples' two-dimensional pinning center geometry was connected to the grain boundaries. The right production parameters for MgB_2 bulk samples can be improved with the help of these discoveries.

Chapter 5: ENHANCEMENTS OF CRITICAL CURRENT DENSITY OF MgB_2 THIN FILM WITH Sn^{2+} IRRADIATION

Ion irradiation has a greater effect on the in-field J_c as well as B_{c2} of MgB_2, as discussed in Chapter 1 [62,98]. Columnar failures along the ion tracks, which are a powerful source of flux pinning and are often produced by high-energy heavy-ion irradiation within superconducting materials, frequently enhance the J_c as well as B_{c2} of high-T_c cuprate superconductors [110]. Furthermore, ion irradiation may induce defects in the target materials mainly through the nuclear stopping of energetic ions, while the exact mechanism of defect creation is still up for question [61]. Type-II superconductors are frequently useful for enhancing key superconducting properties, particularly the in-field J_c as well B_{c2}, since defects in these materials may interfere with vortex migration. Consequently, the scientific advancement and practical use of superconductors depend on a knowledge of how flaws impact the fundamental characteristics of superconductivity [29].

This chapter has examined the effects of 2 MeV Sn^{2+} ion irradiation at dosages ranging from 2E12 to 7E13 on the T_c, in-field J_c, as well B_{c2} of MgB_2 thin film samples produced on an Al_2O_3 substrate. Highly c-axis-oriented 412-nm-thick MgB_2 was produced using a hybrid physical-chemical vapor deposition process (HPCVD) on *c*-cut Al_2O_3 substrates. At room temperature, ion irradiation was carried out using the Faculty of Physics' HUS-5SDH-2 twin pelletron accelerator system. Doses of 2×10^{12} (2E12), 2×10^{13} (2E13), 5×10^{13} (5E13), and 7×10^{13} (7E13) atoms/cm^2 were applied to 2 MeV energetic Sn ions at a tilt angle of 7° in order to avoid channeling effects. To find the mean projected ranges (R_p) and damage events of the Sn ions, the Stopping and Range of Ions in Matter (SRIM) Monte Carlo simulation program was utilized.

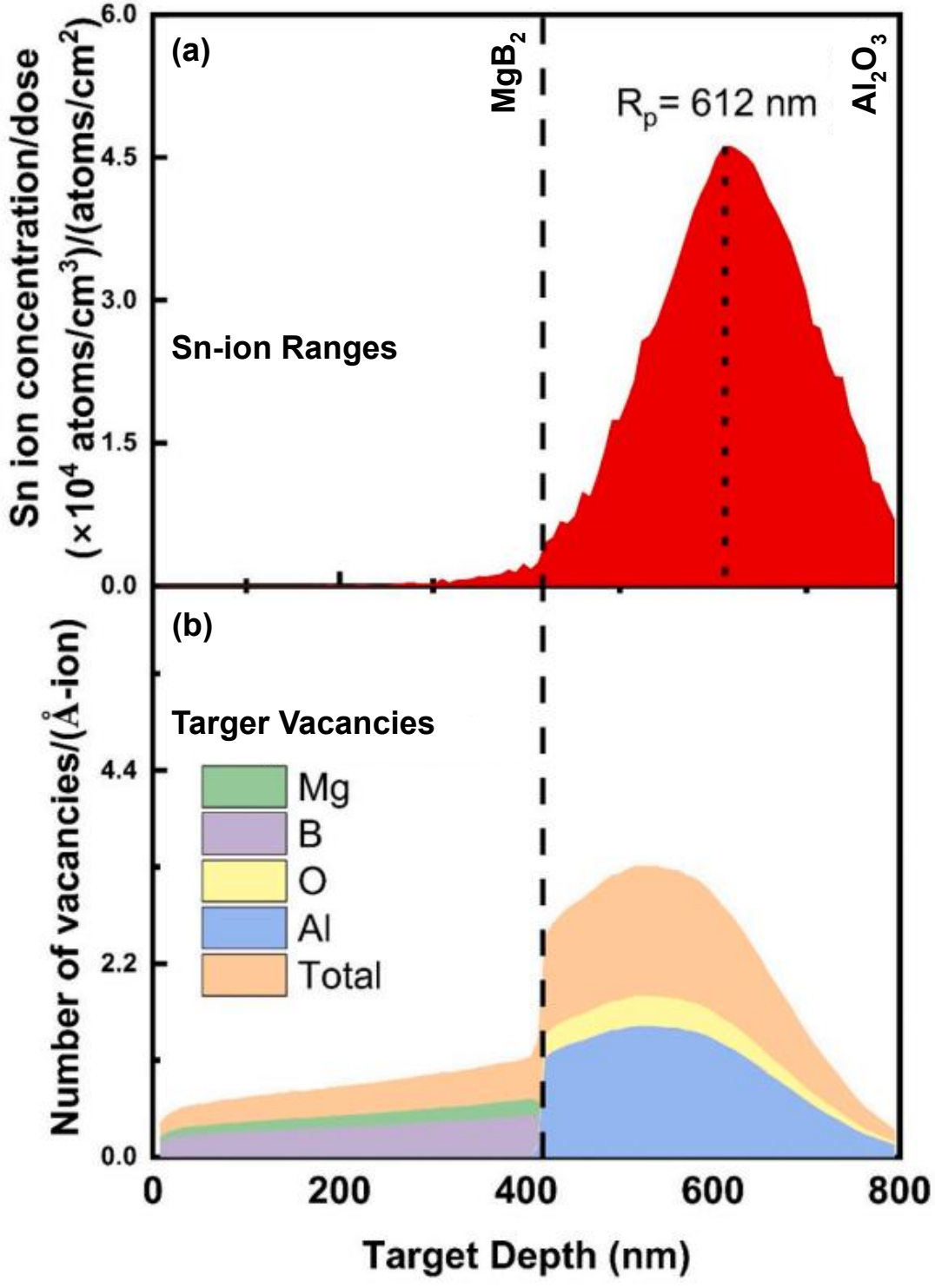

Figure 5.1. (a) A 412 nm thick MgB_2 thin film produced on a c-cut Al_2O_3 substrate was exposed to a range of 2 MeV Sn ions, (b) target vacancy count as a function of target depth produced by 2 MeV Sn-ion irradiations [67].

Changes in T_c as well as B_{c2}, however, have not been thoroughly examined. Raman spectroscopy is crucial in determining the influence of certain phonon characteristics on the T_c as MgB_2 is a superconductor made possible by phonons. To ascertain how the disorder effect and EPC evolved over time, a number of irradiation MgB_2 films were investigated. T_c variations of MgB_2 thin film samples were examined by means of a systematic study of the behavior of EPC by Raman spectroscopy. When comparing the irradiated MgB_2 thin film samples to the pristine sample, the critical temperature dramatically dropped while the B_{c2} and J_c rose. These results imply that ion irradiation-induced displacement plays a crucial role in altering the T_c, in-field J_c, as well as B_{c2}. It was examined how closely the EPC from Raman analysis and superconducting qualities relate to one another. Furthermore, this dissertation use a comparison approach using MFM Meissner curves to show penetration depth data at 4.26 K. The findings show how the penetration depth (λ) along with coherent length (ξ) of pristine and irradiated MgB_2 thin film samples relate to the B_{c2} and thermodynamic critical fields (B_{c2}). Table 5.1 lists the samples' names and other information.

Table 5.1. Details of Sn^{2+} ion irradiated MgB_2 thin film names and ion doses

No.	**Dose (atoms/cm^2)**	**Sample Name**
1	0	Pristine
2	2×10^{12}	2E12
3	2×10^{13}	2E13
4	5×10^{13}	5E13
5	7×10^{13}	7E13

5.1. Effect of Sn^{2+} ion irradiation on T_c and RRR of MgB_2 thin film superconductors

To ascertain the samples' superconductivity, the temperature dependency of their resistivity was investigated. The experimental results are displayed in Figure 5.2. All of the samples showed metallic behavior in the high temperature region, where their resistance dropped linearly with temperature. As the temperature gradually dropped, the superconducting transition took place. $T_{c/on}$ was the temperature at which the sample's resistivity departed from linearity, and $T_{c/off}$ was the temperature at which it entirely disappeared. Stated differently, the superconducting phase transition starts and ends at the two temperatures [25]. The transition width was determined using the formula $\Delta T_c = T_{c/on} - T_{c/off}$. The inset of Figure 5.2 displays the zoomed-in region of (T) surrounding T_c. The T_c of the samples was obviously reduced by the irradiation Sn^{2+} ions. The Pristine sample's T_c was calculated to be around 39.65 K. At a dosage of 2E12, the irradiated sample's T_c value plummeted to about 38.70 K, and when the dose of Sn^{2+} ions increased, it subsequently decreased monotonically. These results are believed to be caused by different lattice distortions in samples of MgB_2 thin films. By modifying the local texture, which manifests as an increase of Mg-B and Mg-Mg bond lengths, it was shown that ion irradiation tends to change the T_c of MgB_2 thin film samples [91]. Furthermore, strain-induced local structural modification, that is the distortion and clutter of the crystal lattice, was shown to have a considerable impact on the T_c fluctuation of MgB_2 [42,69].

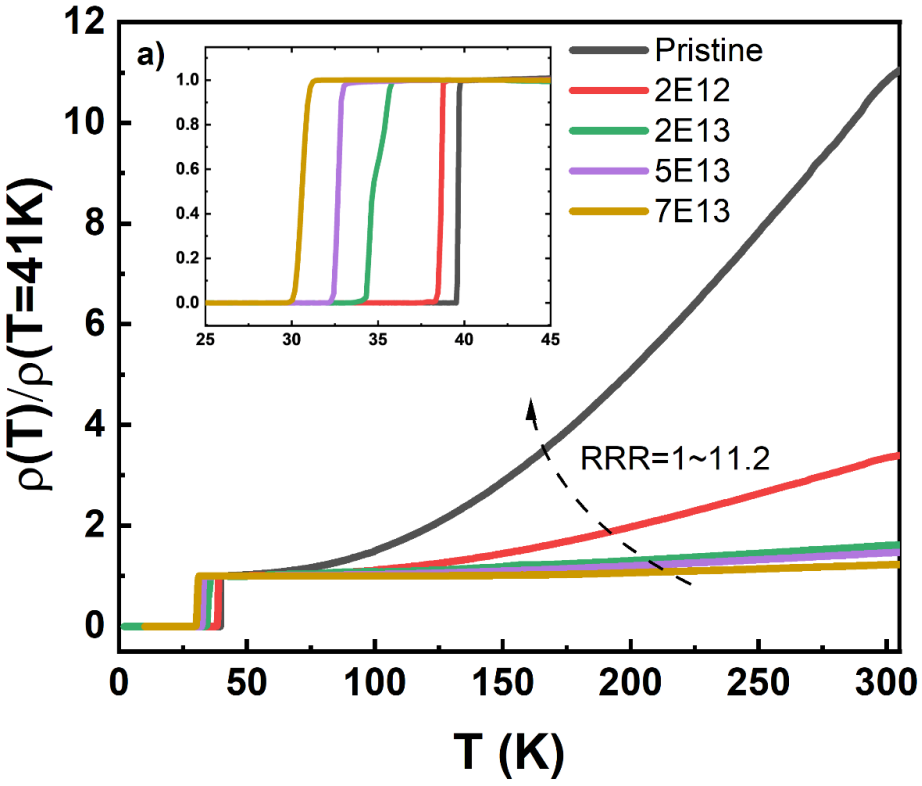

Figure 5.2. Normalized resistivity, $\rho(T)/\rho_n$, as a function of temperature for every sample. The zoom area plot in the inset has a smaller normalized resistivity range of 0.0–1.0 and a smaller temperature range of 25–45 K.

The residual-resistance ratio gauges the superconductor's purity and structure by analyzing the temperature dependence of electron scattering in the normal conducting state. The MgB_2 thin film samples' residual resistance ratio (RRR) is described as [16]:

$$\mathrm{RRR} = \frac{\rho_{300K}}{\rho_{41K}}, \tag{5.1}$$

where the resistances of the MgB_2 thin film samples at 300 K and 41 K are denoted by ρ_{300K} and ρ_{41K}, respectively. The T_c value, which was recorded at 30.47 K, was lowest in the sample that received the dosage of 7E13. These samples had distinct residual resistance ratios (RRR); the pristine sample had an RRR value of 11.2 while the 7E13 sample had an RRR value of 1. In close relation to the Sn^{2+} ions, the RRR

value dropped as the ion dosage increased. Lattice disorder following irradiation may be the cause of the shift in the RRR values.

5.2. Effect of Sn^{2+} ion irradiation on electron-phonon coupling properties of MgB_2 thin film superconductors

Electron-phonon interactions play a major role in the pairing process that results in MgB_2 superconductivity since it is a phonon-mediated superconductor. The E_{2g} phonon mode has been observed lately to be the sole initial-order active mode among the optical modes of MgB_2 (A_{2u}, B_{1g}, E_{1u}, as well as E_{2g}) [118]. Three major peaks may be seen in the 200–1000 cm^{-1} range: the bigger phonon ridge, which is mostly focused at 740–800 cm^{-1}; the intermediate ridge, which is concentrated at 580–610 cm^{-1} (E_{2g}); and the shorter phonon ridge, which is primarily focused at 455–490 cm^{-1}. The Raman spectra of MgB_2 also shows E_{2g} ridge widening, which is brought on by the samples' higher phonon density [116,118]. Although most of the superconducting capabilities of MgB_2 originate in the boron plane, the E_{2g} mode is Raman operational and strongly associated with the electronic conveyance of bands. Consequently, Raman scattering works well for examining this phonon mode and might offer important information on crystal symmetry, impurities, and grain size. Similarly, Raman scattering is strongly affected by residual stress and disorder [15,76], which can change the phonon frequencies and lifetime. While predictions of the frequency of the E_{2g} mode are around 515 cm^{-1} (64 meV) and 665 cm^{-1} (82 meV) [63], respectively, experiments have shown a broad Raman mode in the range of 600 cm^{-1} and 630 cm^{-1} [76].

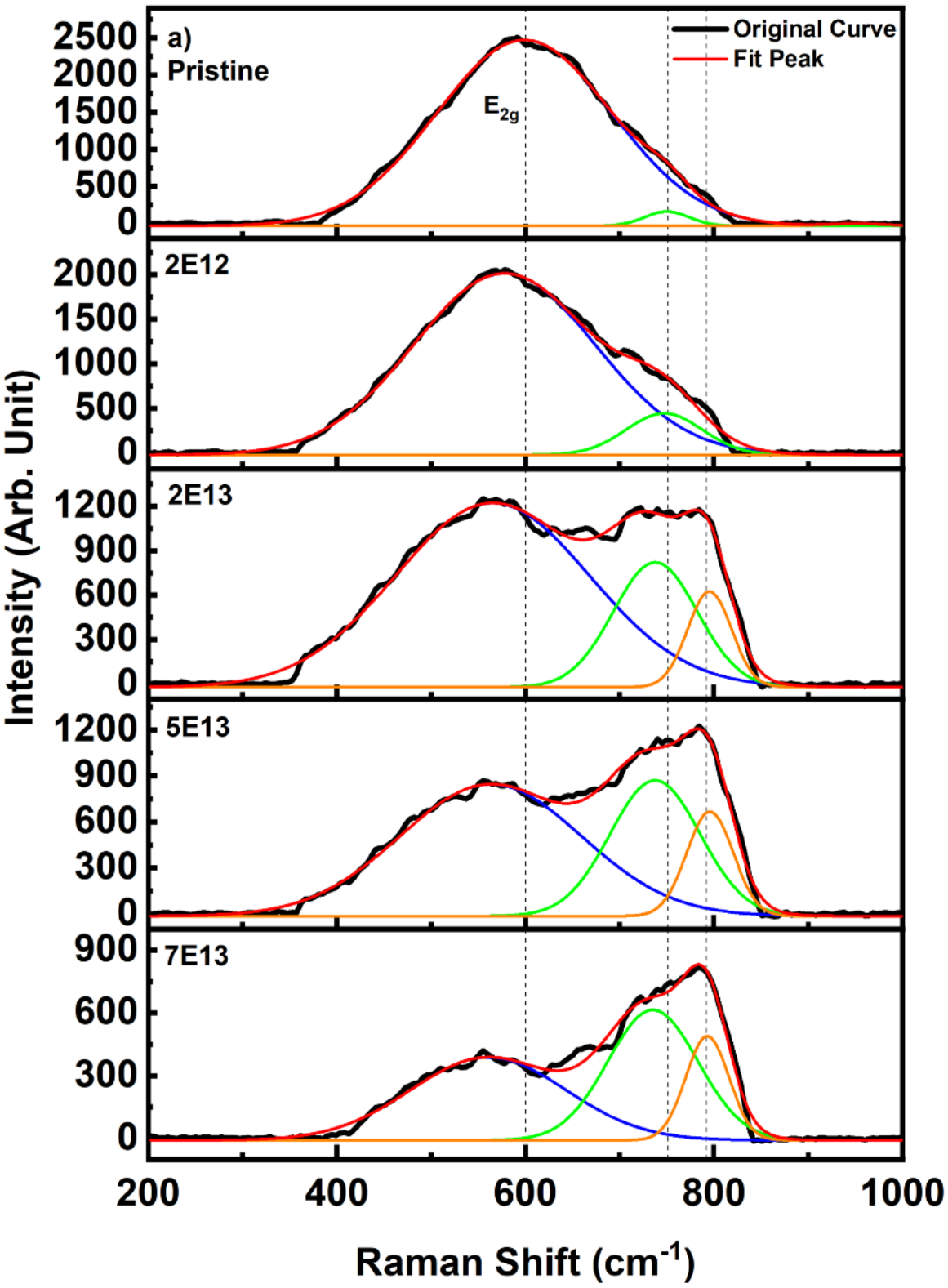
a)
Pristine
E_{2g}
Original Curve
Fit Peak
2E12
2E13
5E13
7E13
Intensity (Arb. Unit)
Raman Shift (cm^{-1})

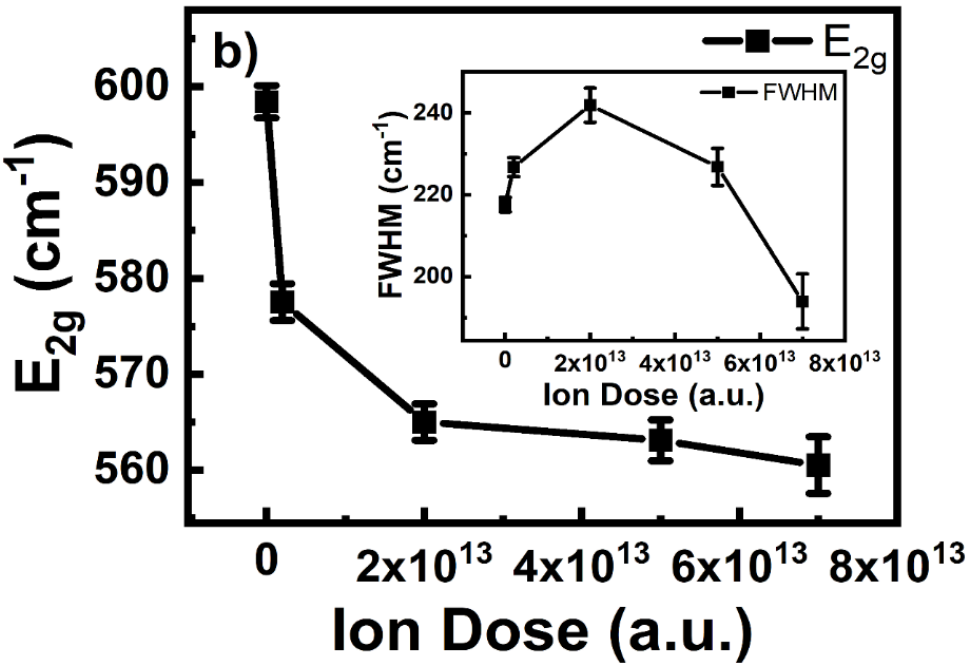
b)
E2g
FWHM
FWHM (cm-1)
240
220
200
0
2x1013
4x1013
6x1013
8x1013
Ion Dose (a.u.)
E2g (cm-1)
600
590
580
570
560
0
2x10^13
4x10^13
6x10^13
8x10^13
Ion Dose (a.u.)

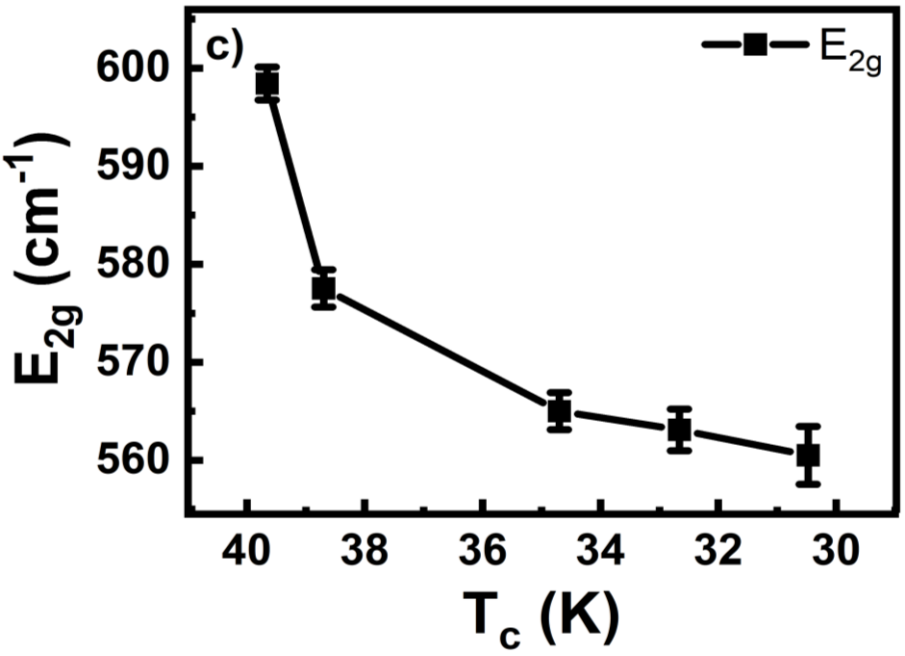
c)
E2g
E2g (cm-1)
600
590
580
570
560
40
38
36
34
32
30
Tc (K)

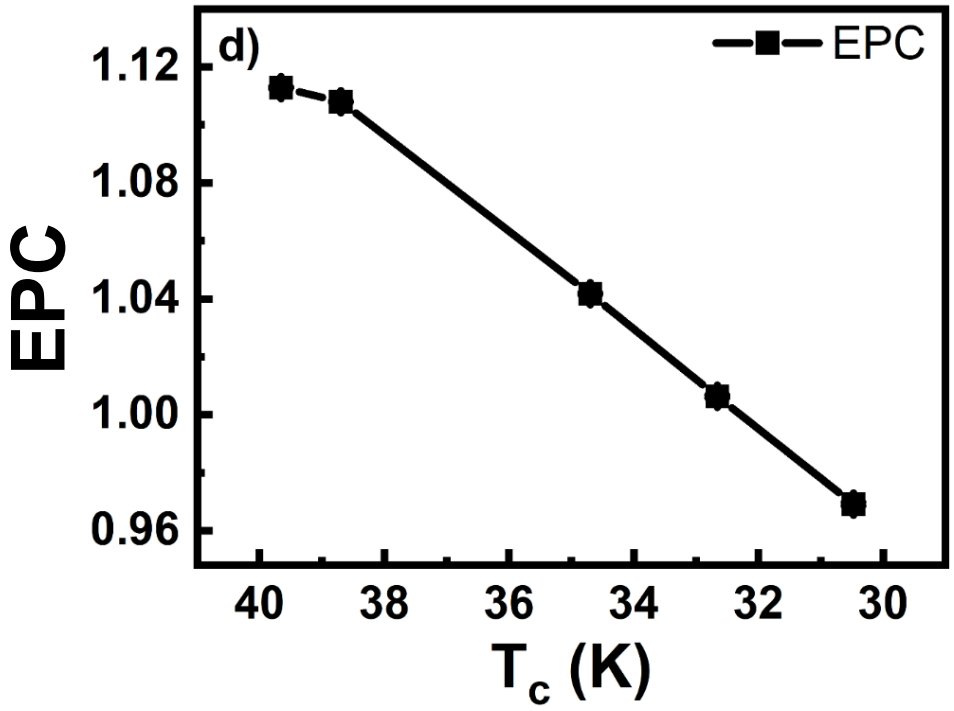

Figure 5.3. (a) The E_{2g} mode (blue) and two PDOS (green and orange) of MgB_2 thin film samples with varying ion doses are fitted to the Raman spectra, (b) Dependence of the E_{2g} peak position on ion doses, (c) Dependence of the E_{2g} peak position on the critical temperature (T_c), (d) Dependence of the electron–phonon coupling constant (EPC) on the critical temperature (T_c).

In general, the Raman spectrum of Sn^{2+} irradiation films is significantly influenced by the Sn^{2+} ion fluence. As the E_{2g} ridge moves as a result of phonon hardening and softening, the Sn^{2+} ion functions as a phonon toughening and loosening layer inside MgB_2. Each Raman observation was fitted using Gaussian fits, and the fitting outcomes are shown in Table 5.2. The Raman spectrum changes of the Sn^{2+} irradiated MgB_2-thin films were analyzed by utilizing Gaussian fitting to determine the peak positions of the samples. The observed Raman spectra of the pristine and Sn^{2+} ion-irradiated MgB_2 thin film samples are displayed in Figure 5.3 (a). The E_{2g} peak's breadth and intensity progressively declined and moved to the left as the irradiation dosage rose from 2E12 to 7E13. The pristine sample's E_{2g} peak location was around 598 cm^{-1}, and it progressively dropped to a minimum for sample 7E13. The relationship between the E_{2g} peak location and the ion irradiation dosage is seen in

Figure 5.3 (b). In particular, sample 2E12's peak E_{2g} was observed at 577 cm^{-1}, while sample 7E13's E_{2g} progressively dropped to 560 cm^{-1}. Table 5.2 lists the precise positions of the samples' E_{2g} peaks. As the irradiation dosage increased, these peaks' intensity also reduced in tandem with the location change. The shift might be attributed to lattice distortions brought on by ion irradiation. As a function of the ion irradiation dosage, the full width at half maximum (FWHM) of the E_{2g} peak is displayed in the inset of Figure 5.3 (b). The E_{2g} peak's FWHM rose from 217.591 (pristine) to 241.893 (5E13) before falling to 193.893 (7E13). This indicates that clean MgB_2 has a high EPC as the Pristine sample's E_{2g} mode's FWHM is more than 217 cm^{-1}. Prior observations of this phenomena have also been made in bulk as well as thin-film MgB_2 materials [69,112]. Strong electron-phonon coupling, phonon-phonon interaction, and lattice relaxation surrounding the impurity Sn atom site can all contribute to the reduction in E_{2g} peak location, breadth, and intensity. The change in T_c is quite comparable to this. The E_{2g} peak position's dependency on T_c is seen in Figure 5.3 (c). T_c dropped as the E_{2g} peak position dropped. This suggests that a significant contraction in E_{2g} is the cause of the observed drop in T_c.

The peaks at 750 cm^{-1} and 792 cm^{-1} in Figure 5.3 (a) for the clean sample and 2E12 sample have a negligible impact on the critical temperature. The materials' Raman spectra were almost symmetrical. A little peak was seen at 750 cm^{-1} when the irradiation dosage was raised to 2E12. Additionally, we saw two peaks at 750 cm^{-1} and 792 cm^{-1} as the irradiation dosage increased. The dosage of ion irradiation causes these peaks to become more intense. The peaks in the phonon density of states (PDOS) are responsible for the peaks at locations 750 cm^{-1} and 792 cm^{-1} [114]. When the Sn^{2+} ions are irradiated onto the MgB_2 thin film samples, residual stress, disordered and faulty systems, and lattice distortions can all contribute to this. With varying amounts of Sn^{2+} ion irradiation, the frequency of PDOS may be considerably changed. The E_{2g} mode is the primary source of the Raman spectra in disordered systems. Indicating and elucidating the connection between the Raman signals and

the superconducting characteristics of the pristine and Sn^{2+} ion-irradiated MgB_2 thin film samples, this highlights the significance of the E_{2g} mode.

The McMillan formula states that the average phonon frequency and T_c have an inverse relationship [74]. Thus, the active phonon frequency E_{2g} in MgB_2 has a comparable effect on T_c fluctuation. To further understand the contribution of E_{2g} to the values of T_c in our MgB_2 samples, we computed the Bardeen–Cooper–Schrieffer theory (BCS) provided by the McMillan Formula updated by Allen–Dynes [74]:

$$T_c = \frac{\langle \omega_{log} \rangle}{1.2} exp\left(-\frac{1.04(1+\mathrm{EPC})}{\mathrm{EPC}-\mu^*(1+0.62*\mathrm{EPC})}\right), \quad (5.2)$$

where the average phonon frequency is $\langle \omega_{log} \rangle = (690 \times \omega^2_{E2g} \times 390)^{0.25}$, and the phonon frequencies of the other modes in the MgB_2 system are 390 and 690 cm^{-1}. The Coulomb pseudopotential, denoted by μ*, is 0.13 [91], and the electron-phonon coupling constant is written as EPC. The EPC values for the MgB_2 film samples may be calculated using the method by utilizing the T_c values in Figure 5.2 and the E_{2g} mode frequency in Figure 5.3 (a). Figure 5.3 (d) shows how EPC values vary with T_c. When they are present, as the ion dosage increases, Raman shifts and EPC values fall. This suggests that ion irradiation-induced T_c suppression results from the suppression of both the Raman shift and EPC values, and that EPC falls as the Raman Shift increases. Similarly, when exposed to Sn^{2+} ions, the disorder results in significant impurity scattering rates. The degree of disorder affects the electronic system, which suppresses the electron-phonon coupling constant and affects the superconducting process of MgB_2.

Table 5.2. Results summary for samples of MgB_2 thim film: residual resistivity $\rho_{41\,K}$, upper critical field $B_{c2}(0)$, coherence length ξ, irreversible field B_{irr}, the frequency of the E_{2g} mode, the critical temperature (T_c) and the electron–phonon coupling constant (EPC)

Samples	**Dose (cm^{-2})**	**$\rho_{41\,K}$ (μΩcm)**	**$B_{c2}(0)$ (T)**	**ξ (0) (nm)**	**B_{irr} (T)**	**E_{2g} (cm^{-1})**	**T_c (K)**	**EPC**
Pristine	0	0.516	5.89	7.48	2.23	598.42	39.65	1.113
2E12	2×10^{12}	0.695	7.62	6.58	3.52	577.53	38.70	1.108
2E13	2×10^{13}	1.836	11.74	5.29	4.56	565.50	34.69	1.042
5E13	5×10^{13}	4.057	12.94	5.05	6.49	563.09	32.66	1.006
7E13	7×10^{13}	5.279	12.80	5.07	5.74	560.49	30.47	0.969

5.3. Effect of Sn^{2+} ion irradiation on the improvement of J_c of MgB_2 thin film superconductors

The enhancement of the in-field J_c is also covered. The magnetic dependency of J_c in the irradiated and pristine samples at 10 K is displayed in Figure 5.4 (a). The J_c of the pristine MgB_2 thin film samples used in this study was significant at zero field and rapidly disappeared in magnetic fields. J_c was calculated using the magnetization hysteresis (M-H) loops using Bean's critical state model. The in-field J_c was considerably increased following Sn^{2+} ion irradiation, according to the results. At around 1.33 T, the J_c value of the irradiated film seems to be equal to the J_c value of the pristine sample. For instance, samples 2E12, 2E13, 5E13, and 7E13 had J_c Values of 131.20, 304.30, 382.22, and 274.19 kA/cm^2, respectively, at 10 K and 2 T, whereas the pristine sample had a J_c value of 12.54 kA/cm^2. The best J_c value was shown by sample 5E13 when the magnetic field was increased. The J_c value of sample 5E13 was 138.38 kA/cm^2 at 4 T, 65.40 kA/cm^2 at 5 T, and 16.18 kA/cm^2 at 6 T at a

temperature of 10 K. Compared to the other samples at the same temperature and magnetic field, these results are much greater. Upon reaching 4.42 (5E13) and 3.38 T (7E13) at 10 K, the irradiated samples' J_c remained over 105 A/cm^2. For real-world uses, a J_c of 10^5 A/cm^2 is suitable [111]. From 2.23 (Pristine) to 6.49 T (5E13), the irreversible field (B_{irr}) assessed at a J_c of 100 A/cm^2 increases by more than three times. J_c and B_{irr}'s actions are comparable to those described by Jung *et al.* [83]. Since the greatest value of B_{irr} obtained at 10 K using low-energy irradiation in previous experiments is usually less than 5 T [53,83], Sn^{2+} irradiation increased the J_c(B) of MgB_2. These findings imply that Sn^{2+} irradiation could improve practical superconducting wires' current-carrying capacity.

For J_c(B) at 10 K, the double-logarithmic plots are displayed in Figure 5.4 (a). In both the low- and high-field areas, single vortices were pinned by a field-independent J_c, which is consistent with the flux-pinning mechanism described by the power law $J_c \sim B^{-\beta}$. According to the collective pinning theory [52], a type-II superconductor's pinning effectiveness is shown by the exponential (Figure 5.4 (b)). At 10 K, the value of the fitted β consistently decreased from 1.12 (pristine) to 0.65 (5E13), then increased to 0.68 (7E13), indicating a change in the pinning mechanism from weak collective (β = 1) to strong plastic pinning (β = 0.5) [21,52]. Among the compounds with the lowest β, 5E13 was the most effective in raising the field-dependent J_c.

When exposed to Sn^{2+} ions at a dosage of 5×10^{13} ions/cm^2 and an energy of 2 MeV, the J_c of the MgB_2 thin film samples reached a value of around 2.5×10^6 A/cm^2. This number, which is around ~2.5 times higher than the previously published values (~1×10^6 A/cm^2), was obtained with an external magnetic field of 0.1 T. The J_c value rose by around ~25 times when the field was 1.5 T and by almost ~1000 times when the field was 2 T in comparison to the previous results. Table 5.3 below displays the particular comparative findings.

Table 5.3. Comparison of J_c values of sample 5E13 with other samples in previous studies

Samples	J_c (A/cm^2) at 10 K					Ref.
	0.1 T	0.5 T	1 T	1.5 T	2 T	
MgB_2 thin film samples irradiated with Sn^{2+} ions at a dose of 5x10^{13} ions/cm^2 and an energy of 2 MeV.	2.5 ×10^6	8.0 ×10^5	4.5 ×10^5	2.5 ×10^5	2.0 ×10^5	This work
MgB_2 thin film samples irradiated with O ions at a dose of 1x10^{14} ions/cm^2 and an energy of 200 keV.	1.0 ×10^6	4.5 ×10^5	1.8 ×10^5	1.0 ×10^4	2.0 ×10^2	[83]
MgB_2 thin film samples irradiated with Co ions at a dose of 1x10^{14} ions/cm^2 and an energy of 140 keV.	1.2 ×10^6	7.0 ×10^5	3.0 ×10^5	0.6 ×10^5	4.0 ×10^3	[55]

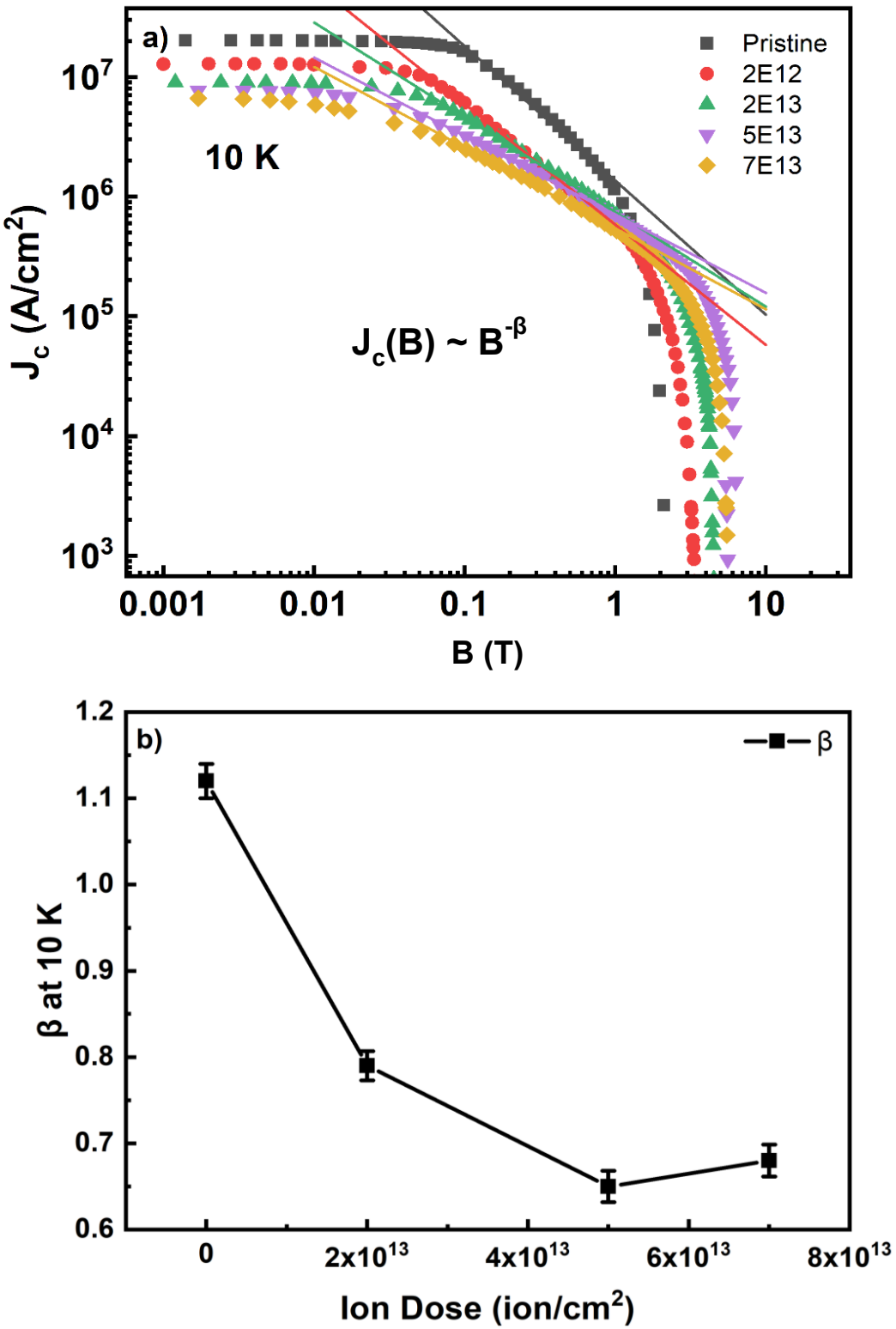

Figure 5.4. (a) The 5E13 sample's double log J_c at 10 K, (b) $J_c \sim B^{-\beta}$, a power-law relation, was seen at 10 K.

5.4. Effect of Sn^{2+} ion irradiation on B_{c2} of MgB_2 thin film superconductors

The effect of Sn^{2+} irradiation on the B_{c2} of the MgB_2 thin film samples was examined by measuring the electrical resistivity as a function of temperature for magnetic fields applied perpendicular to the *ab*-plane. We showed in our earlier work [67] that sample 5E13 has the best ion dosage, resulting in good in-field J_c as well B_{c2} values. The in-field ρ(T) curves for the Pristine sample and the sample exposed to Sn^{2+} ions with 5E13 fluence are displayed in Figure 5.5 (a) and (b), respectively, as the applied field increases from 0 T to 7 T. The optimal fluence for raising B_{c2} in this investigation is 5E13. B_{c2} was determined to be the midway of the superconducting transition, and the in-field ρ(T) was normalized by the resistivity of the normal state (n) for each magnetic field for comparison. Plotting the B_{c2} of each sample against temperature for varying ion dosages is shown in Figure 5.5 (c). Figure 5.5 (c) displays solid lines representing the B_{c2}(T) fitting curves of the irradiated and pristine MgB_2 films. According to the two-band Ginzburg–Landau (GL) hypothesis, all B_{c2}(T) curves were adequately described [5]. With d ≪ ξ_{eff}, λ, this dissertation obtain [5] for thin films:

$$B_{c2} = \frac{\theta^{1+\alpha}}{(1-(1+\alpha)\omega + \ell\omega^2 + m\omega^3)}, \tag{5.3}$$

where $\theta = \left(1 - \frac{T}{T_c}\right)$; $\omega = (1-\theta)\theta^{1+\alpha}$. B_{c2} values were obtained using a resistivity threshold of 50% of the superconducting transition. At 5.889 T, the pristine sample's B_{c2}(0) rose significantly with increasing fluence to a maximum of 12.941 T at 5E13. Then, as the dose increased, it steadily decreased. Although Sn^{2+} irradiation increases B_{c2}(0), T_c suppression in MgB_2 thin film samples by Sn^{2+} ion irradiation is rather small and similar to the results of irradiating MgB_2 with other particles, such as oxygen ions, α particles, and neutrons [33,105]. Furthermore, B_{c2} may suffer from the severe lattice distortions brought on by the substitution of Sn^{2+} ions for boron. B_{c2} was calculated using σ band scattering [33]. When the dose of Sn^{2+} ions was modest, some of them substituted boron and alloyed into MgB_2 grains. As a result, the boron layer becomes chaotic, leading to a large amount of in-plane σ scattering. As the

damage increased, more point-like flaws were created both inside and between the MgB_2 grains [105]. Along with charge doping, Sn^{2+}-related defects caused a considerable distortion of the lattice structure, which resulted in significant in-plane and out-of-plane scattering. Our results imply that B_{c2} (0) can be enhanced by Sn^{2+} ion irradiation. Enhancing key superconducting properties like B_{c2} and in-field J_c while lowering T_c is advantageous when the superconducting layer has not been damaged.

In previous studies, the MgB_2 films irradiated He ions sample had a B_{c2} value of about 8.9 T [36], the MgB_2 films irradiated Co ions sample had a B_{c2} value of about 9.5 T [55], while the B_{c2} of most of the MgB_2 films by Sn^{2+} ion irradiation were all > 11.7 T. Specifically, sample MgB_2 thin films by Sn^{2+} ion irradiation at a dose of 5×10^{13} ions/cm^2 and an energy of 2 MeV (5E13) has a B_{c2} value of 12.941 T, about 1.4 – 1.5 times higher than the doped samples in previous studies.

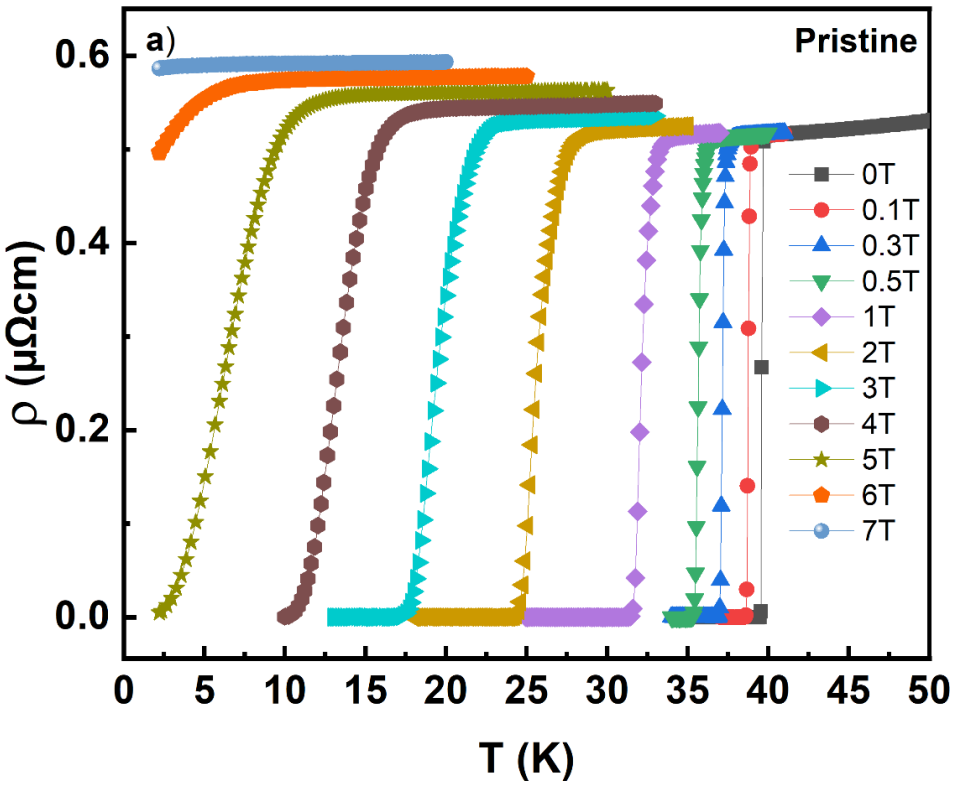

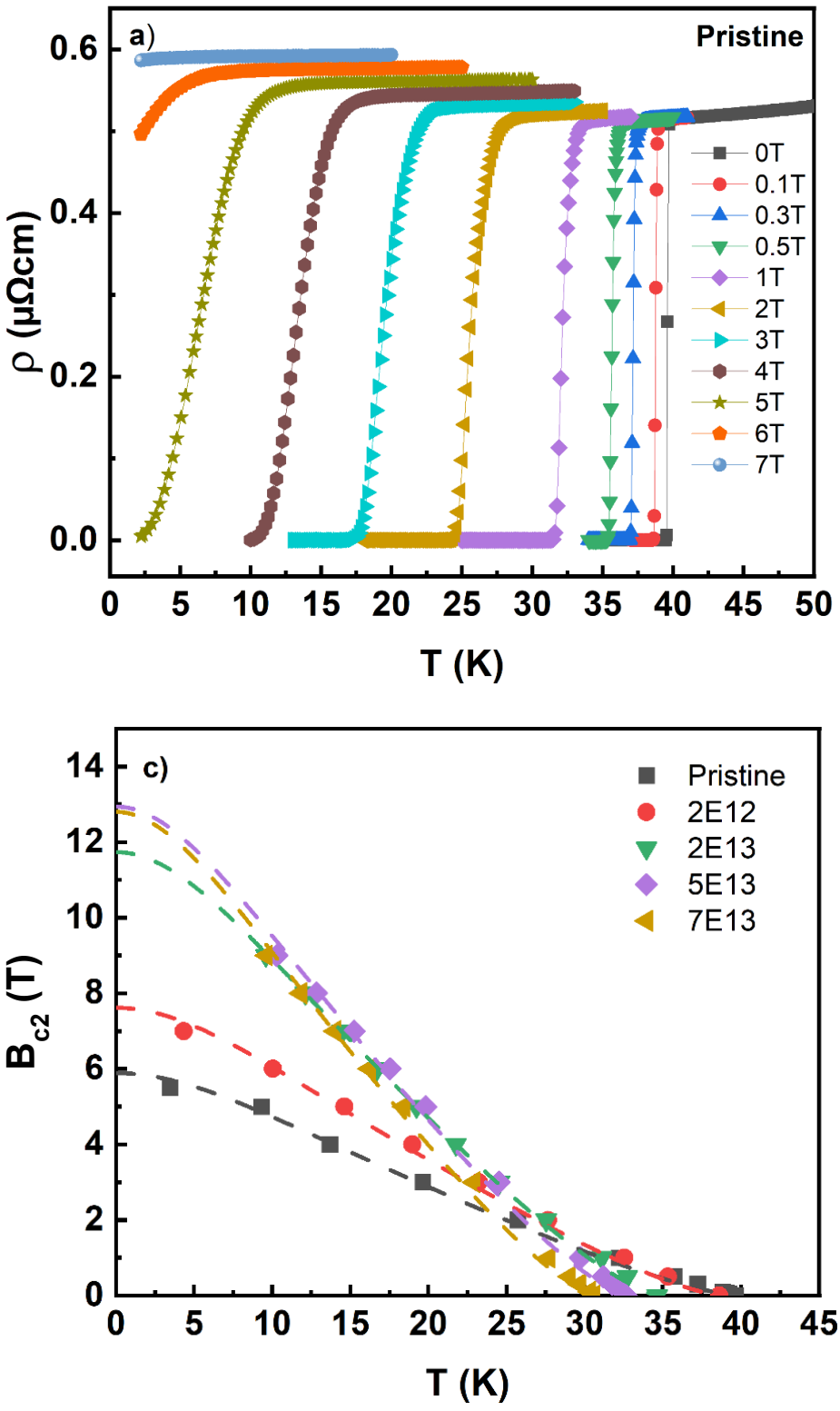

Figure 5.5. (a) The Pristine sample's in-field resistivity, (b) Sn-irradiated samples' in-field resistivity at dosage 5E13, and (c) temperature-dependent upper critical field (B_{c2}) for different fluences

5.5. Observations of magnectic vortex cores MgB_2 thin film superconductors before and after Sn^{2+} ion iradiation

At 4.26 K, MFM measurements were performed with a homemade ^{4}He MFM probe. The PPP-MFMR from NANOSENSORS™ was the identical MFM tip used for all measurements. The formula $\frac{\partial F}{\partial z} = -2k\frac{\Delta f}{f_0}$ [107] is used to get the magnetic force gradient $\partial F/\partial z$ from the frequency shift Δf, where f_0 (74.015 kHz) is the bare resonance frequency of the MFM cantilevers and k (2.8 N/m) is the force constant. Nb and MgB_2 thin film samples (Pristine and 5E13) in their superconducting state at 4.26 K are displayed in Figure 5.6 using MFM pictures. The Nb and clean MgB_2 thin film samples showed homogeneous vortices on a homogeneous backdrop. When a few Oersted's magnetic field is applied, field-cooling creates the vortices. Apart from the emergence of vortices, sample 5E13 had background inhomogeneity, which might be caused by non-superconducting flaws.

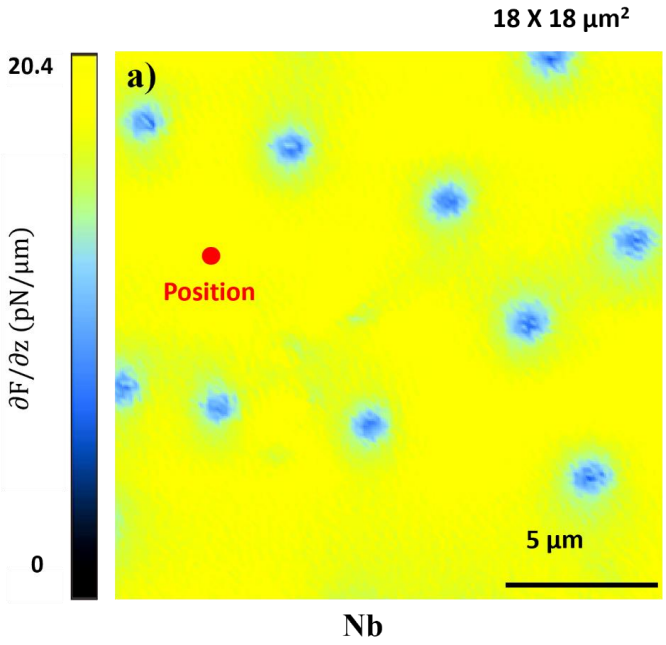

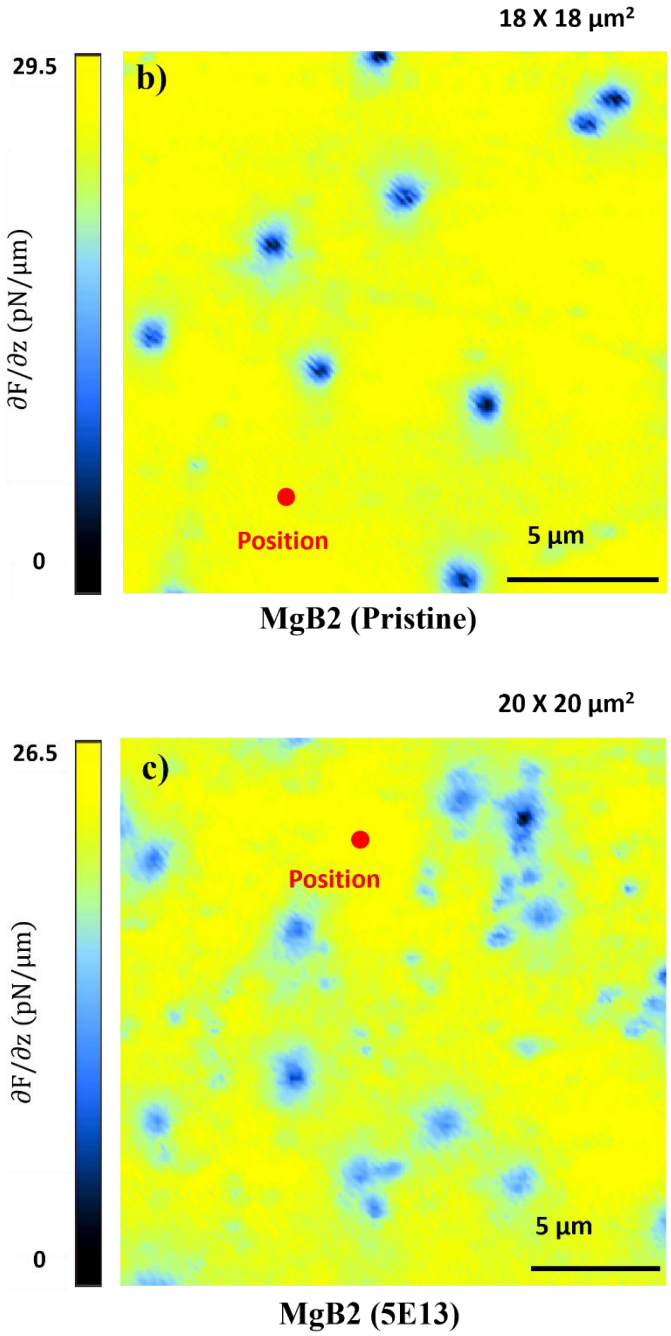

Figure 5.6. (a) The Nb film taken in the superconducting state at T = 4.26 K with a tip-sample lift height of 300 nm is shown in this 18 x 18 µm² MFM picture, (b) The MgB_2 (Pristine) sample taken in the superconducting state at T = 4.26 K with a tip-sample lift height of 300 nm is shown in this 18 x 18 µm² MFM picture, (c) The MgB_2 (5E13) sample taken in the superconducting state at T = 4.26 K with a tip-sample lift height of 300 nm is shown in this 20 x 20 µm² MFM picture.

The shielding currents in the superconducting sample screen the magnetic field of the tip, causing it to experience a Meissner force as it approaches the sample. The Meissner reaction is the name given to this. $\frac{\partial F}{\partial z} = \frac{A\Phi_0}{(z+\lambda)^3}$ is the formula for the Meissner response force gradient, where A is a prefactor that represents the sensor's geometry, Φ_0 is a single magnetic flux quantum, z is the tip-sample distance, and λ is the depth of in-plane magnetic penetration. A reference sample is necessary in order to compare the Meissner curves and determine the penetration depth λ. The reference sample was a 300 nm Nb thin film, and the penetration depth, λ_{Nb}(4.26 K), of the Nb film was confirmed to be around 110 nm [82]. When comparing the pristine and 5E13 MgB_2 samples to the reference sample (Nb film), Figure 5.7 (a) and (b) display the Meissner force gradient as a function of the tip-sample distance z. Meissner curve measurement locations are a few μm from Abrikosov vortex. When compared to the Nb reference, the MgB_2 thin film samples' Meissner force curve peak has a lower size, indicating that the MgB_2 sample has a higher value of λ. The Meissner force curves of the pristine as well as irradiated MgB_2 thin film samples may be shifted along the *z*-axis to that of the Nb film in order to get Δλ (= Δz), as we utilized the identical MFM tip. $\lambda_{pristine}(4.26\ K) = \lambda_{Nb}(4.26\ K) + \Delta\lambda = 110\ nm + 50\ nm = 160\ nm$ is the value for the pristine sample. This result is comparable to values that have been previously reported [54,58]. Likewise, λ_{5E13}(4.26 K) was found to be 270 nm. Because the irradiated sample has a greater penetration depth, the magnetic field can enter the material more deeply before the shielding current entirely filters it out. As an s-wave superconductor, MgB_2 may be approximated using the Gorter–Casimir formula: $\lambda(T) = \frac{\lambda(0)}{\sqrt{1-(T/T_c)^4}}$ [104]. $\lambda_{pristine}(0)$ along with $\lambda_{5E13}(0)$ have respective values of 159.99 and 269.96 nm. It is necessary to look at band interactions since MgB_2 is a two-band superconductor. As indicated in Table 5.2, the coherent length values were acquired using $\mu_0 H_{c2}(0) = \Phi_0/2\pi\xi^2(0)$ [59]. The thermodynamic critical field may be computed as follows using Ginzburg-Landau theory: $\mu_0 H_c(0) = \Phi_0/2\pi\xi(0)\lambda(0)$ [59]. The pristine and 5E13 samples had thermodynamic critical fields of 0.28 and

0.23 T, respectively. This suggests that the irradiated sample has a smaller density of superconducting electrons, which might be associated with a lower thermodynamic critical field or critical temperature.

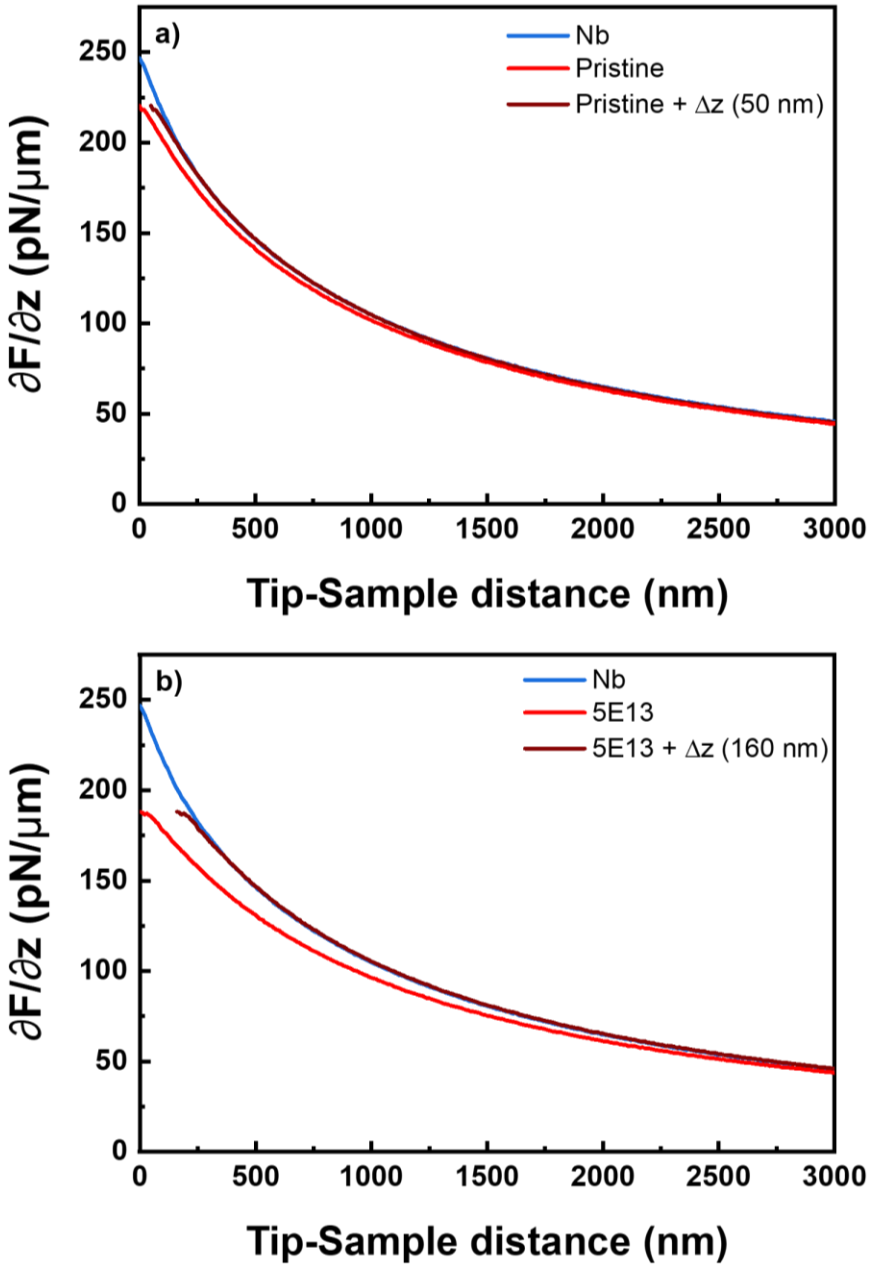

Figure 5.7. (a) As-measured Meissner force curves on MgB_2 (Pristine) (red) and the Nb film (blue), as well as the shifted Meissner force curve for MgB_2 (Pristine) (dark red), (b) as-measured Meissner force curves on MgB_2 (5E13) (red) and Nb film (blue), as well as the shifted Meissner force curve for MgB_2 (5E13) (dark red)

5.6. Comparision of doping effect on the J_c of MgB_2 bulk superconductors and ion irradiation effect on the J_c of MgB_2 thin film superconductors

The effect of sample fabrication conditions on J_c was systematically studied. The obtained results can be used to optimize the suitable fabrication conditions and create quality *ex-situ* MgB_2 bulk samples. The sample fabrication condition to increase J_c the most is Pure *ex-situ* MgB_2 + 0.5 Mg sintered at 1000 °C for 1 h. Following that research direction, the effect of doping on J_c of high-quality bulk samples was systematically studied. By the co-addition of B_4C and Dy_2O_3, the greatest J_c enhancement was obtained for the sample with 5 wt.% B_4C + 2.0 wt.% Dy_2O_3 and this result is shown in Figure 5.8. Beside the MgB_2 bulk superconductors, the MgB_2 thin film superconductors was also focused on research. A hybrid physical-chemical vapor deposition system (HPCVD) was employed to create MgB_2 thin film samples on the Al_2O_3 substrates. As shown in Figure 5.8, the J_c value of MgB_2 thin film samples is much larger than that of MgB_2 bulk samples. The effect of ion irradiation on J_c of MgB_2 thin film samples was systematically studied. By using 2 MeV energetic Sn ions, the condition for the strongest increase in J_c was when the MgB_2 thin film sample was irradiated with Sn^{2+} ions at a dose of 5×10^{13} ion/cm^2. The utilization of Sn^{2+} irradiated MgB_2 thin film samples for power applications is hence appealing.

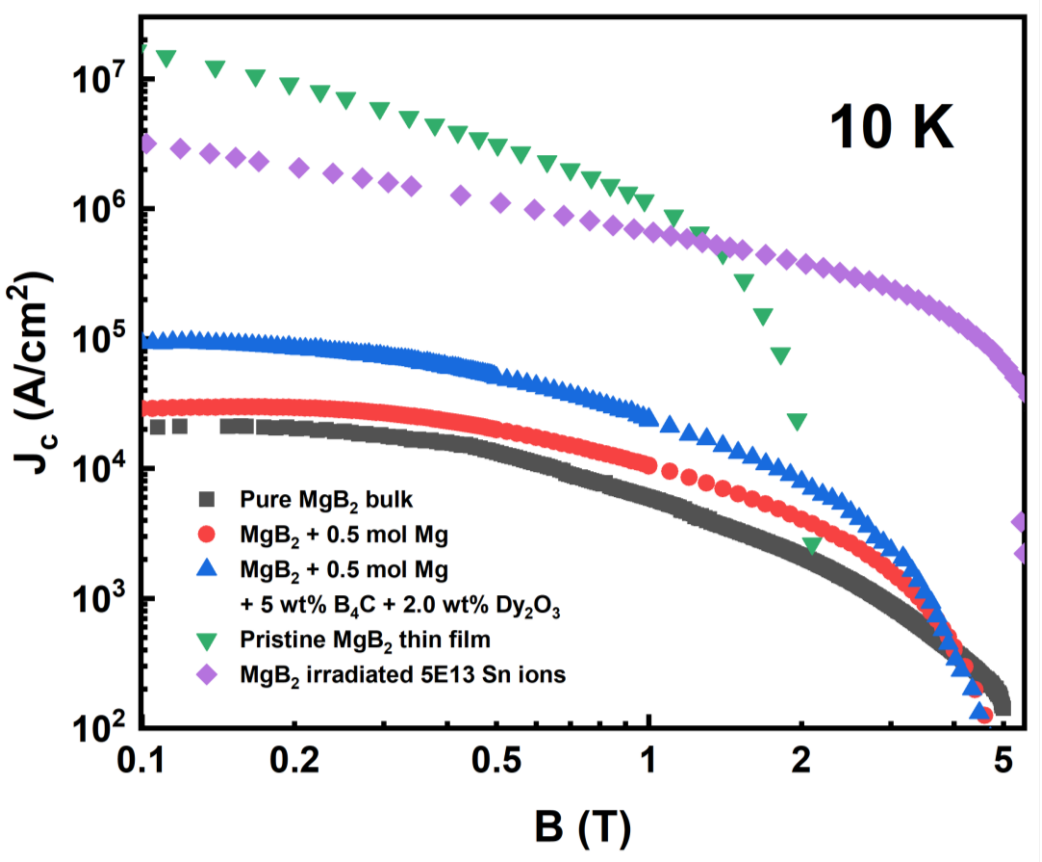

Figure 5.8. Comparision of J_c enhancements of the MgB_2 bulk and thin film samples at 10 K

Conclusion of Chapter 5

In conclusion, we elucidated how irradiation with Sn^{2+} ions, such as T_c, B_{c2}, as well in-field J_c, caused changes in the electron-phonon and superconductivity characteristics in MgB_2 thin film samples. This dissertation found a strong link between the mode at around ω_2 (the frequency of the E_{2g} mode) in MgB_2 and T_c, which supports the idea that this mode is the intended E_{2g} mode in MgB_2 and helps to explain the observed T_c. Using the McMillan formula, it was possible to anticipate from the Raman spectra that the T_c would decrease with increased ion dosage; transport data gathered throughout the film later verified this prediction. This dissertation find that the EPC constant, estimated from studies of the Raman spectra, plays an important role in the behavior of superconducting transitions. Accordingly, our results imply that the superconducting process of MgB_2 is influenced by the

disorder strength, which may result in Cooper pair localization, due to differences in EPC. While the values of J_c and B_{c2} rose and peaked at 5E13, the value of T_c steadily declined. Furthermore, J_c values can be improved by the opposition between the low value of β and the high value of B_{irr}. As a result, it is appealing to employ MgB_2-thin films exposed to Sn^{2+} ions for power applications.

CONCLUSION

The present dissertation delves into the investigation of the critical current density and flux pinning mechanism in MgB_2 superconductors. The main findings of this dissertation, which include advances in J_c in MgB_2 superconductors, can be summed up as follows:

Initially, the fabrication of MgB_2 bulk samples was optimized by using the conventional solid state reaction technique. By adjusting the additions of starting materials of Mg and B as well as the sintering temperature, critical temperature (T_c), critical current density (J_c), and the flux pinning force density (F_p) of the MgB_2 bulk were found to vary. The variation of T_c was found to link to the corresponding variation in electron-phonon coupling and the formation of phonon density of state of the samples probed by Raman spectra. The J_c enhancements were attributed to the improvements of grain connectivity, which was believed to effectively worked as 2D pinning centers by using the Dew-Hughes model. Therefore, the optimal sample fabrication condition to increase J_c was MgB_2 + 0.5 Mg sintered at 1000 °C for 1 hour.

To the further enhancements of J_c of MgB_2 bulk, the additions of proper impurity into solid-state reacted MgB_2 bulk were carried out. By applying the optimal fabrication conditions of MgB_2, the improved flux-pinning properties of MgB_2 bulk samples with co-additions of B_4C and Dy_2O_3 were investigated. The greatest J_c enhancement of ~ 1.5 – 3.2 times in the range of 0.1 to 2 T at 10 K was obtained for the sample with 5 wt.% B_4C + 2.0 wt.% Dy_2O_3. More interestingly, the co-additions of B_4C and Dy_2O_3 were shown to provide the enhancements of B_{c2}, with the maximum B_{c2} was achieve for the 5 wt.% B_4C added MgB_2 bulk sample up to 1.6 – 1.7 times. The improvements of grain connectivity and the dominance of 2D pinning centers in B_4C and Dy_2O_3 added MgB_2 bulk were also revealed by using the Dew-Hughes model. The evidences were likely to be reasons for enhancements of J_c and B_{c2}.

To further satisfy the power related application of MgB_2, the nearly single crystalline MgB_2 thin films were fabricated by using HPCVD technique. The J_c of the MgB_2 thin

film samples was found to be much higher than that of the MgB_2 bulk and the dominant pinning mechanism was still identified to be 2D pinning centers. The addition of different kind of pinning centers was performed by using the ion irradiation technique. The Sn^{2+} ions were irradiated into and expected to thoroughly pass the MgB_2 thin film samples. Evidence for the formation of point-like defects in form of ion track or crystal imperfections were indicated by the shifts in the XRD and Raman E_{2g} peaks. By varying the Sn^{2+} ion dose from 2×10^{12} to 7×10^{13} ion/cm^2, the obvious enhancements of J_c and B_{c2} were reached, those were ~ 2.5 – 1000 times in the range of 0.1 to 2 T at 10 K and 1.4 – 1.5 times, respectively. The pinning strength - obtained by using the collective pinning theory - of the Sn^{2+} irradiated MgB_2 films was found to be improved. The pinning mechanism was slightly shift from 2D to 1D pinning as suggested by the Dew Hughes model, which was possibly originated from the point-like defects. The researches on irradiation process to improve critical parameters of superconductors might be expanded with different kinds of ions.

DISSERTATION PUBLICATIONS

[1]. **Ha H. Pham**, An T. Pham, Phi Thi Huong, Nguyen Hoang Nam, Nurhidayah M. Hapipi, Soo Kien Chen, Muralidhar Miryala, Dzung T. Tran, Jungseek Hwang, Yu Seong Seo, Dang T. B. Hop, Nguyen Thanh Binh, and Duc H. Tran. (2023). Role of electron–phonon coupling in the superconducting state of MgB2 polycrystals fabricated at different conditions. *Ceramics International*, *49*(21), 34053–34061. https://doi.org/10.1016/J.CERAMINT.2023.08.105

[2]. **Ha H. Pham**, Tien Le, An T. Pham, Won Nam Kang, Nguyen H. Nam, Do T. K. Anh, Nguyen Hoang Anh, Hoo Keong Peh, Soo Kien Chen, Nguyen K. Man, Vuong Thi Anh Hong, Hanoh Lee, Tuson Park, Le Viet Cuong, Phan Hai, Nguyen Quang Huy, and Duc H. Tran (2024). Improved flux pinning properties of Mg exceed MgB2 ceramics with B4C and Dy2O3 additions. *Ceramics International*, *50*(23), 51509–51515. https://doi.org/10.1016/J.CERAMINT.2024.10.069

[3]. **Ha H. Pham**, Tien Le, The Nghia Nguyen, Nguyen Hoang Nam, Nhung T. Nguyen, Min Kyun Sohn, Dae Joon Kang, Tuson Park, Jinyoung Yun, Yeonkyu Lee, Jeehoon Kim, Duc H. Tran, and Won Nam Kang (2023). Correlation between electron-phonon coupling and superconductivity of Sn2+ ion irradiated MgB2-thin films. *Ceramics International*, *49*(12), 20586–20593. https://doi.org/10.1016/J.CERAMINT.2023.03.188

REFERENCE

Vietnamese

[26] Trần Hải Đức, (2025), "*Động lực học xoáy từ - Áp dụng trong một số vật liệu siêu dẫn loại II",* Vietnam National University Press, Hanoi.

[49] Thân Đức Hiền, (2008), "*Nhập môn về siêu dẫn : Vật liệu, tính chất và ứng dụng",* Bach Khoa Publishing House, Hanoi.

[103] Nguyễn Huy Sinh, (2006), "*Vật lý siêu dẫn",* Vietnam Education Publishing House, Hanoi.

English

[1] Abrikosov A.A., (1957), "On the Magnetic properties of superconductors of the second group", *Sov.Phys.JETP* 5pp. 1174–1182.

[2] Allen P.B., Dynes R.C., (1975), "Transition temperature of strong-coupled superconductors reanalyzed", *Phys Rev B* 12(3), pp. 905–922.

[3] An J.M., Pickett W.E., (2001), "Superconductivity of MgB2: Covalent Bonds Driven Metallic", *Phys Rev Lett* 86(19), pp. 4366–4369.

[4] Arvapalli S.S., Muralidhar M., Murakami M., (2019), "High-Performance Bulk MgB2 Superconductor Using Amorphous Nano-boron", *J Supercond Nov Magn* 32(7), pp. 1891–1895.

[5] Askerzade I.N., Gencer A., Güçlü N., (2002), "On the Ginzburg-Landau analysis of the upper critical field Hc2 in MgB2", *Supercond Sci Technol* 15(2), pp. L13–L16.

[6] Bardeen J., Cooper L.N., Schrieffer J.R., (1957), "Theory of superconductivity", *Physical Review* 108(5), pp. 1175–1204.

[7] Bateni A., Erdem E., Häßler W., Somer M., (2019), "High-quality MgB2 nanocrystals synthesized by using modified amorphous nano-boron powders: Study of defect structures and superconductivity properties", *AIP Adv* 9(4), p. 45018.

[8] Bateni A., Erdem E., Repp S., Weber S., Somer M., (2016), "Al-doped MgB2 materials studied using electron paramagnetic resonance and Raman spectroscopy", *Appl Phys Lett* 108(20), p. 202601.

[9] Bean C.P., (1964), "Magnetization of High-Field Superconductors", *Rev Mod Phys* 36(1), p. 31.

[10] Bednorz J.G., Müller K.A., (1986), "Possible high Tc superconductivity in the Ba-La-Cu-O system", *Zeitschrift für Physik B Condensed Matter* 64(2), pp. 189–193.

[11] Blatter G., Feigel'Man M. V., Geshkenbein V.B., Larkin A.I., Vinokur V.M., (1994), "Vortices in high-temperature superconductors", *Rev Mod Phys* 66(4), p. 1125.

[12] Bragg W.H., Bragg Apr W.L., H Bragg B.W., Professor of Physics C., (1913), "The reflection of X-rays by crystals", *Proceedings of the Royal Society of London. Series A, Containing Papers of a Mathematical and Physical Character* 88(605), pp. 428–438.

[13] Burdusel M., Aldica G., Popa S., Enculescu M., Mihalache V., Kuncser A., Pasuk I., Badica P., (2015), "B4C in ex-situ spark plasma sintered MgB2", *Current Applied Physics* 15(10), pp. 1262–1270.

[14] Buzea C., Yamashita T., (2001), "Review of the superconducting properties of MgB2", *Supercond Sci Technol* 14(11), p. R115.

[15] Di Castro D., Cappelluti E., Lavagnini M., Sacchetti A., Palenzona A., Putti M., Postorino P., (2006), "Raman spectra of neutron-irradiated and Al-doped MgB2", *Phys Rev B* 74(10), p. 100505.

[16] Charifoulline Z., (2006), "Residual Resistivity Ratio (RRR) measurements of LHC superconducting NbTi cable strands", *IEEE Transactions on Applied Superconductivity* 16(2), pp. 1188–1191.

[17] Chen D.X., Goldfarb R.B., (1998), "Kim model for magnetization of type-II superconductors", *J Appl Phys* 66(6), p. 2489.

[18] Chen S.K., Wei M., MacManus-Driscoll J.L., (2006), "Strong pinning enhancement in MgB2 using very small Dy 2O3 additions", *Appl Phys Lett* 88(19), .

[19] Choi H.J., Roundy D., Sun H., Cohen M.L., Louie S.G., (2002), "The origin of the anomalous superconducting properties of MgB2", *Nature 2002 418:6899* 418(6899), pp. 758–760.

[20] Dadiel J.L., Naik S.P.K., Pęczkowski P., Sugiyama J., Ogino H., Sakai N., Kazuya Y., Warski T., Wojcik A., Oka T., Murakami M., (2021), "Synthesis of Dense MgB2 Superconductor via In Situ and Ex Situ Spark Plasma Sintering Method", *Materials 2021, Vol. 14, Page 7395* 14(23), p. 7395.

[21] Dam B., Huijbregtse J.M., Klaassen F.C., Van Der Geest R.C.F., Doornbos G., Rector J.H., Testa A.M., Frelsem S., Martinez J.C., Stäuble-Pümpin B., Griessen R., (1999), "Origin of high critical currents in YBa2Cu3O7−δ superconducting thin films", *Nature* 399(6735), pp. 439–442.

[22] Dew-Hughes D., (1974), "Flux pinning mechanisms in type II superconductors", *Philosophical Magazine* 30(2), pp. 293–305.

[23] Dilek T., Taylan Koparan E., Başoğlu M., Yanmaz E., (2011), "The magnetic and structural properties of SiC-doped MgB 2 bulks prepared by the standard ceramic processing", *J Supercond Nov Magn* 24(1–2), pp. 495–497.

[24] Dou S.X., Soltanian S., Horvat J., Wang X.L., Zhou S.H., Ionescu M., Liu H.K., Munroe P., Tomsic M., (2002), "Enhancement of the critical current density and flux pinning of MgB2 superconductor by nanoparticle SiC doping", *Appl Phys Lett* 81(18), pp. 3419–3421.

[25] Duc T.H., An P.T., Anh D.T.K., Linh V.H., Ha P.H., Man N.K., (2019), "Effect of K Substitutions on Structural and Superconducting Properties in Bi1.6Pb0.4Sr2-xKxCa2Cu3O10+δ Compounds", *VNU Journal of Science: Mathematics - Physics* 35(2), pp. 42–49.

[27] Dunne L.J., Brändas E.J., Cox H., (2017), "High-Temperature Superconductivity in Strongly Correlated Electronic Systems", *Advances in Quantum Chemistry* 74pp. 183–208.

[28] Van Duong P., Ranot M., Kang W.N., (2014), "Single-Crystal like MgB2 thin films grown on c-cut sapphire substrates", *Progress in Superconductivity and Cryogenics* 16(3), pp. 7–9.

[29] Eisterer M., (2017), "Radiation effects on iron-based superconductors", *Supercond Sci Technol* 31(1), p. 013001.

[30] Erbe M., Hänisch J., Freudenberg T., Kirchner A., Mönch I., Kaskel S., Schultz L., Holzapfel B., (2014), "Improved REBa2Cu3O7−x (RE = Y, Gd) structure and superconducting properties by addition of acetylacetone in TFA-MOD precursor solutions", *J Mater Chem A Mater* 2(14), pp. 4932–4944.

[31] Erdem O., Kirat G., (2018), "Influence of coronene addition on some superconducting properties of bulk MgB2", *Journal of Materials Science: Materials in Electronics* 29(20), pp. 17222–17233.

[32] F. London and H.L., (1935), "The electromagnetic equations of the supraconductor", *Proc R Soc Lond A Math Phys Sci* 149(866), pp. 71–88.

[33] Ferrando V., Manfrinetti P., Marré D., Putti M., Sheikin I., Tarantini C., Ferdeghini C., (2003), "Effect of two bands on critical fields in MgB2 thin films with various resistivity values", *Phys Rev B* 68(9), p. 94517.

[34] Ferrando V., Pallecchi I., Tarantini C., Marré D., Putti M., Ferdeghini C., Gatti F., Aebersold H.U., Lehmann E., Haanappel E., Sheikin I., Orgiani P., Xi X.X., (2007), "Systematic study of disorder induced by neutron irradiation in MgB2 thin films", *J Appl Phys* 101(4), p. 043903.

[35] Gajda D., Morawski A., Zaleski A.J., Häßler W., Nenkov K., Małecka M., Rindfleisch M.A., Hossain M.S.A., Tomsic M., (2016), "Experimental research of high field pinning centers in 2% C doped MgB2 wires at 20 K and 25 K", *J Appl Phys* 120(11), .

[36] Gandikota R., Singh R.K., Kim J., Wilkens B., Newman N., Rowell J.M., Pogrebnyakov A. V, Xi X.X., Redwing J.M., Xu S.Y., Li Q., Moeckly B.H., (2005), "Effect of damage by 2 MeV He ions and annealing on Hc2 in MgB2 thin films", *Appl Phys Lett* 87(7), p. 072507.

[37] Gao Z., Santra S., Amirkhanlou S., Eardley E., Wort C., Grovenor C.R.M., Speller S.C., (2022), "Microstructures and superconducting properties of MgB2 bulk samples processed by ultra-high pressure-assisted sintering", *J Eur Ceram Soc* 42(16), pp. 7481–7490.

[38] Ghorbani S.R., Farshidnia G., Wang X.L., Dou S.X., (2014), "Flux pinning mechanism in SiC and nano-C doped MgB2: evidence for transformation from δTc to δℓ pinning", *Supercond Sci Technol* 27(12), p. 125003.

[39] Ghorbani S.R., Wang X.L., Dou S.X., Lee S.I.K., Hossain M.S.A., (2008), "Flux-pinning mechanism in silicone-oil-doped MgB2: Evidence for charge-carrier mean free path fluctuation pinning", *Phys Rev B Condens Matter Mater Phys* 78(18), p. 184502.

[40] Ginzburg V.L., Landau L.D., (1950), "On the Theory of Superconductivity", *Sov. Phys. JETP* 20(1064), .

[41] Gonano C.A., Zich R.E., Mussetta M., (2015), "Definition for polarization P and magnetization M fully consistent", *Progress In Electromagnetics Research B* 64(1), pp. 83–101.

[42] Goncharov A.F., Struzhkin V. V, Gregoryanz E., Hu J., Hemley R.J., Mao H., Lapertot G., Bud'ko S.L., Canfield P.C., (2001), "Raman spectrum and lattice parameters of MgB2 as a function of pressure", *Phys Rev B* 64(10), p. 100509.

[43] Gozzelino L., Gerbaldo R., Ghigo G., Torsello D., Bonino V., Truccato M., Grigoroscuta M.A., Burdusel M., Aldica G. V, Sandu V., Pasuk I., Badica P., (2020), "High magnetic shielding properties of an MgB2 cup obtained by machining a spark-plasma-sintered bulk cylinder", *Supercond Sci Technol* 33(4), p. 044018.

[44] Griessen R., Wen Hai-Hu, Van Dalen A.J.J., Dam B., Rector J., Schnack H.G., Libbrecht S., Osquiguil E., Bruynseraede Y., (1994), "Evidence for mean free path fluctuation induced pinning in YBa2Cu3O7 and YBa2Cu4O8 films", *Phys Rev Lett* 72(12), p. 1910.

[45] H. K. Onnes, (1911), "The Superconductivity of Mercury", *Comm. Phys. Lab. Univ. Leiden* 12p. 120.

[46] H. K. Onnes, (1913), "Further Experiments with liquid helium", *Commun. Phys. Lab. Univ. Leiden* 133b(29), .

[47] Hapipi N.M., Chen S.K., Shaari A.H., Kechik M.M.A., Lim K.P., Tan K.B., Lee O.J., Arvapalli S.S., Miryala M., (2022), "Enhanced critical current density of ex situ MgB2 via control of Mg assisted sintering", *Journal of Materials Science: Materials in Electronics* 33(14), pp. 11257–11268.

[48] Hapipi N.M., Chen S.K., Shaari A.H., Kechik M.M.A., Lim K.P., Tan K.B., Lee O.J., Miryala M., (2022), "Excess Mg in situ powder addition for enhancing critical current density of ex situ MgB2", *Appl Phys A Mater Sci Process* 128(10), pp. 1–14.

[50] Jin Y., (2017), "Novel Half-Metallic and Spin-Gapless Heusler Compounds", *Department of Physics and Astronomy: Dissertations, Theses, and Student Research* .

[51] Josephson B.D., (1962), "Possible new effects in superconductive tunnelling", *Physics Letters* 1(7), pp. 251–253.

[52] Jung S.-G., Kyung Seong W., Nam Kang W., (2013), "Flux Pinning Mechanism in Single-Crystalline MgB2 Thin Films", *J Physical Soc Japan* 82(11), p. 114712.

[53] Jung S.-G., Pham D., Han Y., Lee J.M., Kang W.N., Kim C., Yeo S., Jun B.-H., Park T., (2022), "Improvement of bulk superconducting current capability of MgB2 films using surface degradation", *Scr Mater* 209p. 114424.

[54] Jung S.G., Pham D., Lee J.M., Han Y., Kang W.N., Park T., (2021), "Effects of surface damage on critical current density in MgB2 thin films", *Current Applied Physics* 22pp. 14–19.

[55] Jung S.G., Pham D., Park T.H., Choi H.Y., Seo J.W., Kang W.N., Park T., (2019), "Giant proximity effect in single-crystalline MgB2 bilayers", *Scientific Reports 2019 9:1* 9(1), pp. 1–8.

[56] Kamihara Y., Hiramatsu H., Hirano M., Kawamura R., Yanagi H., Kamiya T., Hosono H., (2006), "Iron-based layered superconductor: LaOFeP", *J Am Chem Soc* 128(31), pp. 10012–10013.

[57] Kang B., Putri W.B.K., Kang W.N., (2019), "Effect of SiC buffer layer on flux pinning property of MgB2 tapes", *Current Applied Physics* 19(6), pp. 670–674.

[58] Kim H.J., Kang W.N., Choi E.M., Kim M.S., Kim K.H.P., Lee S.I., (2001), "High Current-Carrying Capability in *c*-Axis-Oriented Superconducting MgB2 Thin Films", *Phys Rev Lett* 87(8), p. 087002.

[59] Kim J.H., Oh S., Heo Y.U., Hata S., Kumakura H., Matsumoto A., Mitsuhara M., Choi S., Shimada Y., Maeda M., MacManus-Driscoll J.L., Dou S.X., (2012), "Microscopic role of carbon on MgB2 wire for critical current density comparable to NbTi", *NPG Asia Materials 2012 4:1* 4(1), pp. e3–e3.

[60] Kim J.H., Zhou S., Hossain M.S.A., Pan A. V., Dou S.X., (2006), "Strong enhancement of critical current density in MgB2 superconductor using carbohydrate doping", .

[61] Klein K.M., Park C., Tasch A.F., (1992), "Monte Carlo simulation of boron implantation into single-crystal silicon", *IEEE Trans Electron Devices* 39(7), pp. 1614–1621.

[62] Koblischka-Veneva A., Koblischka M.R., Berger K., Nouailhetas Q., Douine B., Muralidhar M., Murakami M., (2019), "Comparison of Temperature and Field Dependencies of the Critical Current Densities of Bulk YBCO, MgB2, and Iron-Based Superconductors", *IEEE Transactions on Applied Superconductivity* 29(5), p. 8649756.

[63] Kortus J., Mazin I.I., Belashchenko K.D., Antropov V.P., Boyer L.L., (2001), "Superconductivity of Metallic Boron in MgB2", *Phys Rev Lett* 86(20), pp. 4656–4659.

[64] Kumar R., Agrawal H.M., Kushwaha R.P.S., Kanjilal D., (2007), "Change in magnetic properties of MgB2 thin films after irradiation by 200 MeV Au ion beam", *Nucl Instrum Methods Phys Res B* 263(2), pp. 414–418.

[65] Larbalestier D.C., Cooley L.D., Rikel M.O., Polyanskii A.A., Jiang J., Patnaik S., Cai X.Y., Feldmann D.M., Gurevich A., Squitieri A.A., Naus M.T., Eom C.B., Hellstrom E.E., Cava R.J., Regan K.A., Rogado N., Hayward M.A., He T., Slusky J.S., Khalifah P., Inumaru K., Haas M., (2001), "Strongly linked current flow in polycrystalline forms of the superconductor MgB2", *Nature 2001 410:6825* 410(6825), pp. 186–189.

[66] Larkin A.I., Ovchinnikov Y.N., (1979), "Pinning in type II superconductors", *J Low Temp Phys* 34(3–4), pp. 409–428.

[67] Le T., Pham H.H., Nghia N.T., Nam N.H., Miyanaga T., Tran D.H., Kang W.N., (2023), "Effects of Sn-ion irradiation on local structure and flux pinning properties of MgB2 thin films", *Ceram Int* 49(2), pp. 2715–2720.

[68] Lee J.M., Jung S.G., Han Y., Park T.H., Jang J., Jeon H.R., Yeo S., Choi H.Y., Park T., Kang W.N., (2021), "Influence of disorder strength on the superconducting mechanism of MgB2", *Supercond Sci Technol* 35(1), p. 015001.

[69] Lee S., Masui T., Yamamoto A., Uchiyama H., Tajima S., (2003), "Carbon-substituted MgB2 single crystals", *Physica C Supercond* 397(1), pp. 7–13.

[70] Li W., Kang J., Liu Y., Zhu M., Li Y., Qu J., Zheng R., Xu J., Liu B., (2019), "Extrinsic Two-Dimensional Flux Pinning Centers in MgB 2 Superconductors Induced by Graphene-Coated Boron", *ACS Appl Mater Interfaces* 11(11), pp. 10818–10828.

[71] Li W.X., Li Y., Chen R.H., Zeng R., Dou S.X., Zhu M.Y., Jin H.M., (2008), "Raman study of element doping effects on the superconductivity of MgB2", *Phys Rev B* 77(9), p. 94517.

[72] Li Y., Kang G., Gao Y., (2016), "Scaling rules for critical current density in anisotropic biaxial superconductors", *Physica B Condens Matter* 491pp. 70–78.

[73] Loudhaief N., Ben Salem M., Labiadh H., Zouaoui M., (2020), "Electrical properties and fluctuation induced conductivity studies of Bi-based superconductors added by CuS nanoparticles synthesized through the aqueous route", *Mater Chem Phys* 242.

[74] McMillan W.L., (1968), "Transition Temperature of Strong-Coupled Superconductors", *Physical Review* 167(2), p. 331.

[75] Meissner W., Ochsenfeld R., (1933), "Ein neuer Effekt bei Eintritt der Supraleitfähigkeit", *Naturwissenschaften* 21(44), pp. 787–788.

[76] Meletov K.P., Kulakov M.P., Kolesnikov N.N., Arvanitidis J., Kourouklis G.A., (2002), "Raman spectra of MgB2 at high pressure and topological electronic transition", *Journal of Experimental and Theoretical Physics Letters* 75(8), pp. 406–409.

[77] Miryala M., (2024), "Advancing sustainability: Magnesium-based solutions for environmental challenges and high-performance technologies in superconductivity", *Journal of Magnesium and Alloys* 12(4), pp. 1257–1259.

[78] Mohd Hapipi N., Miryala M., Chen S.K., Arvapalli S.S., Murakami M., Kechik M.M.A., Tan K.B., Lee O.J., (2020), "Enhancement of critical current density for MgB2 prepared using carbon-encapsulated boron with co-addition of Dy2O3 and La2O3", *Ceram Int* 46(14), pp. 23041–23048.

[79] Muralidhar M., Higuchi M., Kitamoto K., Koblischka M.R., Jirsa M., Murakami M., (2018), "Enhanced Critical Current Density in Bulk MgB2", *IEEE Transactions on Applied Superconductivity* 28(4), .

[80] Muranaka T., Akimitsu J., (2011), "Superconductivity in MgB2", *Zeitschrift fur Kristallographie* 226(4), pp. 385–394.

[81] Nagamatsu J., Nakagawa N., Muranaka T., Zenitani Y., Akimitsu J., (2001), "Superconductivity at 39 K in magnesium diboride", *Nature* 410(6824), pp. 63–64.

[82] Nazaretski E., Thibodaux J.P., Vekhter I., Civale L., Thompson J.D., Movshovich R., (2009), "Direct measurements of the penetration depth in a superconducting film using magnetic force microscopy", *Appl Phys Lett* 95(26), p. 262502.

[83] Pham D., Jung S.-G., Tran D.H., Park T., Kang W.N., (2019), "Effects of oxygen ion implantation on single-crystalline MgB2 thin films", *J Appl Phys* 125(2), p. 023904.

[84] Pham H.H., Pham A.T., Huong P.T., Nam N.H., Hapipi N.M., Chen S.K., Miryala M., Tran D.T., Hwang J., Seo Y.S., Hop D.T.B., Binh N.T., Tran D.H., (2023), "Role of electron–phonon coupling in the superconducting state of MgB2 polycrystals fabricated at different conditions", *Ceram Int* 49(21), pp. 34053–34061.

[85] Pham The An, (2023), "Improvements of critical current density of Bi-Pb-Sr-Ca-Cu-O high-Tc superconductor by additions of nano-structured pinning centers", , VNU University of Science.

[86] Prikhna T., Eisterer M., Buchner B., Kluge R., Sokolovsky V., Moshchil V.E., Bodenseher A., Filzmoser J., Lindackers D., Ponomaryov S.S., Karpets M. V., Werfel F.N., Flogelndelor U., Vakaliuk A., Sverdun V.B., (2023), "Trapped Fields of Hot-Pressed MgB2for Applications in Liquid Hydrogen", *IEEE Transactions on Applied Superconductivity* 33(5), .

[87] Prikhna T., Sokolovsky V., Moshchil V., (2024), "Bulk MgB2 Superconducting Materials: Technology, Properties, and Applications", *Materials 2024, Vol. 17, Page 2787* 17(11), p. 2787.

[88] Prikhna T.A., Gawalek W., Savchuk Y.M., Sergienko N. V., Moshchil V.E., Wendt M., Habisreuther T., Dub S.N., Melnikov V.S., Kozyrev A. V., Schmidt C., Dellith J., Litzkendorf D., Nagorny P.A., Dittrich U., Sverdun B., Kovalev L.K., Penkin V.T., Goldacker W., Rozenberg O.A., Noudem J., (2008), "Peculiarities of high-pressure and hot-pressing manufacture of MgB2-based blocks with high critical currents for electrical machines", *J Phys Conf Ser* 97(1), p. 012022.

[89] Putra R.P., Oh J.Y., An G.H., Rahman I.N., Lee H.S., Kang B., (2024), "Raman Spectroscopy Investigation of Phonon Behavior in ZnO-Buffered MgB2 Tapes: Exploring Lattice Dynamics and Anharmonicity", *Journal of Physical Chemistry Letters* 15(35), pp. 8924–8932.

[90] Putra R.P., Oh J.Y., Jung S.G., Park H.S., Kang W.N., Kang B., (2023), "Enhancement in High-Field Jc Properties and the Flux Pinning Mechanism of ZnO-Buffered MgB2 Films", *ACS Omega* 8(12), pp. 11607–11613.

[91] Putri W.B.K., Van Duong P., Kang W.N., Miyanaga T., Yang D.-S., Kang B., (2016), "Close relation between Mg–Mg bonds and Tc of SiC buffered-MgB2 tapes", *J Alloys Compd* 665pp. 352–354.

[92] Putti M., Vaglio R., Rowell J.M., (2008), "Radiation effects on MgB2: a review and a comparison with A15 superconductors", *Supercond Sci Technol* 21(4), p. 043001.

[93] Qin M.J., Wang X.L., Liu H.K., Dou S.X., (2002), "Evidence for vortex pinning induced by fluctuations in the transition temperature of MgB2 superconductors", *Phys Rev B* 65(13), pp. 1–4.

[94] Quilty J.W., (2003), "The MgB2 superconducting energy gaps measured by Raman spectroscopy", *Physica C Supercond* 385(1), pp. 264–272.

[95] Ranot M., Duong P. V., Bhardwaj A., Kang W.N., (2015), "A review on the understanding and fabrication advancement of MgB2 thin and thick films by HPCVD", *Progress in Superconductivity and Cryogenics (PSAC)* 17(2), pp. 1–17.

[96] Rowell J.M., (2003), "The widely variable resistivity of MgB2 samples", *Supercond Sci Technol* 16(6), p. R17.

[97] Saito A., Shimakage H., Kawakami A., Wang Z., Kuroda K., Abe H., Naito M., Moon W.J., Kaneko K., Mukaida M., Ohshima S., (2004), "XRD and TEM studies of as-grown MgB2 thin films deposited on r- and c-plane sapphire substrates", *Physica C Supercond* 412–414(SPEC. ISS.), pp. 1366–1370.

[98] Seong W.K., Oh S., Kang W.N., (2012), "Perfect Domain-Lattice Matching between MgB2 and Al2O3: Single-Crystal MgB2 Thin Films Grown on Sapphire", *Jpn J Appl Phys* 51(8R), p. 083101.

[99] Shcherbakova O. V., Pan A. V., Wang J.L., Shcherbakov A. V., Dou S.X., Wexler D., Babić E., Jerčinović M., Husnjak O., (2008), "Sugar as an optimal carbon source for the enhanced performance of MgB 2 superconductors at high magnetic fields", *Supercond Sci Technol* 21(1), .

[100] Shibata T., Sakai S.I., (2016), "Passive Micro Vibration Isolator Utilizing Flux Pinning Effect for Satellites", *J Phys Conf Ser* 744(1), .

[101] Shinde S.R., Ogale S.B., Higgins J., Choudhary R.J., Kulkarni V.N., Venkatesan T., Zheng H., Ramesh R., Pogrebnyakov A. V., Xu S.Y., Li Q., Xi X.X., Redwing J.M., Kanjilal D., (2004), "Modification of critical current density of MgB2 films irradiated with 200 MeV Ag ions", *Appl Phys Lett* 84(13), pp. 2352–2354.

[102] Simon G., Miryala M., (2024), "Impact of doping on MgB2 superconductors: A comprehensive review", *Journal of Alloys and Compounds Communications* 3p. 100023.

[104] Sokolovsky V., Prikhna T., Meerovich V., Eisterer M., Goldacker W., Kozyrev A., Weber H.W., Shapovalov A., Sverdun V., Moshchil V., (2017), "MgB2-based superconductors for fault current limiters", *IOP Conf Ser Mater Sci Eng* 171(1), p. 012144.

[105] Sudesh, Das S., Bernhard C., Varma G.D., (2014), "Enhanced superconducting properties of rare-earth oxides and graphene oxide added MgB2", *Physica C: Superconductivity and its Applications* 505pp. 32–38.

[106] Sueyoshi T., (2021), "Modification of critical current density anisotropy in high-tc superconductors by using heavy-ion irradiations", *Quantum Beam Science* 5(2), .

[107] T. G. Berlincourt, R. R. Hake, (1962), "Pulsed-magnetic-field studies of superconducting transition metal alloys at high and low current densities", *Bull. Am. Phys. Soc. II.* 7(408), .

[108] Vinícius G., "Introduction to Superconductivity, by Michael Tinkham (2nd edition)", .

[109] Wang J., Zhuang C.G., Li J., Wang Y.Z., Feng Q.R., Zheng D.N., (2009), "Upper critical field and Raman spectra of MgB2 thin films irradiated with low energy oxygen ion", *J Appl Phys* 106(9), p. 093915.

[110] Wu F., (2014), "The Improved Superconducting Properties in the Ex-situ Sintered MgB2 Bulks with Mg Addition", *J Low Temp Phys* 177(3–4), pp. 157–164.

[111] Wulferding D., Kim G., Kim H., Yang I., Bauer E.D., Ronning F., Movshovich R., Kim J., (2020), "Local characterization of a heavy-fermion superconductor via sub-Kelvin magnetic force microscopy", *Appl Phys Lett* 117(25), p. 252601.

[112] Xi X.X., Pogrebnyakov A. V., Xu S.Y., Chen K., Cui Y., Maertz E.C., Zhuang C.G., Li Q., Lamborn D.R., Redwing J.M., Liu Z.K., Soukiassian A., Schlom D.G., Weng X.J., Dickey E.C., Chen Y.B., Tian W., Pan X.Q., Cybart S.A., Dynes R.C., (2007), "MgB2 thin films by hybrid physical-chemical vapor deposition", *Physica C: Superconductivity and its applications* 456(1–2), pp. 22–37.

[113] Yamamoto A., Tanaka H., Shimoyama J.I., Ogino H., Kishio K., Matsushita T., (2012), "Towards the realization of higher connectivity in MgB 2 conductors: In-situ or sintered ex-situ?", *Jpn J Appl Phys* 51(1), .

[114] Yang P., Lieber C.M., (1996), "Nanorod-Superconductor Composites: A Pathway to Materials with High Critical Current Densities", *Science (1979)* 273(5283), pp. 1836–1840.

[115] Yao C., Ma Y., (2021), "Superconducting materials: Challenges and opportunities for large-scale applications", *iScience* 24(6), p. 102541.

[116] Yates K.A., Burnell, Stelmashenko N.A., Kang D.-J., Lee H.N., Oh B., Blamire M.G., (2003), "Disorder-induced collapse of the electron-phonon coupling in MgB2 observed by Raman spectroscopy", *Phys Rev B* 68(22), p. 220512.

[117] Yeoh W.K., Horvat J., Dou S.X., Keast V., (2004), "Strong pinning and high critical current density in carbon nanotube dopedMgB2", *Supercond Sci Technol* 17(9), p. S572.

[118] Yildirim T., Gülseren O., Lynn J.W., Brown C.M., Udovic T.J., Huang Q., Rogado N., Regan K.A., Hayward M.A., Slusky J.S., He T., Haas M.K., Khalifah P., Inumaru K., Cava R.J., (2001), "Giant Anharmonicity and Nonlinear Electron-Phonon Coupling in MgB2: A Combined First-Principles Calculation and Neutron Scattering Study", *Phys Rev Lett* 87(3), p. 37001.

[119] Zeng X., Pogrebnyakov A. V., Kotcharov A., Jones J.E., Xi X.X., Lysczek E.M., Redwing J.M., Shengyong X.U., Li Q., Lettieri J., Schlom D.G., Tian W., Pan X., Liu Z.K., (2002), "In situ epitaxial MgB2 thin films for superconducting electronics", *Nature Materials 2002 1:1* 1(1), pp. 35–38.

[120] Ziegler J.F., Biersack J.P., (1985), "The Stopping and Range of Ions in Matter", *Treatise on Heavy-Ion Science* pp. 93–129.

[121] Ziegler J.F., Ziegler M.D., Biersack J.P., (2010), "SRIM – The stopping and range of ions in matter (2010)", *Nuclear Instruments & Methods in Physics Research Section B-beam Interactions With Materials and Atoms* 268(11–12), pp. 1818–1823.

[122] Zou J., Ainslie M.D., Fujishiro H., - al, Naito T., Mochizuki H., Fujishiro H., Zhang W., Deng Z., Zhang Y., Durrell J.H., Ainslie M.D., Zhou D., Vanderbemden P., Bradshaw T., Speller S., Filipenko M., Cardwell D.A., (2018), "Bulk superconductors: a roadmap to applications", *Supercond Sci Technol* 31(10), p. 103501.